The Dissertation Committee for Qingjun Zhou Certifies that this is the approved version of the following dissertation:

ELECTRO-OPTIC MODULATORS BASED ON POLYMERIC Y-FED DIRECTIONAL COUPLERS

Committee:

Ray T. Chen, Supervisor

Michael Becker

A. Bruce Buckman

Dim-Lee Kwong

Boris Tsap

ELECTRO-OPTIC MODULATORS BASED ON POLYMERIC Y-FED DIRECTIONAL COUPLERS

by

Qingjun Zhou, B.S., M.S., M.S.

Dissertation

Presented to the Faculty of the Graduate School of
The University of Texas at Austin
in Partial Fulfillment
of the Requirements
for the Degree of

Doctor of Philosophy

The University of Texas at Austin
December, 2004

To my parents, my wife and my daughter

Acknowledgements

I would like to thank my advisor Dr. Ray T. Chen for his conferring with me and offering theoretical guidance and advice on the experimental aspects of the research. It has certainly been satisfying and rewarding to work in the optical interconnect research group. I offer my thanks to the members of the group for their long-term valuable help. I am also grateful to the members of my dissertation committee, Dr. Michael Becker, Dr. A. Bruce Buckman, Dr. Dim-Lee Kwong, and Dr. Boris Tsap for giving me advice on my research and for taking the time to read this dissertation, listen to my defense, and ask useful questions.

I would also like to say thank you to my wife and other members of my family for their encouragement and support during my study and research at the University of Texas at Austin. Without their help and care, it would be difficult to imagine my having accomplished the progress of these past few years.

I would also like to thank Ms. Jean L. Toll and Ms. Melanie R. Gulick for their help these years.

ELECTRO-OPTIC MODULATORS BASED ON POLYMERIC Y-FED DIRECTIONAL COUPLERS

Publication No._____________

Qingjun Zhou, Ph.D.
The University of Texas at Austin, 2004

Supervisor: Ray T. Chen

The performance of current commercially available electro-optical (EO) intensity modulators is adversely affected by the distortions caused by the nonlinearity of their modulation curves. Furthermore, the direct-current biases, required in order to bring these modulators to their best working points, result in more complicated circuit fabrications than are desirable. This current research investigated the feasibility of fabricating bias-free and/or high-linear EO modulators by incorporating the merits of the Y-fed directional couplers (YCMs) with those of the EO polymer materials.

To this end, EO polymer-based conventional YCMs were employed to fabricate bias-free EO modulators. A low switching voltage of 3.6V and a high extinction ratio of 26dB were obtained, at a 1.34μm wavelength, with a conventional polymeric YCM having lumped electrodes. A high-speed intrinsic 3dB-biased EO modulator based on a conventional polymeric YCM operating at a 1.55μm

wavelength was successfully demonstrated to provide a 22-GHz 3-dB bandwidth, with a performance similar to that of a quadrature-biased Mach-Zehnder modulator (MZM) in terms of nonlinear distortion suppression when no direct-current bias was applied.

A broadband high-linear EO modulator based on a Δβ-inverted polymeric YCM was also demonstrated for the first time. This modulator had a 3-dB bandwidth of 20GHz, and a high nonlinear distortion suppression, which was approximately 20dB larger than that of a quadrature-biased MZM in the range between 0 and 8 GHz. The linearity properties of the high-speed Δβ-inverted YCMs were also investigated theoretically. The results show that broadband high-linear modulators can be achieved by taking advantage of the small dispersion in EO polymers' refractive indexes at microwave and optic frequencies.

A systematic study on traveling-wave (TW) electrodes for polymer-based directional couplers was conducted for the first time in order to find the optimal electrode structure and dimensions. A conformal-mapping approach to the optimum TW electrode design of a coplanar waveguide with ground (CPWG) was developed and employed to optimize the electrode dimensions.

Table of Contents

List of Tables

List of Figures

Chapter 1 Introduction

Optical modulators are a family of opto-electronic or opto-mechanical components that change the parameters of the optical signals dynamically in a controlled manner. In modern technologies, more and more applications turn to optical solutions in order to take advantage of optics' extremely large bandwidth capability and high packaging density potential. As a key component influencing the interface between optics and other mechanism such as electronics, optical modulators are fulfilling increasingly important roles.

Optical modulators have a wide range of applications in many fields, such as telecommunication, analog-to-digital conversion, phased-array radar, electrical-to-optical signal transduction. Although the polymer-based electro-optical modulators designed and fabricated in this current research are generally applicable to many fields, their applications to analog systems are particularly emphasized here.

Different characteristics of the modulators are emphasized for different applications. As a typical analog application of optical modulators, analog optical links have the requirements for modulators that are characteristic of most other analog applications. In order to research these requirements, analog optical links are introduced briefly in Section 1.1. There follows an overview of optical modulators in Section 1.2. Section 1.3 discusses the insufficiency of current modulators for analog applications. Section 1.4 presents the advantages of polymer-based directional couplers. Lastly, the motivation for the research and the organization of the total dissertation are given in Section 1.5.

1.1. OVERVIEW OF ANALOG OPTICAL LINKS [1,2]

1.1.1. Implementation

Optical link refers to an optical transmission channel designed to connect two electronic terminals. At a minimum, an optical link, as shown in Figure 1.1, consists of a transmitter (all the hardware required to impose an electric signal on an optical carrier), the transmission medium, and a receiver (all the hardware required to recover the electrical signal from the carrier). An optical link can be used to transfer either digital signals, such as in fiber-based telecommunication systems, or analog signals. In the latter, the link referred to here is an analog optical link.

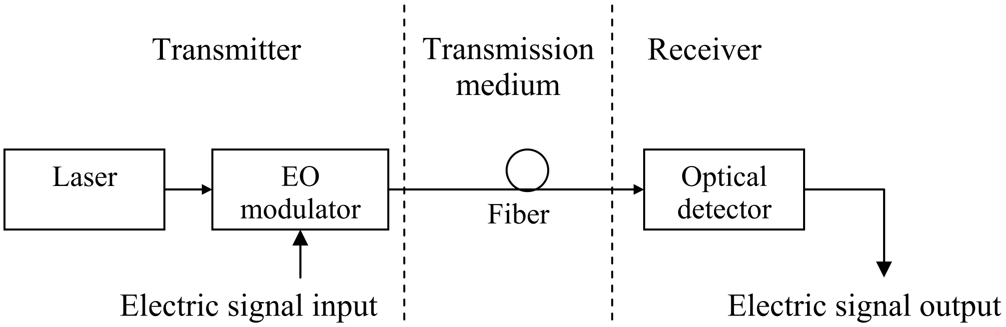

Figure 1.1. Schematic of a fiber optical link with an external modulator

The optical medium can be free space, optical waveguides, or other mediums that can conduct optical signals. For large distances, the optical medium is usually optical fiber, and the carrier's wavelength is usually 1.3 or 1.5 μm. The transmitter can be either a single direct modulated laser or a laser and an external modulator. The performance of direct modulated lasers is limited by their small bandwidth, large relative intensity noise (RIN), and distortions [3]. Currently, optical links with external modulators give better performance by taking advantage of optimizing the laser and the modulator separately. On the receiver side, both direct detection and coherence detection can be employed to recover the signal from the optical carrier. To our knowledge, every fiber-optic link in operation outside of laboratories uses a single semiconductor photodiode to perform direct detection of the light, which is intensity-modulated by the input RF signal. By contrast, the cost and complexity of coherent detection techniques have thus far precluded their widespread use in the field [1].

The optical link models and results presented here apply to intensity-modulation/direct-detection (IMDD) analog optical links with external modulation.

1.1.2. Applications and spurious free dynamic range requirements

Due to the intrinsic large bandwidth of optics and the low loss in optical fibers, analog optical links have been used or have the potential to be used in many fields. These applications usually require an optical link exhibiting high linearity in order to reduce the nonlinear distortion. In an IMDD link with an external modulator, almost without exception, the principal source of nonlinear distortion is the modulator, because of its nonlinear transfer curve. Therefore, in order to design modulators for these applications, it is mandatory to analyze the linearity requirements of these applications. The figure of merit to describe the nonlinearity property is Spurious Free Dynamic Range, SFDR, which actually is the maximum range (expressed in dB) of the input signal power in which the output signal is greater than the output noise, but the output distortion products resulting from device nonlinearities are below the output noise. In this section, the major application of optical links and their SFDR requirements are described.

Analog optical links have been found wide spread use as a mean of cable television (CATV) signal distribution [4]. CATV system designers wish to have a single link carry as many channels as possible without significant distortion of any one channel. They use a measurable parameter called “composite triple beat” (CTB) to quantity the level of distortion resulting from a given number of channels. When channels are spaced at equal frequency intervals, a small part of the information transmitted on three of the channels can appear as distortion on a fourth channel transmitted at a frequency that is the sum of two channel frequencies minus the third channel’s frequency. Thus CTB, like SFDR, is a measure of nonlinearity. To meet the CTB requirements of the CATV application, the link SFDR must exceed 110 dB in a 1HZ bandwidth [2].

Analog optical links have proved to be extremely useful also in radar systems. One application is to implement optical true-time delay modules in phased array antenna systems. Another application is in the routing of signals to and from antennas remotely located from the radar’s signal-generating and -processing equipment. In remoting applications, the link that brings the received signals to the central receiver/signal-processor equipment from the remote antennas has more stringent performance requirements than links that carry transmitted signals to the antenna from the signal generators. It has been proposed that a link exhibiting SFDR > 145dB in a 1-Hz bandwidth will meet or exceed the performance needs for most receive radar antennas [2].

Optical links can also carry cellular phone signals and personal communication system signals between antenna base stations and the central routing stations. In this application, the signals conveyed by the up-link (which carries information from the antenna site to the central station) should have the capability of transferring multiple calls simultaneously without undergoing significant distortion, meaning that high SFDR is also required.

1.2. OVERVIEW OF OPTICAL MODULATORS

1.2.1. Operational principles and categories

For developing optical modulators, there are four important factors: modulated parameters, mechanisms, structures, and materials.

The first factor is the optical parameter that is modulated. Considerations include intensity, phase, frequency, and propagation direction. The second factor is the physics effect to be employed for *modulation*. The phase, frequency and propagation direction can be modulated through changing the refractive index which is in turn effected (1) by applying an external electrical field (electro-optical (EO) effect), (2) by changing the temperature (thermal effect), or (3) by inducing a strain (photoelastic effect). For semiconductors, more mechanisms such as the plasma effect, the quantum confined stark effect (QCSE), or the band gap shift effect can also be used to tune the refractive index. The optical intensity can be directly modulated through changing the absorption coefficient; this change can be accomplished by using QCSE or the Franz-Keldysh (FK) effect in the case of semiconductor-based modulators. The third factor is the modulator *structures*, examples including bulk structure, waveguide structure, grating structure, and micro-machine structure. The last factor is the *material* used to fabricate the modulators. Major materials include inorganic crystalline materials (such as lithium niobate (LiNbO3)), semiconductor materials, and polymer materials. By combining these four factors, a quite wide variety of optical modulators have been developed, often very specialized for a particular application.

The intention of this section is to give a brief introduction to modulators suitable for optical link applications rather than to give a general review of the whole optical modulator family. The reader may refer elsewhere [3,5] for a more detailed overview of optical modulators.

1.2.2. Modulators for optical link applications

The modulator for an IMDD optical link application should be an intensity modulator with high-speed capability. Waveguide is the most convenient structure since it facilitates coupling light from waveguides to a fiber, which is usually the link media. The EO, QCSE, and FK effects are usually the mechanisms used for high-speed modulations. Electroabsorption modulators (EAM), as shown in Figure 1.2(a), have a single-waveguide structure that is the simplest structure for waveguide-based modulators. EAMs modulate the output intensity by directly changing the absorption coefficient in turn employing the QCSE or FK effects. Waveguide-based Mach-Zehnder interferometers (MZM), as shown in Figure 1.2(b), and directional couplers are commonly used to convert a phase modulation induced by EO or QCSE effects into an intensity modulation. The traditional structure of a directional coupler (denoted by DCM) is shown in Figure 1.2(c). The Y-fed directional coupler (denoted by YCM), as shown in Figure 1.2(d), is a new and exceptionally important structure and is the research topic of this thesis. The advantages of this structure are discussed in Section 1.4 and in the chapters thereafter. Table 1.1 shows the possible modulators for optical IMDD link applications. Some of the modulators shown in this table, such as $LiNbO_3$ MZM, and EAM, are commercially available. Others are still in the research phase.

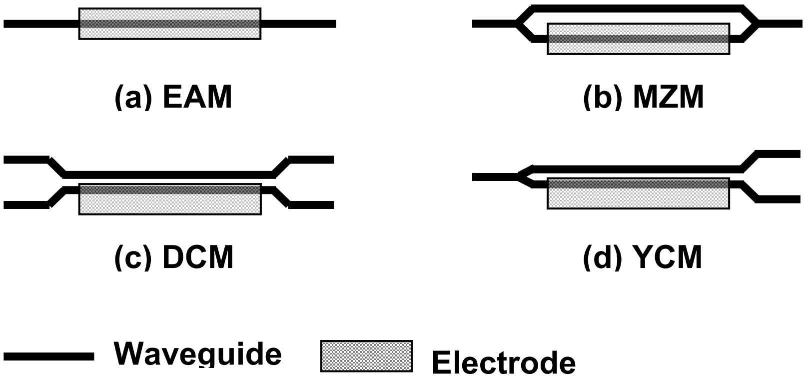

Figure 1.2. Schematic of waveguide-based intensity modulators: (a) Electroabsorption modulator (EAM); (b) Mach-Zehnder interferometer (MZM); (c) traditional directional coupler modulator (DCM); (d) Y-fed directional coupler modulator (YCM)

Table 1.1 Waveguide-based high-speed modulator

Modulator	Waveguide structure	Materials	Physical mechanism
EAM[a]	Single waveguide	Semiconductor	FKE[b], QCSE[c]
MZM[d]	Mach-zehnder interferometer	Semiconductor	QCSE, EO[e]
		$LiNbO_3$	EO
		polymer	EO
DCM[f],YCM[g]	Directional coupler	Semiconductor	QCSE, EO
		$LiNbO_3$	EO
		polymer	EO

a. EAM: Electrodabsorption modulator
b. FK: Franz-Keldysh effect
c. QCSE: quantum confined stark effect
d. MZM: Mach-zehnder modulator
e. EO: Electro-optical effect
f. DCM: Traditional directional coupler modulator
g. YCM: Y-fed directional coupler modulator

As a comparison of the properties of $LiNbO_3$, semiconductors, and EO polymers, Table 1.2 gives some representative data of these materials [6]. MZM is chosen as the benchmark since it is the most popular modulator structure.

Table 1.2 Comparison of $LiNbO_3$, gallium arsenide and polymer materials

Property	**Gallium arsenide**	**$LiNbO_3$**	**EO polymer**
EO coefficient (Pm/V at 1.3 micron)	1.5	31	>70
Dielectric constant (ε)	10-12	28	2.5-4.0
Refractive index (n)	3.5	2.2	1.6-1.7
Optical loss (dB/cm at 1.3 micron)	2	0.2	0.2-3
Maximum optical power (mW)	30	250	250*

* Obtained with a hardened polymeric material

1.3. NONLINEARITY OF OPTICAL MODULATORS [7,8,9,10]

As mentioned in the previous section, EAM, MZM, and DCM are the three types of modulator, which can be used for an optical link application. The linearity of their transfer curves is different from each other's. The transfer curves of an EAM are usually quite nonlinear; thus it is seldom used in an optical link having high dynamic range requirements. A normal DCM biased on 0.43Vs (Vs represents the switch voltage), where the second harmonic distortion is zero, has similar SFDR to that of an MZM biased at the quadrature point. When a normal DCM is biased at 0.70Vs, although its intermodulation is very small, its second-order harmonic distortion is extremely large, making its broadband SFDR much smaller than that of a quadrature-biased MZM. Most IMDD optical link demonstrations use MZMs biased at their quadrature points where all the even orders of harmonic distortion are zero. Here, MZMs are chosen as the benchmark to analyze modulators' linearity properties.

For a quadrature-biased MZM, the third-order intermodulation distortion (IMD) is the dominant distortion, which usually determines the SFDR of the optical link in which the MZM is embedded. Figure 1.3 shows the simulated fundamental signal, the third-order IMD, and the third-order harmonic distortion of a quadrature-biased MZM vs. modulation depth. In the calculation, two signals with the frequencies f1 and f2=1.1f1 (nonlinear distortion is independent of the signal frequency) are inputted into the modulator. The fundamental and distortions are then calculated by performing Fourier transforms. The result indicates that, when the modulation depth is 1%, the available SFDR is only around 100dB. In order to obtain a larger SFDR, the modulation depth must then be further reduced. However, the modulation depth can not be decreased infinitely, since it will finally be limited by the noise level. Moreover, to eliminate the even orders of harmonic distortions, the MZM needs to be exactly biased to its quadrature point. A complex system is usually employed to provide a strictly controlled direct current (*dc*) bias.

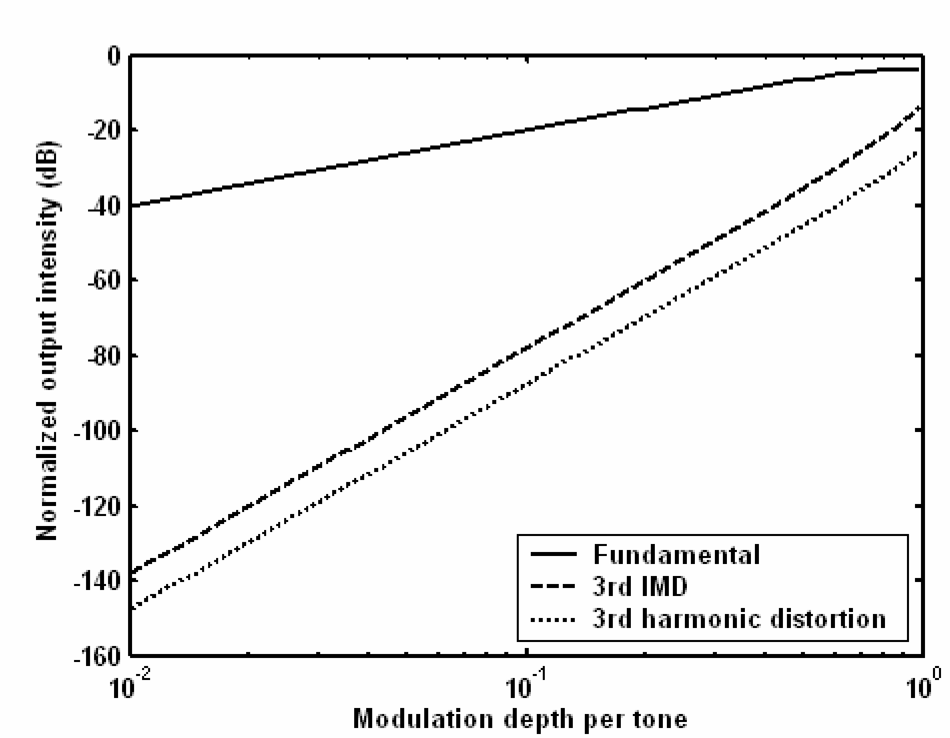

Figure 1.3. The normalized fundamental signal, third-order intermodulation distortion (IMD), and third-order harmonic distortion of a quadrature-biased Mach-Zehnder modulator as a function of the modulator's modulation depth

The above analysis and simulation results given in Figure 1.3 show that a simple standard modulator can not satisfy the requirements of analog optical links with high SFDR, e.g., >130 dB for antenna remote applications. Many techniques have been investigated to improve the modulation linearity by using standard modulators. These techniques can be basically divided into four categories: (1) Electronic techniques (including a predistortion technique in which a broadband nonlinear electronic circuit is incorporated into the modulator driver to supply signals to cancel the distortion signals generated by the modulator); (2) electro-optical techniques (including feed-back and feed-forward techniques in which a correction signal, derived by monitoring the difference between the modulator RF input and the optical output, is added in the optical domain to correct the optical output); (3) multiple modulator techniques (including dual series MZMs, triple MZMs, etc., where multiple modulators are used and the distortions generated by these modulators are cancelled by each other); and (4) multiple bias techniques (including triple-directional-coupler techniques in which multiple bias voltages are applied to different sections of the directional coupler). These techniques have some common drawbacks such as complexity, needing more optical devices, and strict conditions requirement. In these techniques, more optical devices like splitters, lasers, detectors, and extra modulators are needed to perform the modulation function that should be achieved by a single modulator. All of these techniques need strict bias controls and some of them need to split the input optical light and the RF driving signal in order to feed multiple modulators. Since the bias voltages and the intensity-splitting ratio must be extremely exact in order to achieve high SFDR, thee control systems needed to perform these functions are usually very complex. Moreover, some of these techniques have bandwidth limitations.

Since standard modulators cannot provide enough SFDR for analog optical link applications, and the linearity techniques are too complex, an optical modulator, which has an intrinsic linear transfer curve and no bias requirements, is highly desirable.

1.4. THE ADVANTAGES OF POLYMER-BASED Y-FED DIRECTIONAL COUPLERS

As shown in Figure 1.2(d), the Y-fed directional coupler (YCM) possesses some intrinsic advantages over other integrated optical modulators. Its built-in 3-dB bias point, deriving from its symmetrical structure, minimizes or even eliminates the need for bias voltage. Furthermore, its performance in terms of modulation linearity can be enhanced significantly (1) by properly selecting its interaction length with respect to its conversion length and (2) by using domain-reversion or alternative-$\Delta\beta$ techniques[11,12]. These properties make the YCM obviously an attractive candidate for fabricating high-linear modulators since the YCM can, by itself, perform high-linear modulation, which is usually performed by a system with complex circuits and with multiple optical components.

The particular properties of the EO material, used to fabricate Y-fed directional couplers are critical for the improvement of modulation linearity (a detailed discussion on this topic can be found in Section 7.2). Compared with LiNbO3 and semiconductor materials as shown in Table 1.2, EO polymers have the following advantages [3, 6]:

(1) Relatively small and non-disperse dielectric constants

In the case of polymers, the dielectric constants in the microwave frequencies are approximately the square of their refractive indexes in optical frequencies. This property results in a small microwave to optical velocity mismatch that is not only important for implementing broadband modulation but also critical for achieving high-linear modulation in high frequencies. Due to their complex structure, high-linear modulators usually have stricter requirements in velocity match than do standard modulators. The performance of some high-linearity modulation techniques based on LiNbO3 modulators degrades quickly along with an increase in operating frequency because of the accumulated phase mismatch. In this respect, EO polymer-based modulators should have much better performance. In addition, the small differences between the refractive indexes of polymers and that of fiber results in small reflective losses between the fiber and the polymer-based devices.

(2) Large EO coefficient

Like other high-linear modulation techniques, a Y-fed directional coupler improves its linearity only with a cost in driving voltage. In order to compensate for this expense, a material with a high EO coefficient is favored. After about two decades of research, EO polymers have surpassed LiNiO3 in EO coefficient. Based on a novel EO polymer PMMA-CLD1, an intensity modulator was achieved with 0.8V half-wave voltage. The recent advances (1) in chromophore synthesis with large molecular nonlinearity and (2) in the chromophore-to-chromophore interactive mechanism exploration in electrical-field-induced polling processes have exhibited great potential in the synthesis of EO polymers with EO coefficients 2-3 times larger than those of typical crystalline materials, and even larger EO coefficients are possible in the future.

(3) Integration capability

The advantages of EO polymers in integration capability come mostly from the applicability of the spin-coating technique. This fact not only makes it possible to integrate polymer EO devices with various electronic and optoelectronic components [5], but also creates the opportunity to fabricate multiple devices stacked in the vertical direction. Metal electrodes can be buried between various polymer layers, making the electrode design quite flexible. To lower the fabrication cost, polymer EO devices can be fabricated directly on top of optical submounts. Besides EO modulators, polymers are also candidate materials for fabricating LEDs, fiber lasers, fiber amplifiers, wavelength converters, variable optical attenuators, tunable filters, and optical switches. Thus it is possible to integrate these functions into one module.

By taking advantage of the structure and the material properties summarized above, EO polymer-based Y-fed directional couplers (YCM) have the potential to be superior to other high-linear modulators in many aspects such as device simplicity, integration capability, and broad bandwidth. However, no such device has been demonstrated and no theoretical analysis has been done on the feasibility of using domain-inversion or alternative-Δβ techniques on a polymer-based YCM to improve its modulation linearity in the high-frequency domain.

1.5. RESEARCH MOTIVATION AND DISSERTATION ORGANIZATION

The attractive properties of EO polymer-based YCMs and the lack of research in this field are the research motivation for this dissertation. The major research topics include:

1) The theoretical study of the high-linear properties of YCMs will be laid out, with emphasis on the influence of traveling-wave (TW) electrode loss and velocity mismatch in the high-frequency domain (Chapter 5, Chapter 7). Although the direct-current (*dc*) properties of YCMs have been studied in reference 10, their high-speed properties have not yet been systemically studied.
2) The dissertation theoretically and experimentally explores traveling-wave electrodes for polymer-based YCMs, including electrode structure, simulation methodology, fabrication, test structure, optimization, etc. (Chapter 6). EO polymer-based directional couplers have their unique requirements for their TW electrodes because of the small waveguide separation and the buried bottom electrodes. Dedicated study on these issues has not been reported yet.
3) This work will demonstrate for the first time a broadband high-linear EO polymer-based Δβ-inverted YCM, and a high-speed bias-free EO polymer-based conventional YCM (Chapter 7). The former YCM achieves approximately 20dB larger distortion suppression than a corresponding MZM

in the frequency range from *dc* to 8GHz. Without a *dc* bias, the latter YCM behaves similarly, in terms of nonlinear distortion suppression, to a quadrature-biased MZM.

4) This document will also demonstrate a domain-inverted EO polymer-based YCM that has a lumped electrode and exhibits a high-linear transfer curve (Chapter 5).

In addition to the chapters mentioned above, in Chapter 2 the EO polymers used in these demonstrations and their poling procedures are introduced. Chapter 3 describes the optical waveguide design, fabrication, and testing. Chapter 4 presents a conventional EO polymer-based YCM with a low half-wave voltage of 3.6V and a high extinction ratio of 26 dB.

Chapter 2 Electro-Optic (EO) Polymer Materials and Their Poling

2.1. INTRODUCTION

Electro-optic (EO) polymers are a classification of second-order nonlinear optical (NLO) EO materials whose optical properties (e.g. the refractive index) can be modulated by an external electrical field. Such materials are members of the more general class of organic NLO materials wherein the nonlinear optical properties arise from the ability of the molecules and atoms to change, in a nonlinear way, their polarization under an external electrical field. Since the late 60's, organic molecules have attracted an increasing amount of interest because of their potential applications in NLO devices and, in particular, in second-order nonlinear optics. This interest is motivated not only by the large, fast, and electronic-in-origin NLO response, but also by the versatility, ease of processing, and possibility of tailoring the physicochemical properties by the molecular engineering approach.

In organic NLO materials, the power series expansion of polarization with an electric field ($\vec{E}$) can be expressed either in terms of molecular polarization ($\vec{p}$) (Equation 2.1) or macroscopic polarization ($\vec{P}$) (Equation 2.2) [6, 13]

$$p_i = p_{i0} + \alpha_{ij} E_j + \beta_{ijk} E_j E_k + \cdots$$

(Equation 2.1)

$$P_I = P_{I0} + \chi_{IJ}{}^{(1)} E_J + \chi_{IJK}{}^{(2)} E_J E_K + \cdots \quad ,$$

(Equation 2.2)

where β is the molecular first hyperpolarizability, and $\chi^{(2)}$ is the macroscopic second-order nonlinear optical susceptibility. In order to have second-order nonlinear properties at the molecular level $(\beta \neq 0)$, the molecules should present noncentrosymmetric symmetry[6,14]. Although second-order nonlinear optical activity can arise from higher order octupolar symmetry[15,16], such materials have yet to be used in the fabrication of devices. Thus, for practical purposes, organic second-order NLO materials can be considered to be made up of dipolar molecules organized into noncentrosymmetric chromophore lattices. This requirement of ordered chromophore lattices, which is indispensable for having macroscopic second order nonlinear properties $(\chi^{(2)} \neq 0)$, is the most daunting materials requirement to be satisfied in the development of electro-optic materials[6].

Dipolar chromophores with larger and larger dipole moments have been successfully synthesized using a (electron donor)-(π-electron connective segment)-(electron acceptor) structure. Several ways have been explored by which noncentrosymmetric lattices have been achieved including Molecular Self-Assembly, Sequential Synthesis Methods, and the Electric Field Poling method. [13,17] Among these methods, the most popular and successful method has been electric field poling of dipolar NLO chromophores containing polymers. In this method, the NLO chromophores are first dispersed into a host polymer, which served as the polymer matrix, either dissolved as guests (guest-host type) or by being chemically connected to the polymer molecules to form side-chain/main-chain polymer (linear type), crosslinked polymer (crosslinked type), or hyperbranched/dendritic polymer (dendrimer type).[6,14] Then the chromophore-containing polymer is cast into a thin film, and an external electrical field is applied to orient the chromophores employing the interaction strength of dipole moment with an applied external electric field. Several such orientation techniques have been developed including (i) static field poling, (ii) photoassisted poling [18-20], and (iii) all optical poling [21,22]. Among them, the static field poling technique is the most successful. In this technique, the chromophore-containing polymers are heated up to around the glass transition temperature, Tg, of the polymer matrix: the chromophore molecules then become mobile and are aligned in the same direction by an applied static electric field. After the polymer is cooled down under a high electric field, the alignment of the electric dipoles is "frozen," and macroscopic optical nonlinearity is achieved. Many static-field poling techniques have been developed, such as electrode (contact) poling (electrodes are deposited for applying the poling electric field), corona (corona discharge is used to create the poling electric field) [23,24], photothermal poling (a laser beam with wavelength lying in the material absorption band is used to heat the thin film) [25,26], and electron beam poling (the poling field is generated by bulk charges provided by a monoenergetic electron beam with an energy of 2–40 keV) [27,28]. Contact and corona poling are the commonly used approach.

After poling, the initially isotropic EO polymer becomes uniaxial, with the extraordinary optical axis parallel to the direction of the poling field. This direction is also chosen as the z-axis in the principal coordinate system. Because of the cylindrical polar symmetry induced by the electrical filed poling, and the fact that only one component of the molecular hyperpolarizability tensor, β_{zzz}, is important for dipolar chromophores, the corresponding EO tensors have only two independent non-zero components. They take the following form [3]:

$$\begin{bmatrix} 0 & 0 & \gamma_{13} \\ 0 & 0 & \gamma_{13} \\ 0 & 0 & \gamma_{33} \\ 0 & \gamma_{13} & 0 \\ \gamma_{13} & 0 & 0 \\ 0 & 0 & 0 \end{bmatrix}$$

(Equation 2.3)

where [6]

$$\gamma_{33} = \left| 2Nf(\omega)\beta_{zzz} < \cos^3\theta > / n_e^4 \right|$$
$$\gamma_{13} = \left| 2Nf(\omega)\beta_{zzz} < \cos^3\theta > / n_o^4 \right| \quad ,$$

(Equation 2.4)

and N is the chromophore number density; $f(\omega)$ is a product of local field factors, taking into account that the applied fields are attenuated by the local environment of the chromophore; n_e and n_o are the extraordinary and ordinary indexes of refraction respectively; and θ is the angle between the chromophores' dipole direction and the z-axis in the principal coordinate system. For electrically poled polymer materials, it is common to assume that $\gamma_{33} = 3(n_o / n_e)^4 \gamma_{13}$ [17]. However, it should be noted that such is not always the case [29,30] and is seldom the case with the use of laser-assisted (photochemical) poling.

The index ellipsoid for EO polymers in the presence of an electric field is represented by

$$x^2\left(\frac{1}{n_o^2} + \gamma_{13}E_z\right) + y^2\left(\frac{1}{n_o^2} + \gamma_{13}E_z\right) + z^2\left(\frac{1}{n_e^2} + \gamma_{33}E_z\right)$$
$$+ 2yz\gamma_{13}E_y + 2zx\gamma_{13}E_x = 1 \quad ,$$

(Equation 2.5)

where E_x , E_y and E_z are the three components of the applied external electrical field. (Equation 2.5 shows that the most efficient direction to apply the modulation electrical field is the poling (z-axis) direction. For optical polarization along the z-axis (TM mode) and perpendicular to the z-axis (TE mode), the optical refractive indexes become [3]

$$n_{TM}^{'} = \left(\frac{1}{n_e^2} + \gamma_{33}E_z\right)^{-\frac{1}{2}} \approx n_e - \frac{1}{2}n_e^3\gamma_{33}E_z$$

(Equation 2.6)

and

$$n'_{TE} = \left(\frac{1}{n_o^2} + \gamma_{13} E_z \right)^{-\frac{1}{2}} \approx n_o - \frac{1}{2} n_o^3 \gamma_{13} E_z$$

(Equation 2.7)

respectively. (Equation 2.6 and (Equation 2.7 show that EO polymer-based devices are generally polarization-dependent. For modulation application, TM optical modes are desirable since they are much more efficiently modulated than are the TE optical modes because of the relatively larger value of γ_{33} over γ_{13}.

The three EO polymers used in this research are introduced in Section 2.2, and their poling processes are described in Section 2.3.

2.2. EO POLYMER MATERIALS

Three EO polymer materials, DR1/PMMA, FTC/PU, and CLD1/APC, as listed in Table 2.1, were employed to build EO modulators in this research. Table 2.1 also gives the corresponding cladding materials, which were employed to fabricate optical waveguides using the procedure described in the next chapter. Figure 2.1 shows the molecular structures of these chromophores.

Table 2.1 EO polymer and cladding materials

Wave guide number	**Bottom cladding**		**EO polymer**				**Top cladding**	
	Polymer	**Provider**	**Chrom-ophore**	**Host polymer**	**Dispersion method**	**Provider**	**Material**	**Provider**
1	UV15 (UV-curable)[l]	Master Bond, Inc.[a]	DR1[b]	PMMA[c]	Side-chain	IBM[d]	UV11-3 (UV-curable)	Master Bond, Inc.[a]
2	U9120[e]	Amoco Chem.[f]	FTC	PU[g]	Cross-link	L. Dalton Group, UW[h]	NOA61[i] (UV-curable)	Norland Prod., Inc.[j]
3	UV15 (UV-curable)	Master Bond, Inc.[a]	CLD1	APC[k]	Guest-host	L. Dalton Group, UW[h]	UV11-3 (UV-curable)	Master Bond, Inc.[a]

a. Master Bond Inc. 154 Hobart Street, Hackensack, New Jersey 07601.
b. DR1: Dispersion Red 1
c. PMMA: poly(methylmethacrylate)
d. IBM: International Business Machines Corporation, New Orchard Road, Armonk, NY 10504.
e. U9120: Ultradel® 9120D polyimide
f. BP Amoco, Naperville, IL 60563
g. PU: polyurethane
h. Larry Dalton, Dept. of Chem., Univ. of Washington, Seattle, Washington, 98195-1700.
i. NOA61: Norland Optical Adhesive 61
j. Norland Products Inc., 2540 Route 130, Suite 100, P.O. Box 637, Cranbury, NJ 08512
k. APC: Amorphous polycarbonate
l. UV curable: The material is UV curable. The materials without the UV-curable label in this table were cured thermally.

The azo dye Dispersion Red 1 (DR1) dispersed in poly(methylmethacrylate) (PMMA) is the first EO polymeric material which was successfully poled by electrical field in 1986 [31]. Thereafter, DR1/PMMA has been widely used to explore poling conditions and mechanisms [14,32] and it is commercially available now. In this research, side-chained DR1/PMMA, provided by International Business Machines Corporation (IBM), was used to explore the poling conditions and traveling-wave electrode structures.

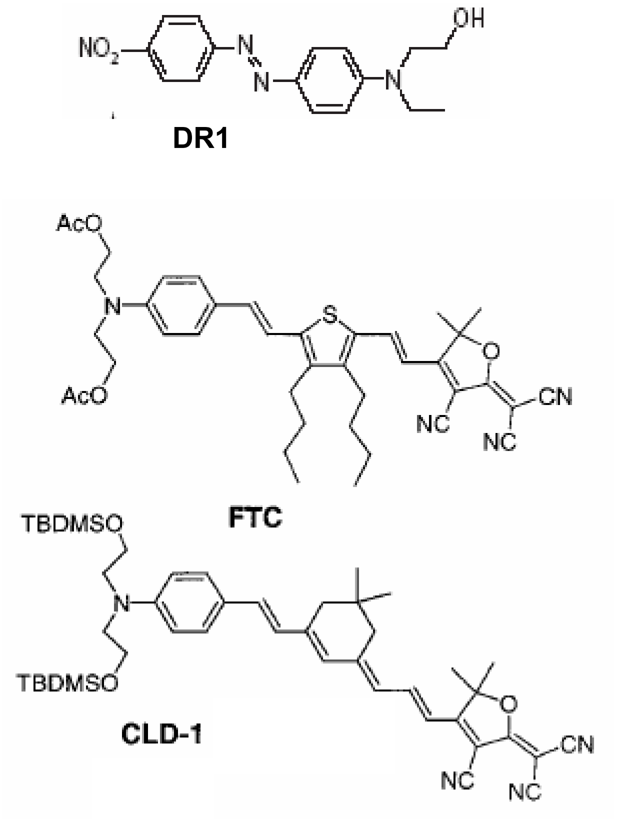

Figure 2.1. Chemical structures of nonlinear chromophores DR1, FTC, and CLD1

The dipole moment of DR1 is relatively small for fulfilling the task of fabricating low driving-voltage EO modulators. FTC was the first chromophore that exhibited high nonlinearity induced by a novel tricyanobutadiene acceptor with a furan-derivative [33]. The invention of this efficient acceptor has greatly accelerated progress in improving the nonlinearity of the chromophore. The three cyanogroups in this acceptor are aligned along the charge-transfer direction of the chromophore; thus they can pull the electron more efficiently so as to provide relatively large dipole moment (12–15 Debye). The two butyl groups on the thiophene increase the solubility and reduce the interchromophore electrostatic interaction, in turn leading to aggregates. The FTC chromophore has excellent solubility, and high chromophore thermostability (>300 ^{o}C). To enhance the thermal stability, a hydroxyl functionalized FTC chromophore was synthesized by adopting a single-end crosslinked polyurethane (PU) system. Thermoset polyurethanes have been widely used to stabilize the polar alignment of a nonlinear optic polymer. The FTC chromophore is mixed with toluene diisocyanate (TDI) in a solvent and heated to attach the NCO groups to the OH groups. Next, the crosslinker, triethanolamine (TEA), was added, acting to form a 3-D network during the pre-curing and the final hardening during poling. Excess TDI and TEA can be added to control the density of the chromophores. The resulting cross-linked FTC/PU has excellent thermal stability and is used to fabricate EO directional couplers working at the 1.3 μm wavelength.

The basic structure of the CLD [33] chromophore is obtained by replacing the thiophene unit in FTC with a diene. The aromatic resonance energy of the bridge is reduced to increase the nonlinearity of CLD1. The two bulky -butyldimethylsilyl groups used in CLD1 enhance the molecular cross-section so that aggregates are less likely to form. They also reduce the interchromophore interaction during the poling process so as to increase the poling efficiency [34]. Amorphous polycarbonates (APC) [6] is one of the currently most investigated group of host materials because of its high thermal stability and low loss at the 1.55 μm wavelength [35]. APC is quite compatible with virtually all high-μβ chromophores and has a glass transition temperature (Tg = 205 °C) in the appropriate processing range. Materials prepared using APC typically exhibit thermal stability of the acentric chromophore order up to 120 °C or greater. This is sufficient for some applications. APC also has the advantage of having a very favorable dielectric constant and is compatible with a variety of substrates and cladding materials. Meanwhile, APC has low loss at 1.55

μm wavelengths. When CLD-1 was used in the APC host, 90 pm/V at 1060 μm was obtained. In this research, guest-host CLD1/APC was used to fabricate EO directional couplers working at the 1.55 μm wavelength.

2.3. POLING PROCEDURES

To build EO modulators, EO polymer-based optical waveguides were fabricated as will be described in Section 3.4. The EO polymer cores were either corona poled during the waveguide fabrication (after core layer coating, but before RIE) or contact poled after the waveguide fabrication.

2.3.1. Corona poling

FTC/PU was poled using the corona poling method. Before the poling, the bottom electrode, bottom cladding, and FTC/PU film were deposited using the fabrication process to be described in Section 3.4. The schematic diagram of our corona poling setup is shown in Figure 2.2. To optimize the poling result, different poling conditions such as curing temperature, time, and pre-cure processes were investigated extensively to achieve the best EO coefficient without damaging the polymer surface. The typical needle-to-plane distance was about 2cm and the DC voltage of 8 kV was applied. As shown in Figure 2.3, the poling profile consisted of two major steps: pre-curing and electrical poling. During the pre-curing step, the optical polymer was heated quickly from room temperature to 120^{o}C for slight hardening, kept at that temperature for only 3 minutes, and then reduced to 110^{o}C. This step was to initiate partial crosslinking prior to applying high voltage. This procedure was to prevent surface damage due to the electric charges induced by the corona needle. There was a tradeoff between the pre-curing and the poling efficiency. When the pre-curing was not sufficient, surface damage occurred, while with excessive pre-curing the rotation of the chromophores was restricted, and the poling efficiency was reduced. During the actual poling, an 8 kV DC voltage was applied to the corona needle, with the film temperature fixed at 110°C for 60 minutes, until the aligning of the chromophores and the crosslinking of the polymers were completed.

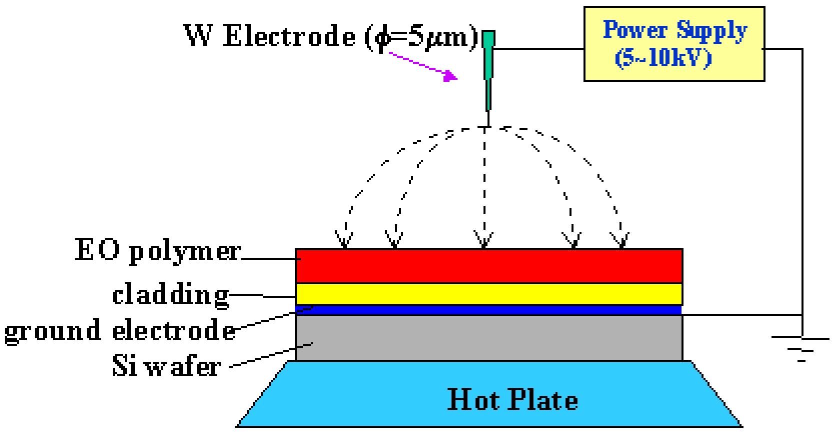

Figure 2.2. Schematic of Corona poling setup

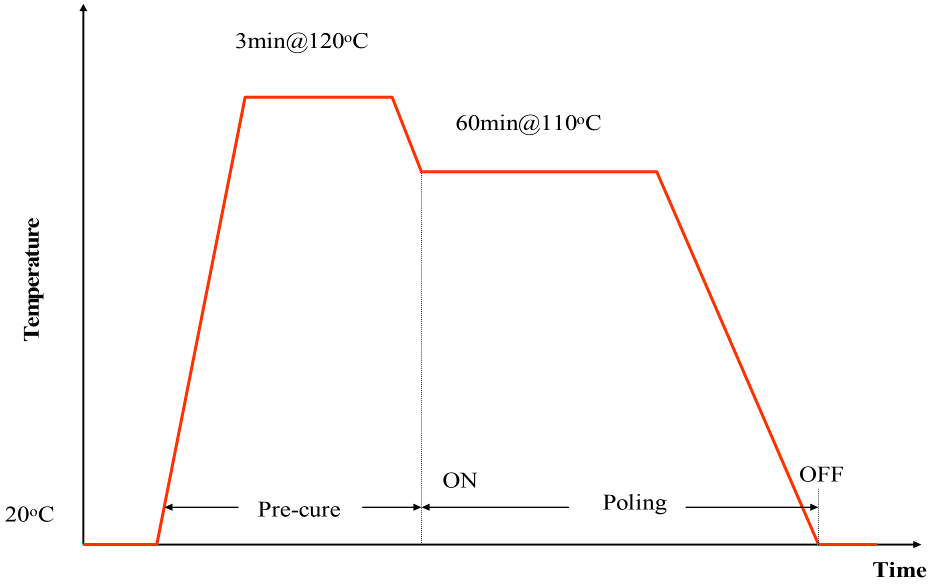

Figure 2.3. The corona poling temperature profile for the FTC/PU polymer

For the thermosetting material, lattice hardening took place during poling; it can reduce the poling efficiency by preventing some of the chromophore from reorienting under the influence of the poling field. Experiments confirmed that a well-controlled pre-cure step was very critical, otherwise either lower poling efficiency or damaged film would result. The surface damage was attributed to the strong compressive electrostatic force of the charges accumulated on the film, since the charged particles may carry large kinetic energy when they pass through the high electric potential between the corona needle and the ground electrode.

In addition, it was found that poling temperature affected the thermal stability of the EO film. Too low poling temperature resulted in poor EO coefficient and thermal stability. For FTC/PU, 100~110^{o}C was the best poling temperature. Figure 2.4 shows a FTC/PU sample coated onto a 3” silicon wafer. Notice the color change for the center area (about 4cm in diameter) where corona poling was performed.

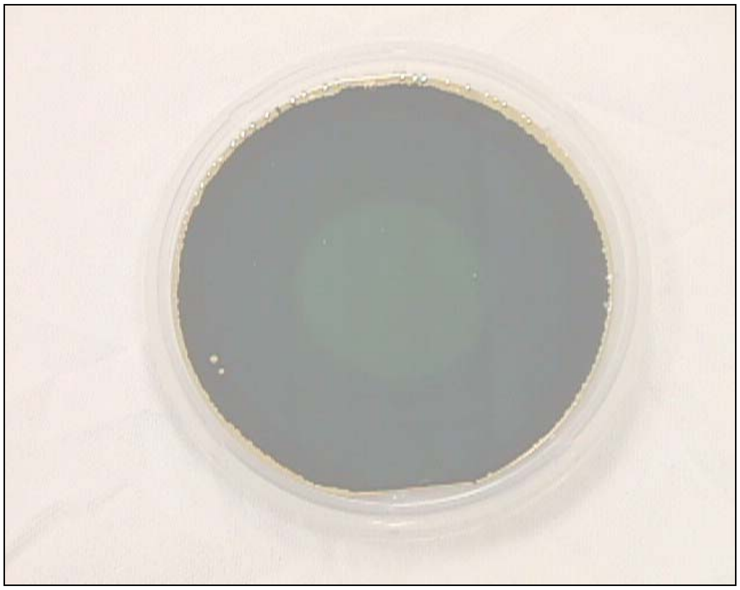

Figure 2.4. A corona poled wafer coated with FTC/PU. The poled area (a circle 3 - 4cm in diameter) near the center of the wafer changed its color compared to the original film.

2.3.2. Contact poling

An advantage of contact poling over corona poling is that deferring the poling until the top cladding is cured or even until the top electrode is processed protects the poling-induced chromophore alignment from decay during the thermal or UV-curing processes on the top cladding and the top electrode. CLD1/APC- and DR1/PMMA-based waveguides fabricated following the fabrication procedure given in Section 3.4 were poled using the contact poling method. Figure 2.5. shows the schematic of the contact poling set-up. The temperature was controlled by a Thermo-Electric Cooler (TEC). It was found that high temperature can increase the poling efficiency, but will reduce the resistance of the polymer layer to a high electrical field. High voltage will increase the poling efficiency, but meanwhile increase the risk of breakdown and may induce too large current, which can damage the polymer. Extensive experiments were done to explore these poling parameters. Figure 2.5 shows a typical poling process for a DR1/PMMA sample with a poling area of around 0.1cm^2. In Phase I, the sample was first heated up to 115°C; the voltage was increased gradually to 1000 volts. The monitored current between the top and the bottom electrodes increased rapidly along with the voltage and reached its peak value when the voltage reached its own maximum value. In Phase II, the voltage and the temperature were maintained for 20 to 30 minutes; the current was then reduced gradually. In Phase III, the sample was cooled down to room temperature. After keeping the high voltage for a few minutes in Phase IV, the voltage was reduced to 0 V, at which time the poling process was finished. Poling time is a flexible parameter. Experiments show that a long poling time can compensate for the low poling efficiency of low temperature and low voltage. For example, a EO coefficient (r33) of 11pm/V obtained by poling DR1/PMMA for 15 minutes at 120°C with 1000V was also achieved by 30-minute poling at 115°C with 900V. CLD1/APC was poled using the same procedure, except that the poling temperature was 120-125°C, the voltage was 700-800V, and the poling time was around 30 minutes.

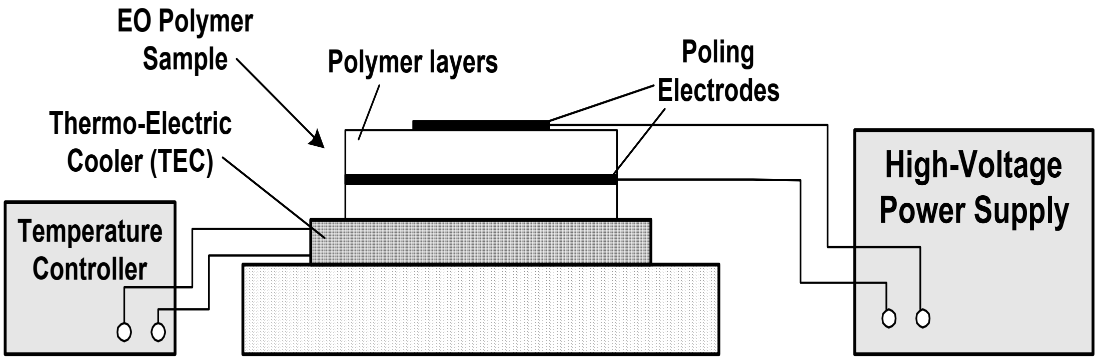

Figure 2.5. The schematic diagram of the contact-poling setup for polymer-based EO modulators

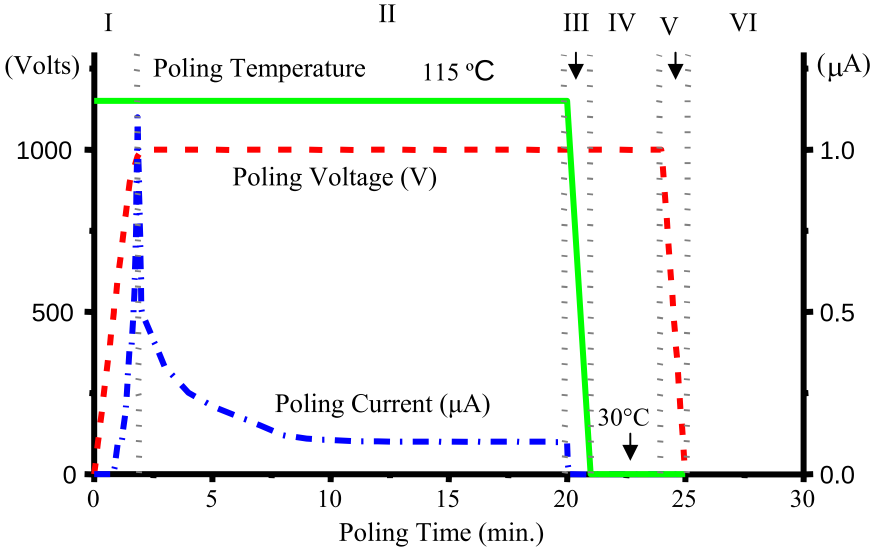

Figure 2.6. Typical parameters of applied temperature, voltage, poling time, and the monitored electric current in our poling experiments

2.3.3. Two-section domain-inverted contact poling

The availability of domain inversion through poling in electro-optic polymer is a cornerstone for high-performance EO devices. Due to polymer's spin-coating flexibility onto any desired substrate, different sections of one polymeric waveguide can be poled into opposite directions, *i.e.*, domain inversion of $\Delta\beta$. Many novel EO devices can be built based on such types of domain-inverted waveguides [36-38].

The effective way to invert the polymeric domain is to electrically pole the polymer film simultaneously in two opposite directions. As a result, all corresponding physical parameters, such as the electro-optic coefficient, are inverted with respect to each other. Notice that the corona poling technique is not suitable for fabrication of domain-inverted polymers, where a high electric field, produced by the charge dropped on the film surface, points in one direction. Besides, it is also difficult to precisely control the poling area under the electric corona.

In order to obtain the proposed domain-inverted polymeric waveguide, a novel contact poling technique was developed to pole FTC/PU films. The schematic diagram is illustrated in Figure 2.7. EO polymer film was prepared with the method described in Section 3.4. The top electrode is patterned to define the two domain regions, and a 50μm-wide by 25μm-tall insulating wall, made with photoresist AZ4620, was employed to separate the two poling electrodes.

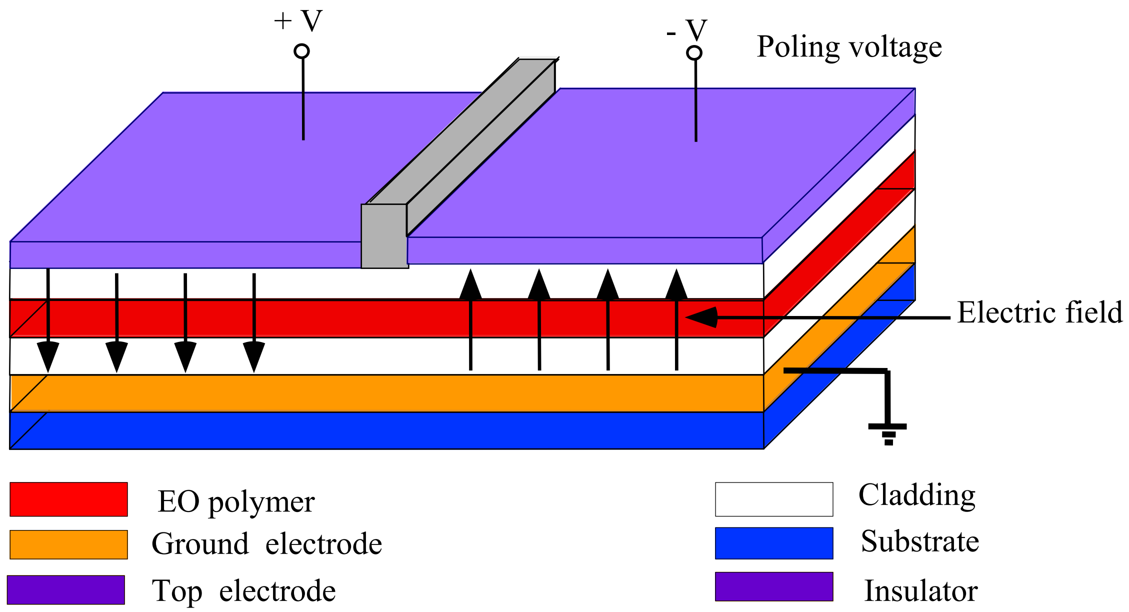

Figure 2.7. Schematic diagram for obtaining domain-inverted polymers using an electric contact poling technique.

Two electrical voltage supplies were employed for poling the polymer, sharing a common ground (bottom electrode), as shown in Figure 2.7. During the poling the same voltage is applied to the two top electrodes with reversed polarities. Note that the gap between the two top electrodes is much larger than the distance between the top electrodes and the bottom electrode, so the electric field is perpendicular to the polymer film, except for small areas near the center edges. The length of this area should also be small enough to ensure the designed device's performance.

The experiment was carried out in an ambient environment. We used a similar poling profile similar to the one described in the corona poling section (Figure 2.4). The sample was raised to 120°C for 3 minutes for pre-curing. The electrical poling field was applied while keeping the sample's temperature fixed at 110°C. After poling for 60 minutes, the hotplate was turned off, but keeping the poling voltage on until the sample's temperature had been reduced to room temperature. The breakdown voltage was determined to be around 920V. A typical poling voltage of 850V, corresponding to a strength of ~110V/μm on average, was used for real device poling.

2.4. EO COEFFICIENT MEASUREMENTS

Mach-Zehnder (MZ) modulators were designed and fabricated to estimate the poling-induced EO coefficients.

For an MZ modulator, it is a simple matter to derive the following formula:

$$r_{33} = \frac{\lambda d}{n^3 V_\pi \Gamma L} \quad ,$$

(Equation 2.8)

wherein λ is the wavelength in free space, d is the distance between the top and bottom electrodes, n is the waveguide effective index, V_π is the half-wave voltage, Γ is the overlap factor, and L is the electrode length. (Equation 2.8 was used to estimate the γ_{33} values based on the measured V_π, and the calculated Γ. Γ was calculated based on the waveguide dimensions in the following way: the electrical field was first calculated by solving the Posion equation, then the index change was determined based on the modulation field, and finally, the phase shift was calculated using the BPM method.

Figure 2.8 shows the measured modulation curve (dots) of a DR1/PMMA-based MZ modulator. The solid line is the fitted sinusoidal line. In this example, $V_\pi \approx$45V (based on Figure 2.8), λ=1.55μm, d=12μm, $\Gamma \approx$0.64, and L=16mm; the r_{33} was calculated to be 11.1 pm/V.

The γ_{33} values of the poled DR1/PMMA, FTC/PU, and CLD1/APC were estimated to be 11, 28, and 33 pm/V respectively.

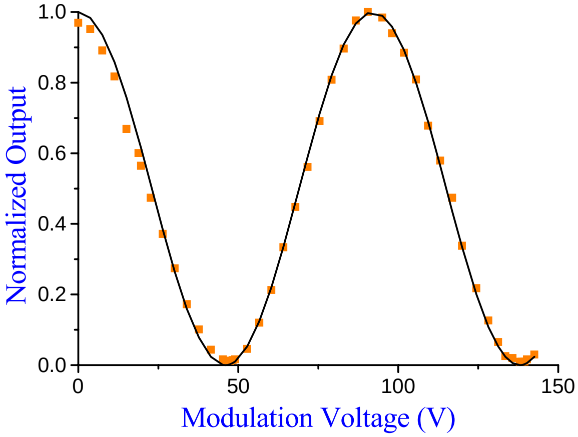

Figure 2.8. Modulation curve of a Mach-Zehnder modulator based on contact-poled DR1/PMMA

2.5. SUMMARY

The physics mechanism, synthesis method, and working principle of EO polymers were generally introduced in this section. The three EO polymers DR1/PMMA, FTC/PU, and CLD1/APC, which were used to fabricate EO modulators in this dissertation research, were described. These polymers were successfully poled by employing the contact poling and corona poling procedures given in Section 2.3. A standard MZM was designed to estimate the poling-induced EO coefficients.

Chapter 3 EO Polymer-based Optical Waveguide Design and fabrication

3.1. INTRODUCTION

To form an optical waveguide, optical confinement in the vertical direction is achieved by sandwiching the core EO layer between two cladding layers of different polymer materials with lower refractive index than that of the core. To provide horizontal confinement, a higher index channel in the active layer must be fabricated and surrounded by lower-index materials. This higher index channel can be fabricated using a variety of procedures [13], including the following: (1) photochemical processing exploiting photoinduced conformational changes; (2) electron cyclotron resonance (ECR) and reactive ion etching (RIE) using ions present in an oxygen plasma; (3) spatially selective poling taking advantage of the refractive index changes induced by poling; and (4) laser ablation techniques using excimer lasers and other forms of UV irradiation. RIE is a popular method and was the method used here.

The modulation electrical fields are usually applied through a pair of electrodes: a bottom electrode beneath the bottom cladding and a top electrode resting on top of the top cladding layer. These electrodes can be deposited using regular metal deposition methods such as sputtering and electron-beam deposition. For high-speed applications, electroplating is usually employed to increase the electrode thickness to several microns in order to reduce the resistive loss.

An EO polymer-based device can be packaged either as a stand-along device or be integrated into other devices on the same chip. At the ends of the EO polymer-based waveguides, the light is coupled into or from fibers or waveguides based on other materials. In some cases, certain transition structures may be fabricated at the end of the waveguides to reduce the coupling losses [39].

3.2. CLADDING MATERIALS

The deposition of the cladding layers must be compatible with the active electro-optic layer. In particular, the solvents used in the spin casting of the active layer must not dissolve the bottom cladding layer, and the solvents used in spin casting the top cladding layer must not dissolve the active layer. Meanwhile, the curing process of the top cladding layer must not cause damage to the active layer. Furthermore, the cladding materials should also exhibit appropriate refraction indexes, excellent thermal and photochemical stability, and low optical losses. Many materials have been tested by us to serve as the cladding materials, including UV15, UV11-3, NOA61, Epoxylite9530, U9020D, U9120D, UV15LV. Out of these, three groups of EO polymer and cladding materials (e.g. UV15:DR1/PMMA:UV11-3, U9120:FTC/PU:NOA61, and UV15:CLD1/APC:UV11-3), as listed on Table 2.1, have proved to be suitable for fabricating optical waveguides.

UV15 and UV11-3 are UV-curable epoxies produced by Masterbond Company. UV15 has good adhesion to metals, silicon, and silicon dioxide and is compatible to the solvents for spin-coating DR1/PMMA and CLD1/APC. UV11-3 does not attack the core layers and is compatible to metal (such as Cr-Au and Al) top electrodes. Ultradel® 9120D is negatively photosensitive polyimide used in optical waveguide and multi-player coating. Its glass transition temperatures are about 420 ^{o}C. Its high thermal stability, good adhesion to substrates, and compatibility to core materials make it excellent bottom cladding material. Norland Optical Adhesive 61 (NOA 61) is a clear, colorless, liquid photopolymer that will cure when exposed to ultraviolet light. NOA 61 is cured by ultraviolet light with maximum absorption within the range of 350-380 nanometer with a light intensity of 3 Joules/cm^2. The cure is not inhibited by oxygen. NOA 61 also has excellent clarity, low shrinkage, and slight flexibility that make it superior to other materials as an optical adhesive. More properties of these cladding materials can be found on Table 3.1.

3.3. WAVEGUIDE DESIGN

There are several design requirements for the waveguides used in polymer modulators. First, the waveguides must be single-mode to provide a high extinction ratio. Second, the loss, including the propagation loss and the coupling loss between the waveguide and fiber, should be as small as possible. Third, the modulation efficiency should be as large as possible, which condition is achieved by increasing the portion of light propagating in the EO polymer layer and by reducing the total thickness of the active and cladding layers.

After choosing the proper materials, the refractive indexes of the waveguide materials listed on Table 2.1 are measured using the prism-coupling method by spin-coating thin films of these materials with the fabrication procedure described in Section 2.3.1. The results are given on Table 3.1 (some data are cited from references, as indicated in the table).

Table 3.1 The refractive indexes of EO and cladding polymers

Waveguide	Bottom cladding		Core		Top cladding	
	Material	Refractive index (TM @ 1550nm)	Material	Refractive index (TM @ 1550nm)	Material	Refractive index (TM @ 1550nm)
1	UV15	1.501	DR1/PMMA	1.55	UV11-3	1.506
2	U9120	1.5402 (@ 1340nm)	FTC/PU	1.6500[a] (@ 1340nm)	NOA61	1.5398 (@ 1340nm)
3	UV15	1.501	CLD1/APC	1.612[b]	UV11-3	1.506

a: reference [59] b: reference [33]

Because EO polymers have a relatively high index of refraction compared to the passive cladding polymers, EO polymer-based waveguides usually have a buried rib structure which has a relatively larger cross-section (inducing smaller coupling loss) compared with the corresponding rectangle structure, meanwhile maintaining as single-mode.

It has been widely accepted that, in order to keep the waveguide single mode, the thickness of the core layer must be thin enough to suppress higher-order modes in its slab waveguide. To do so at a 1.55μm wavelength requires that the typical thickness of the EO polymer layer be less than 1.5 μm. However, the small vertical mode size in the thin waveguide leads to a high coupling loss and low modulation efficiency, since only a small portion of the light is traveling in the active polymer.

In order to avoid this problem, the large cross-section-design approach is employed here, in which even the core layer is so thick that it could support several modes in its slab waveguide; the rib waveguide can still be designed to confine only one mode by radiating the higher order modes horizontally into the slab modes [40-42]. The principle of this approach is illustrated in Figure 3.2, which is actually a schematic of the effective indexes of the UV15:CLD1/APC:UV11-3 planar waveguide as a function of the core layer thickness. For a rib waveguide with the core layer thickness and rib depth given in Figure 3.2, more than one slab mode exists at the center of the rib waveguide. However, since the effective index of the first-order mode N_1 (center) is smaller than the effective index of the fundamental slab mode of the waveguide side N_0(side), those high-order modes will dissipate into the slab mode of the waveguide side regions. If a proper rib depth is chosen which not only satisfies the dissipation condition but also provides a proper lateral confinement in such a way that only one lateral mode is confined, the resulting waveguide will be single-mode. This principle has been proven experimentally. In practice, the core layer thickness is also limited by material properties and fabrication procedures. After comprehensive evaluations, the rib structures were designed using the effective index method (EIM) and the beam propagation method (BPM) following the large cross-section approach. The results are shown on Table 3.2. In addition to the three specific rib depths, Table 3.2 also lists the largest rib depths which satisfy the single-mode requirement. These values are useful in later directional coupler fabrications, since the rib depth is usually adjusted to fine-tune the interaction length.

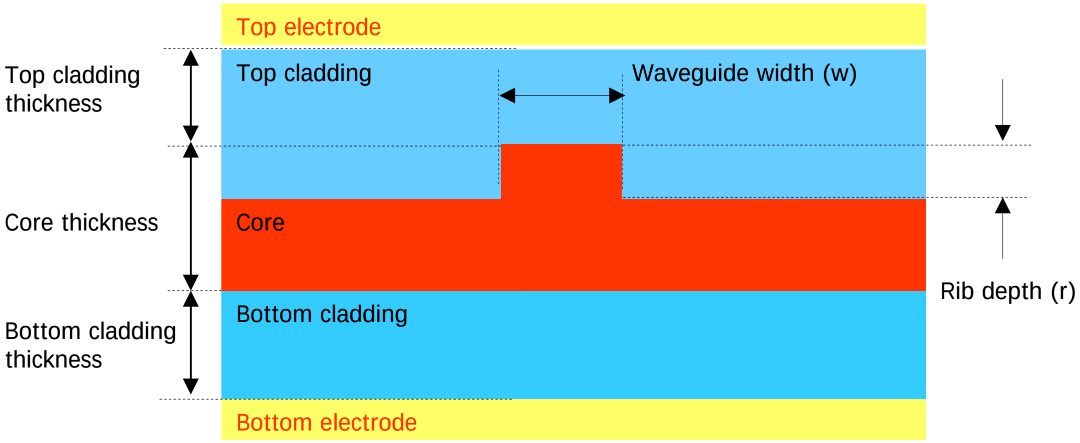

Figure 3.1. Schematic of the buried rib waveguide

The minimum thickness of the cladding layer is determined by setting the metallic absorption loss caused by the surface plasmon coupling to the upper or lower electrodes to an acceptable value (< 0.1 dB/cm). Making the cladding layer thicker than this minimum only increases the driving voltage. To find the minimum thickness, the effective index of the multilayer planar waveguide structure, including the two metal electrode layers, was calculated. The imaginary part of the effective index is then used to obtain the metallic absorption loss. The designed cladding thicknesses are also given on Table 2.3.

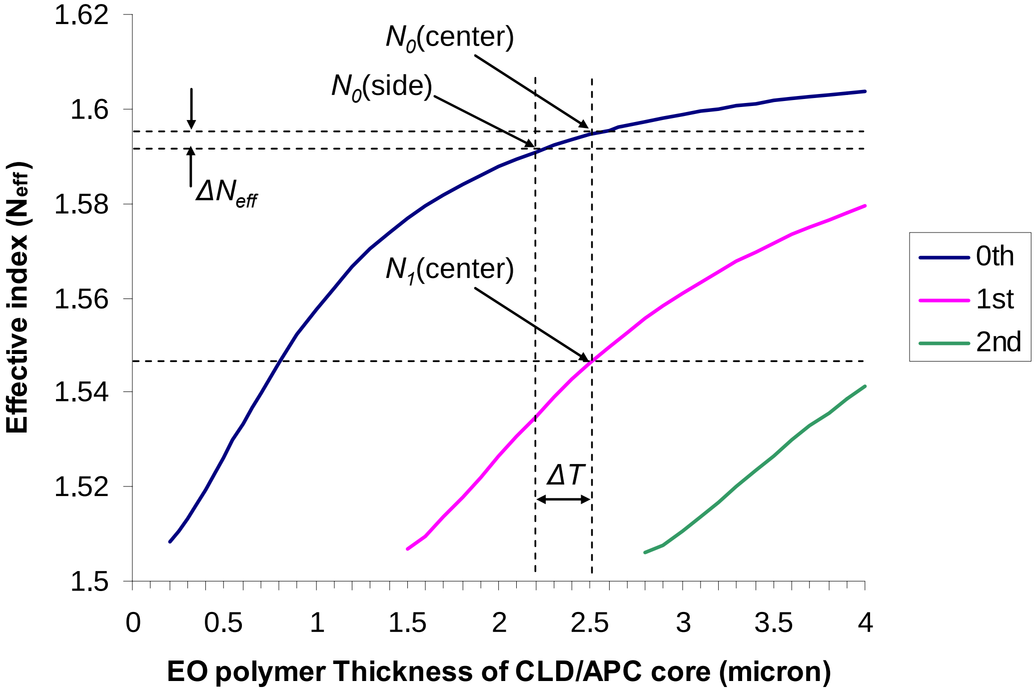

Figure 3.2. The effective index of the planar waveguide as a function of the thickness of the core layer. The waveguide consists of UV15 lower cladding (1.501), CLD/APC core layer (1.612), and UV11-3 upper cladding (1.506). In the rib waveguide structure, the waveguide side needs to be etched by ΔT to obtain the effective index contrast of ΔN_{eff} for the fundamental mode.

Table 3.2 Waveguide and electrode parameters

Waveguide parameters												
Waveguide #	**Material**					**Waveguide parameter**						
	bottom cladding	**core**	**top cladding**	**bottom electrode**	**top electrode**	**bottom cladding thickness (μm)**	**core thickness (μm)**	**bottom cladding thickness (μm)**	**waveguide width (um)**	**rib depth (μm)**	**rib depth range (μm)**
1	UV15	DR1/PMMA	UV11-3	Al (2000-5000Å)	Al (2000-5000Å)	4.00	4.00	4.00	4.00	1.2	<=2.17 (<1.57)
2	U9120	FTC/PU	NOA61	Cr (50Å) Au (2000Å)	Al (2000-5000Å)	3.00	2.00	3.00	4.00	0.30	<=0.45
3	UV15	CLD1/APC	UV11-3	Cr (50Å) Au (30000Å)	Cr (50Å) Au (30000Å)	3.00	2.50	3.00	4.00	0.30	<=0.76 (<0.57)

3.4. WAVEGUIDE FABRICATION

The waveguides were fabricated in a Class 100 cleanroom following the procedures described in this section. Note that only the three cladding and core combinations UV15:DR1/PMMA:UV11-3, U9120:FTC/PU:NOA61, and UV15: CLD1/APC:UV11-3 were implemented.

3.4.1. Substrate and bottom electrodes

Silicon wafers are used as the device substrate. A 2-μm thick silicon dioxide layer is usually formed by thermal oxidation on the top surface to prevent electrical breakdown in the contact poling process as described in Section 2.4. Wafer pre-clean is essential for satisfactory coating quality and interface adhesion. The wafers were cleaned in an ultrasonic bath as follows: Acetone (5 min.) → Methanol (5 min.) → DI H_2O (5min.) → Baking (15min @ 120°C).

Metal layers were deposited as the bottom electrode, as indicated on Table 3.2, using the e-beam or sputtering method. These metals were chosen based on their properties, such as adhesion to the substrate and the bottom cladding and thermal expansion. Aluminum (Al) is an excellent bottom electrode material which has outstanding adhesion to both the substrate and the bottom cladding and is easy to process (wet etch, patterning etc.). Chromium (Cr) was used to enhance the adhesion of the gold (Au) on the silicon wafer. A thick Au layer can efficiently reduce the Ohm loss for high-speed modulation.

3.4.2. Bottom claddings

UV15: A film coated with original UV15 supplied by Masterbond, Inc., was of poor quality (with particle-like contaminations); moreover it is difficult to coat thin film (3~4 μm) using this material, because of its large viscosity. These problems were solved by diluting UV15 with cyclopentanone in a volume ratio of 2:1 (UV15 : cyclopentanone) and filtering the solution with 0.2 μm filters. The diluted UV15 was used to coat 3~4 μm thick films at a rotation speed of 2000~3000 rpm. The films were UV-cured for 30 min. using a mercury lamp with an intensity of around 10 mW/cm^2, and then thermally cured at 90°C overnight. The resulting films have good quality and excellent resistance to cyclopentanone (solvent of DR1/PMMA) and 1,2-dichloroethane (solvent of CLD1/APC).

U9120D: Promoter A600 (Amoco, Inc.) was first coated on to improve adhesion, and then 3μm-thick U9120D films were spin-coated and cured in an N_2-purged oven. Figure 3.3 illustrates a typical curing process.

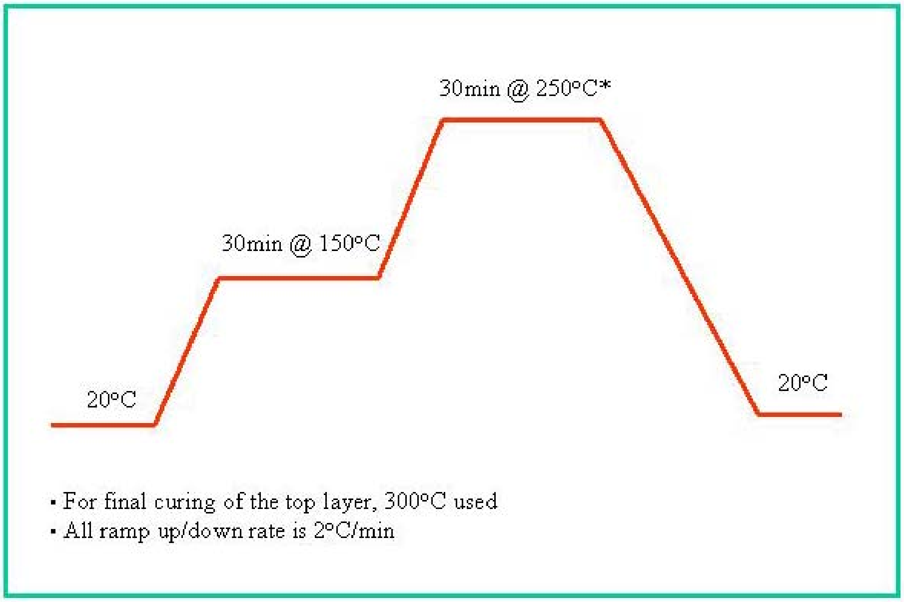

Figure 3.3. U9120 curing profile

3.4.3. EO polymer cores

DR1/PMMA: The solution of DR1/PMMA was prepared by dissolving DR1/PMMA powder into cyclopentanone with a mass to volume ratio of 0.2(mg):1(ml). After being filtered with 0.2-µm filters, the solution was used to coat a ~4-µm thick core layer with a spinning speed of about 700 rpm. The resulting DR1/PMMA film is then thermally cured in a 90°C oven overnight.

FTC/PU: As described in Chapter 2, to prepare an FTC/PU solution, the FTC chromophore is mixed with toluene diisocyanate (TDI) in a solvent and is heated to attach the NCO groups to the OH groups. Then the crosslinker, triethanolamine (TEA), was added. Dioxane is the solvent used in this process. Polymer film was spin-coated following the solution preparation, and the coated sample was dried thoroughly in a vacuum oven overnight at room temperature. The 3-D cross-links in the FTC/PU films were formed during pre-curing, and the final hardening occurred during the poling process described in Chapter 2.

CLD1/APC: The selection of solvent is critical to the film quality of guest-host materials. 1,2-Dichloroethane was chosen as the solvent because its low boiling point (83 °C) ensures fast solvent evaporation (typically in 10 sec.), which is necessary for reducing the degree of chromophore phase separation. This separation can hardly be avoided when high-boiling-point solvents are used. To prepare the coating solution, the CLD chromophore was mixed with the APC polymer in a concentration of 25 wt%. Then, a 10 wt/v% solution of CLD1 was used to spin films of 2~3 μm thickness at spin rates of 800-1100 rpm. The spin time is typically limited to 2 sec. to prevent wrinkles on the film which would be caused by the inhomogeneous drying of the solvent. After spinning, the core layer was dried in a vacuum for 1 hr., and then baked at 120°C for 1 hr. to remove the residual solvent.

3.4.4. Waveguide patterning

The standard photolithography process was used to pattern the waveguide, and Reactive Ion Etching (RIE) was employed to transfer these patterns to the core layer. It was experimentally proved that a photoresist film with a thickness larger than 1 μm is strong enough to serve as the RIE mask to etch a rib waveguide with an etch depth in the desired ranges listed on Table 3.2 for all three core materials.

Photoresist can be directly applied to the FTC/PU and DR1/PMMA films without causing damage. However, the CLD1/APC material was difficult to process using standard lithography, because the film could be dissolved easily during the photoresist coating. To protect the CLD1/APC core layer from being damaged by the photoresist, we coated an additional thin layer of UV-15 on the core layer using methanol as the solvent (methanol is a nonsolvent for APC and CLD1). Methanol-diluted UV-15 with a volume ratio of 6:1 (methanol : UV15) was prepared in order to coat on a ~0.5 μm thick UV15 film with a rotation speed of around 6000rpm. After the protective UV15 film is UV-cured, photolithography can be performed over it. Figure 3.4 shows the fabrication steps for the CLD1/APC waveguide. Note that the protective UV15 film was cured instantly using a large intensity UV light to prevent it from cracking.

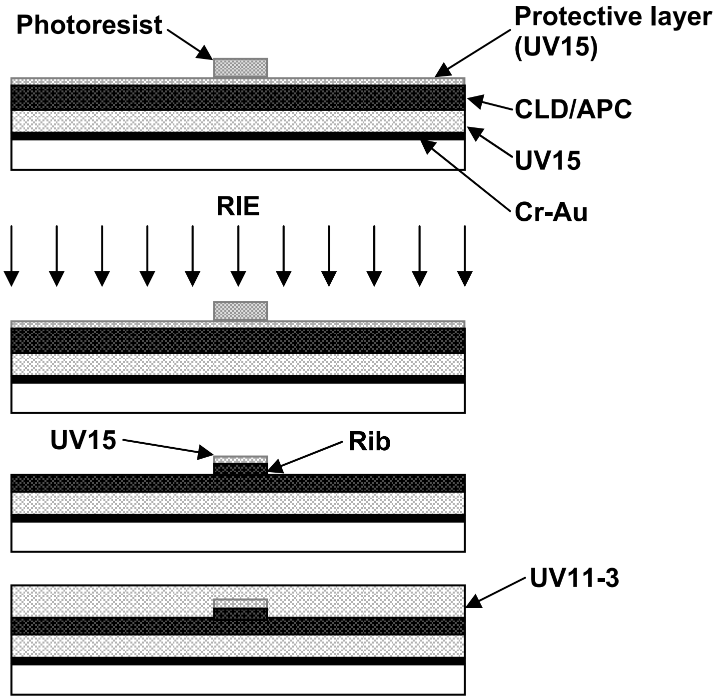

Figure 3.4. Schematic diagram of the UV15:CLD1/APC:UV11-3 waveguide fabrication procedure.

3.4.5. Reactive ion etching (RIE)

All the RIE processing parameters, such as plasma pressure, RF power, gas flowing fluxes, and etching time, were optimized experimentally to make an ideal optical waveguide. The optimized parameters are listed on Table 3.3.

Table 3.3 RIE conditions for EO polymer etching

Core materials	DR1/PMMA	FTC/PU	CLD1/APC
Mask	AZ 5209	AZ 5214	AZ 5209
Pressure	75 mTorr	350 mTorr	75 mTorr
Gas flow rate	O_2: 20 sccm N_2: 8 sccm	O_2: 50 sccm	O_2: 20 sccm N_2: 4 sccm
RF power	35 W	0.04 W/cm^2	120 W
Etch rate	0.074 µm/min	0.05-0.06 µm/min	0.16 µm/min

N_2 was added to O_2 to obtain more stable etch rates for the DR1/PMMA and FTC/PU etches. Figure 3.5 (a) and (b) show the etch depths versus etch time for DR1/PMMA without and with N_2 respectively; it is clearly that a more stable etch rate is achieved by adding N_2. Figure 3.5 (c) shows the etch depth versus etch time for CLD1/APC.

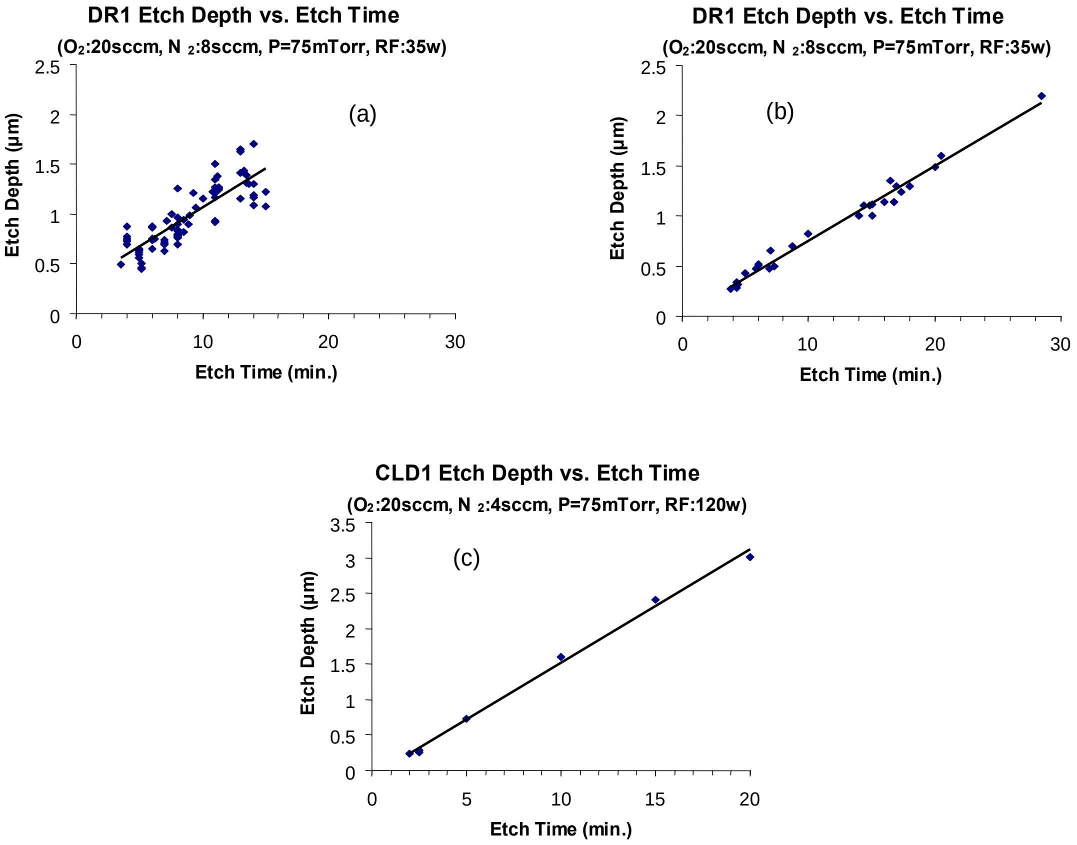

Figure 3.5. RIE etch depth versus etch time: (a) DR1/PMMA (O2: 20sccm, P: 75mTorr, RF power: 35W); (b) DR1/PMMA (O2: 20sccm, N_2: 8sccm, P: 75mTorr, RF power: 35W); (c) CLD1/APC (O2: 20sccm, N_2: 4sccm, P: 75mTorr, RF power: 120W).

3.4.6. Top claddings and top electrodes

UV11-3: The UV11-3 top cladding was directly coated onto the etched DR1/PMMA and CLD1/APC cores and then fully cured with UV lights. An 2000-5000Å Al film was deposited to serve as both the poling and modulation top electrode for low-speed modulation. For high-speed modulation, a seed layer of Cr (50 Å) and Au (2000 Å) were first deposited, and the seed-layer is then electroplated to 30000 Å using the process described in Chapter 6 in order to serve as the traveling-wave electrode. In some cases, an Al (2000-5000 Å) poling electrode was deposited prior to the seed layer deposition in order to conduct contact poling. After poling, the poling electrode was etched away, and the seed layer was deposited.

NOA61: The NOA61 top cladding was directly coated onto the etched FTC/PU layer and was fully cured using UV lights. Then Cr (200Å) and Au (2000Å) were deposited as the top electrode.

3.4.7. Dicing (cleaving) and polishing

Light could be coupled into the waveguides through the directly cleaved waveguide ends, as shown in Figure 3.6. However, the coupling loss was large in this case. Edge polishing was employed to reduce the coupling loss. Before polishing, UV15 was first dropped at the edge area and a thin (~50µm) glass slide was applied on top of the uncured UV15 layer. After being fully cured, the UV15 layer can prevent the waveguides from peeling off during the polishing process. An Ecomet 4 variable-speed polisher and diamond polishing pads from Buehler Company were employed for the polishing. The polishing speed was controlled to 30rpm and the sample edges were polished using pads with particle sizes of 25µm, 9µm, 6µm, 3µm, 1µm, and 0.5 µm sequentially.

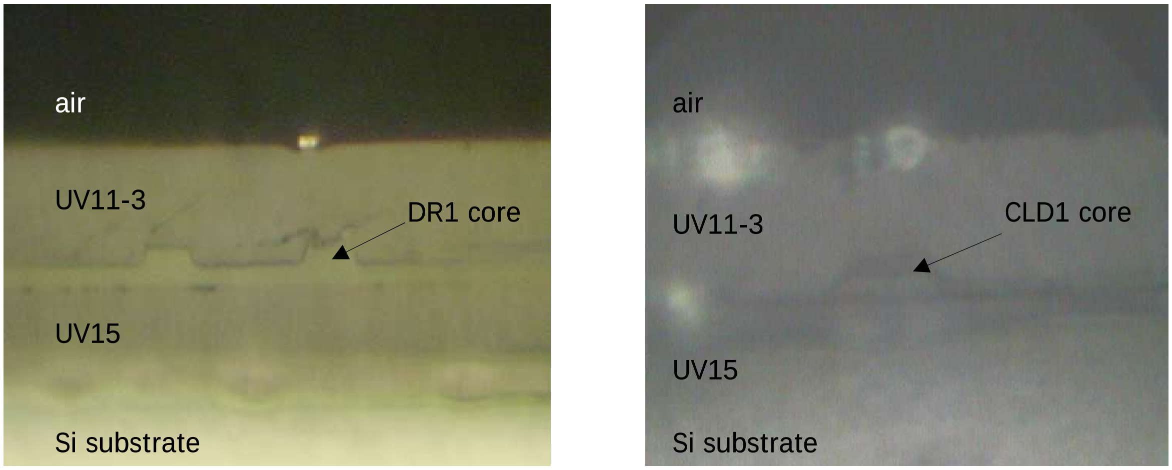

(a) (b)

Figure 3.6. Waveguide cross sections of (a) UV15:DR1/PMMA:UV11-3 and (b) UV15:CLD1/PMMA:UV11-3

3.5. WAVEGUIDE TESTING

The waveguides are tested by coupling light into and out of the samples through optical fibers. A Newport AutoAlign PCS system was employed for this purpose. This machine has the capability of automatically fine-tuning the input and output fibers in five dimensions to find the best position by monitoring the output light intensity.

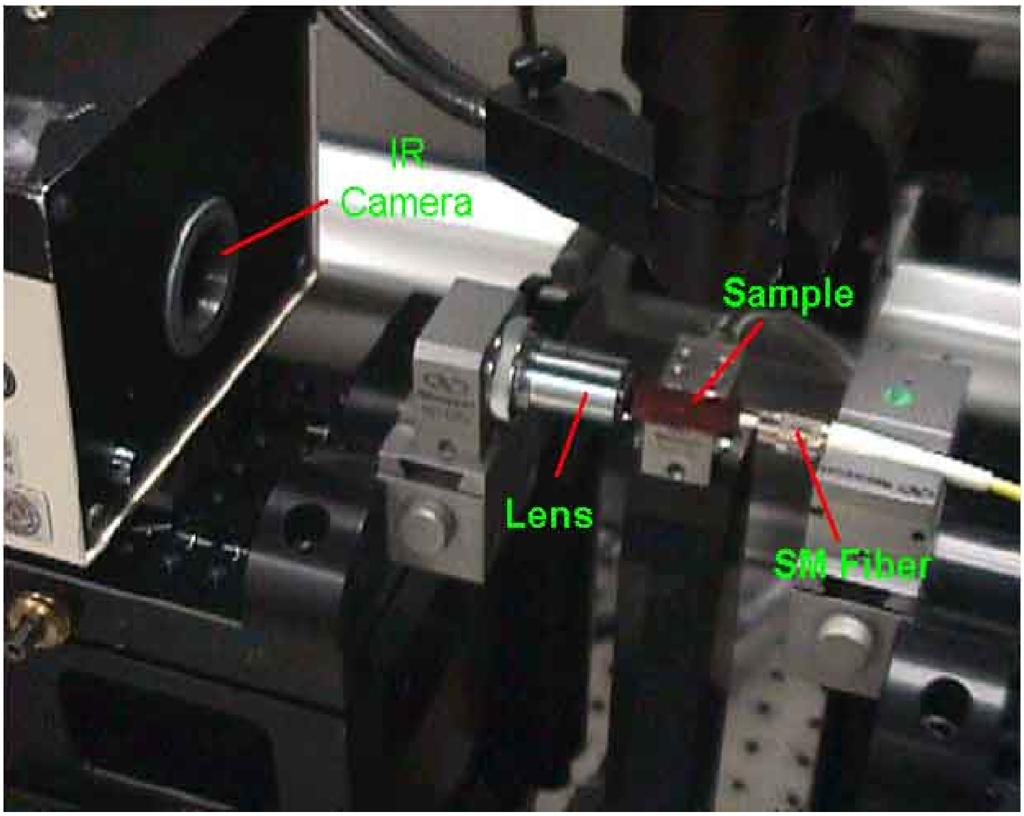

Figure 3.7. Set-up for test mode patterns

The coupling loss between the waveguide and a single-mode fiber was estimated by measuring the insertion loss change when replacing the single-mode output fiber with a multimode fiber. It was assumed that the multimode fiber can collect all the output light. The measured propagation and coupling loss of the UV15:DR1/PMMA:UV11-3 waveguide are about 3.0dB/cm and 1.5 dB/facet respectively. The measured propagation and coupling loss of the UV15:CLD1/APC:UV11-3 waveguide were around 3.5dB/cm and 3.0 dB/facet respectively.

The near-field pattern of the waveguide mode was also measured by focusing the output light into a CCD camera using an objective lens. Figure 3.7 illustrates the set-up employed for this measurement. Figures 3.8 (a), (b) show the near-field pattern of two parallel UV15:DR1/PMMA:UV11-3 waveguides and a single UV15:CLD1/APC:UV11-3 waveguide respectively. These patterns were used to verify single-mode waveguides. The experiments showed that the single-mode conditions used in the waveguide design are correct.

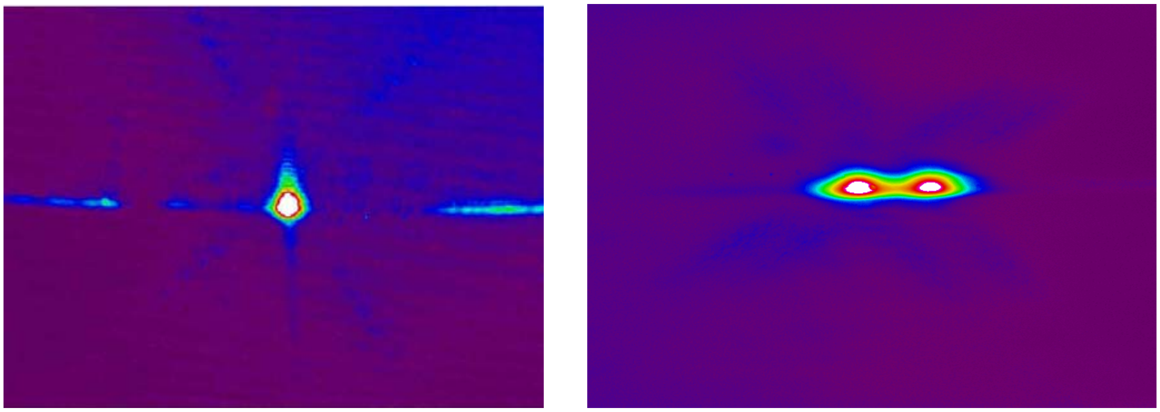

Figure 3.8. Measured field pattern of the fabricated waveguides: (a) single UV15:CLD1/APC:UV11-3 channel; (b) Dual UV15:DR1/PMMA:UV11-3 channels

3.6. SUMMARY

Single-mode buried-rib waveguides based on UV15:DR1/PMMA:UV11-3, U9120:FTC/PU:NOA61, and UV15:CLD1/APC:UV11-3, respectively, were designed, fabricated and tested. The large cross-section-design approach was employed in the waveguide design. The complete fabrication processes of these waveguides, including polymer solution preparation, polymer coating and curing, channel pattern and REI etching, edge polishing. have been discussed in detail in this chapter. The RIE-etch-rate instability problem was solved by adding N_2 to the recipe. The optimized RIE recipe is presented in this chapter. The propagation loss of the UV15:DR1/PMMA:UV11-3 and UV15:CLD1/APC:UV11-3 waveguides was measured to be 3.0dB/cm and 3.5 dB/cm respectively.

Chapter 4 Polymer-Based Intrinsic 3dB-Biased EO Modulators

4.1. INTRODUCTION

To date, the structures of most reported EO modulators, no matter fabricated with inorganic crystals or EO polymers, are exclusively based on the Mach-Zehnder interferometer or its variables. [43-52] In a Mach-Zehnder modulator, the intrinsic sinusoidal modulation curve prohibits it from improving modulation linearity, and the direct-current (*dc*) bias, required in order to set the modulator at the half-power point, results in more complicated circuit fabrication. These problems may be overcome by using modulators based on properly designed directional-coupler structures. The directional coupler-based modulators have many more varieties since various modulation curves and intrinsic points (the positions in their modulation curves when no *dc* voltages are applied) can be achieved by changing the interaction length-to-conversion length ratios, by employing domain-inversion (or $\Delta\beta$-inversion) techniques, or by using different feeding methods. Therefore, it is worthwhile to investigate this type of modulator which incorporates the benefits of EO polymer materials.

Thaniyavarn first reported a Y-fed directional coupler modulator using an inorganic crystal material (Ti:LiNbO$_3$)[53]. The linearity, inter-modulation distortion, and other unique characteristics of such modulators were theoretically investigated at that point.[11] In this chapter, we will present two Y-fed directional waveguide coupler modulators which are fabricated with EO polymers. These modulators eliminate the necessity of a *dc* bias since they are intrinsically biased at the 3-dB points due to their symmetric structure.

4.2. THEORY OF Y-FED DIRECTIONAL COUPLER MODULATORS

Basically, a Y-fed directional coupler modulator (YCM) consists of a single-mode Y-junction splitter and a co-directional coupler with two parallel and symmetric waveguide channels. The schematic diagram and the fabrication parameters of the modulator are shown in Figure 4.1. A light beam is fed in and split into the two symmetric waveguides equally through the Y-junction region. The co-directional coupler guides the two light beams in traveling along the two channels. However, the separation between the two parallel waveguides is not as wide as that of a Mach-Zehnder modulator. There is a coupling between the two channels. With no modulating voltage applied, the modulator is set to the 3-dB operating point automatically due to the symmetric structure of the Y-fed directional coupler. While a driving voltage is applied through the electrodes over the coupler region, however, the light can be coupled from one channel into the other. Note that the Y-fed coupler modulator has two complementary optical outputs. For a normalized input and omitting the waveguide loss, we have $P_2=1-P_1$, apparently due to the conservation of the total power.

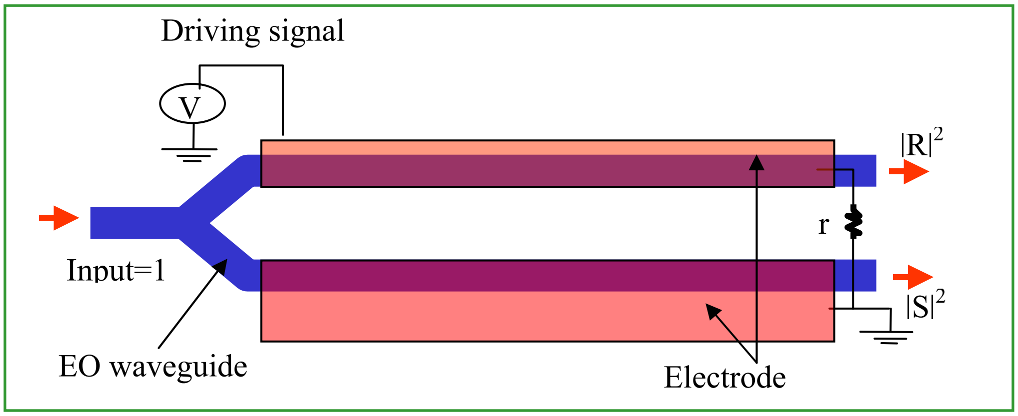

Figure 4.1. Schematic diagram of a Y-fed directional coupler modulator

To simplify the description, the "cross" state ⊗ is named as the light crosses over completely from one guide to the other, and the "bar" state ⊖ as the light beam passes straight through and appears at the output of the same guide. The application of a voltage to the uniform electrode induces a phase mismatch $\Delta\beta = \beta_1 - \beta_2$ between the propagation constants of the two wave channels. We describe the light in the two guides by complex amplitudes R(z) and S(z), which vary slowly along the z axis, i.e., the propagation direction. We assume that the energy exchange between the two guides is governed by the coupled-wave equations[54-56]

$$\frac{\partial R}{\partial z} - j\,\delta\,R = -j\mathrm{k}\mathrm{S} \qquad \textbf{(Equation 4.1)}$$

and

$$\frac{\partial S}{\partial z} + j\,\delta\,S = -j\mathrm{k}R \ , \qquad \textbf{(Equation 4.2)}$$

where $\delta = \Delta\beta/2$, and $\kappa = \pi / 2\ell$ is the coupling coefficient determined by the channel separation and the refractive indices of the polymers. $\Delta\beta$ is a function of the driving voltage applied to the electrode over the optical waveguides:

$$\Delta\beta \propto n, \gamma, V, {}^{1}\!/_{d} \qquad ,$$

where γ is the electro-optic coefficient, V is the applied voltage, and d is the separation between the two electrodes.

For a normalized input, the amplitudes $R_o = S_o = 1/\sqrt{2}$ in the Y-branch structure, the solution of the coupled-wave equations can be written in the matrix form

$$\begin{bmatrix} R \\ S \end{bmatrix} = \begin{bmatrix} A & -jB \\ -jB^* & A^* \end{bmatrix} \begin{bmatrix} \frac{1}{\sqrt{2}} \\ \frac{1}{\sqrt{2}} \end{bmatrix} \qquad \textbf{(Equation 4.3)}$$

where

$$\begin{cases} A = \cos L\sqrt{\kappa^2+\delta^2} + j\dfrac{\delta}{\sqrt{\kappa^2+\delta^2}}\sin L\sqrt{\kappa^2+\delta^2} \\ B = \dfrac{\kappa}{\sqrt{\kappa^2+\delta^2}}\sin L\sqrt{\kappa^2+\delta^2} \end{cases} \qquad \textbf{(Equation 4.4)}$$

The device is in the cross state when $A - jB = 0$, *i.e.*,

$$\cos L\sqrt{\kappa^2+\delta^2} + j\frac{\delta-\kappa}{\sqrt{\kappa^2+\delta^2}}\sin L\sqrt{\kappa^2+\delta^2} = 0 \quad ,$$

implying that

$$\left(\frac{L}{l}\right)^2 + \left(\frac{\Delta\beta L}{\pi}\right)^2 = (2n+1)^2 \qquad (n = 0, 1, \ldots) \qquad \textbf{(Equation 4.5)}$$

and

$$\frac{L}{l} = \frac{\Delta\beta L}{\pi} \quad , \qquad \textbf{(Equation 4.6)}$$

where $l = \pi/2\kappa$ is the conversion length, which is the minimum length required to obtain a complete crossover in a directional coupler. These conditions lead to some isolated points marked ⊗ in the switching diagram shown in Figure 4.2.

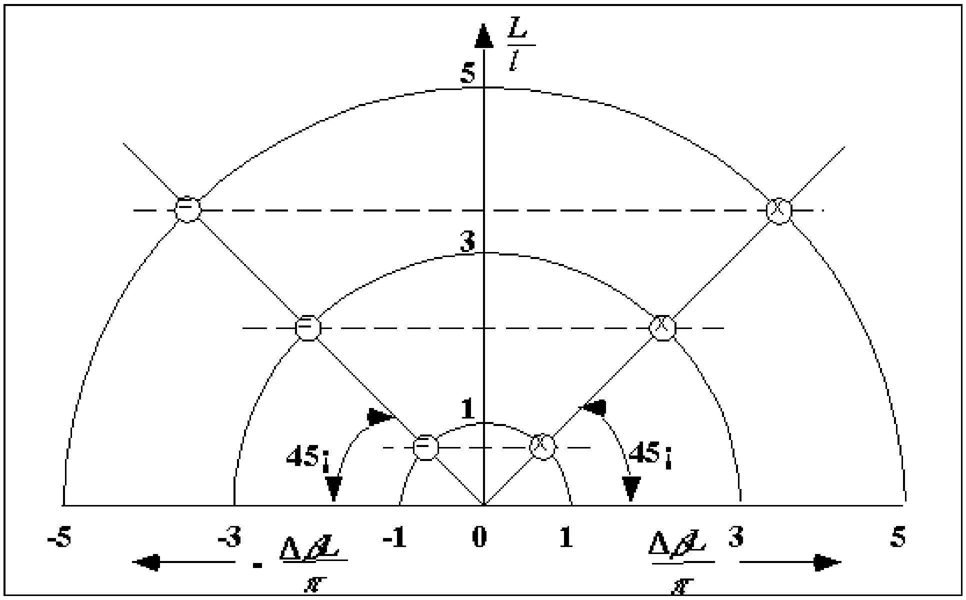

Figure 4.2. Switching diagram of a conventional Y-fed directional coupler modulator

The modulator is in the bar state when $A^* - jB^* = 0$, i.e.,

$$\cos L\sqrt{\kappa^2+\delta^2} - j\frac{\delta+\kappa}{\sqrt{\kappa^2+\delta^2}}\sin L\sqrt{\kappa^2+\delta^2} = 0,$$

which is equivalent to

$$\left(\frac{L}{l}\right)^2 + \left(\frac{\Delta\beta L}{\pi}\right)^2 = (2n+1)^2 \qquad \textbf{(Equation 4.7)}$$

and

$$\frac{L}{l} = -\frac{\Delta\beta L}{\pi} \quad . \qquad \textbf{(Equation 4.8)}$$

These conditions lead to some isolated points marked ⊖ in the switching diagram in Figure 4.2.

The conditions for the cross and bar states can be graphically represented by a switching diagram as shown in Figure 4.2, where we use the values of L/l and $\Delta\beta L/\pi$ as coordinates. The cross states are represented by isolated points on the 45° line through the origin, and the bar states are represented by isolated points on the 135° line through the origin. While in this device configuration the L/l value is essentially independent of the applied voltage, the $\Delta\beta$ value can be controlled electrically. An increase in the voltage moves from left to right the point representing the state of the coupler parallel to the $\Delta\beta L/\pi$ axis. After checking all the available solutions with L/l up to 15, we have found that only the first point, $L/l=\sqrt{2}/2$, provides an acceptable linear transfer curve, which is similar to that of a conventional directional coupler and a Mach-Zehnder interferometer.

Usually a Y-fed directional coupler modulator is characterized by its interaction length (L), its conversion length (l), and the propagation constant mismatch ($\Delta\beta$) between the two channels. For a push-pull structure, the mismatch $\Delta\beta$ caused by the driving voltage is determined by

$$\Delta\beta = \frac{2\pi}{\lambda} n_e^3 r_{33} \alpha \frac{V}{d} \quad , \qquad \textbf{(Equation 4.9)}$$

where λ is the optical wavelength, n_e is the extraordinary index of EO film, d is the electrode spacing, and α is the overlap integral between the applied electrical field and the optical field ($0 < \alpha < 1$). Using the coupled-mode theory [55], an expression of the light power outputting of the modulator can be obtained. In a normalized condition, the light power P_1 of the upper branch is given by

$$P_1 = |R|^2 = \frac{1}{2}\left[1 - \frac{2xs}{r^2}\sin^2(\frac{\pi r}{2})\right] \quad ,$$ **(Equation 4.10)**

where the normalized driving voltage is

$$x = \Delta\beta L/\pi = \frac{2n_e^3 r_{33}\alpha L}{\lambda d}V = \Gamma V$$ **(Equation 4.11)**

and

$$\Gamma = \frac{2\, n_e^3 r_{33}\,\alpha\, L}{\lambda d} \quad .$$ **(Equation 4.12)**

The normalized interaction length is

$$s = L/l \quad ,$$ **(Equation 4.13)**

and

$$r^2 = x^2 + s^2 \quad .$$ **(Equation 4.14)**

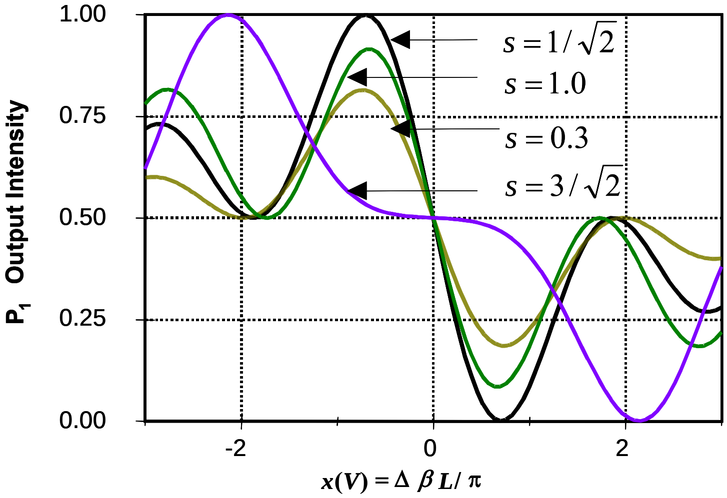

Figure 4.3. Transfer curves of a conventional Y-fed directional coupler modulator with various normalized interaction lengths (*s*=*L*/*l*)

Supposing power conservation, the power in the lower branch is $P_2 = 1- P_1$. It is clear that x is a linear function of the driving voltage, although the normalized interaction length s is independent of it. According to Equations (4.3) and (4.4), the Y-fed directional coupler modulator is set at the 3dB operation point automatically, i.e., $P_1=P_2= 1/2$ when no driving voltage is applied. Figure 5.3 shows the simulated results of the light intensity versus the driving voltage when s = 0.3, $1/\sqrt{2}$, 1.0, and $3/\sqrt{2}$, respectively. Notice that the maximum modulation depths are different with different values of the normalized interaction length. A 100% depth is reached when $s=1/\sqrt{2}$ and $3/\sqrt{2}$. Theoretically, the 100% modulation depth is possible only when $s = L/l = (2n+1)/\sqrt{2}$ (n= 0, 1, 2…), according to Equation (4.10).

4.3. DEVICE DESIGN

The UV15:DR1/PMMA:UV11-3 and U9120:FTC/PU:NOA61 waveguides described in Chapter 3 were used to build Y-fed directional couplers which operate at 1.55μm and 1.31μm respectively. As shown in Figure 4.4, a Y-fed directional coupler consists of three sections: (1) a single-mode input at the left; (2) a Y-branch junction in the middle, and (3) a 2x2 directional coupler on the right. All the three parts are basically formed by single-mode waveguides. The structure of the Y-branch junction and the separation between the two waveguides in the 2x2 directional coupler should be carefully optimized in order to obtain well-performed modulators. The design of the single-mode waveguides has been presented in Section 3.3. We will describe only the designs of the Y-branch junctions and the 2x2 directional couplers here. All the simulations were carried out with a waveguide design tool BeamPROP$^{\text{TM}}$ (v4.0, Rsoft, Inc.).

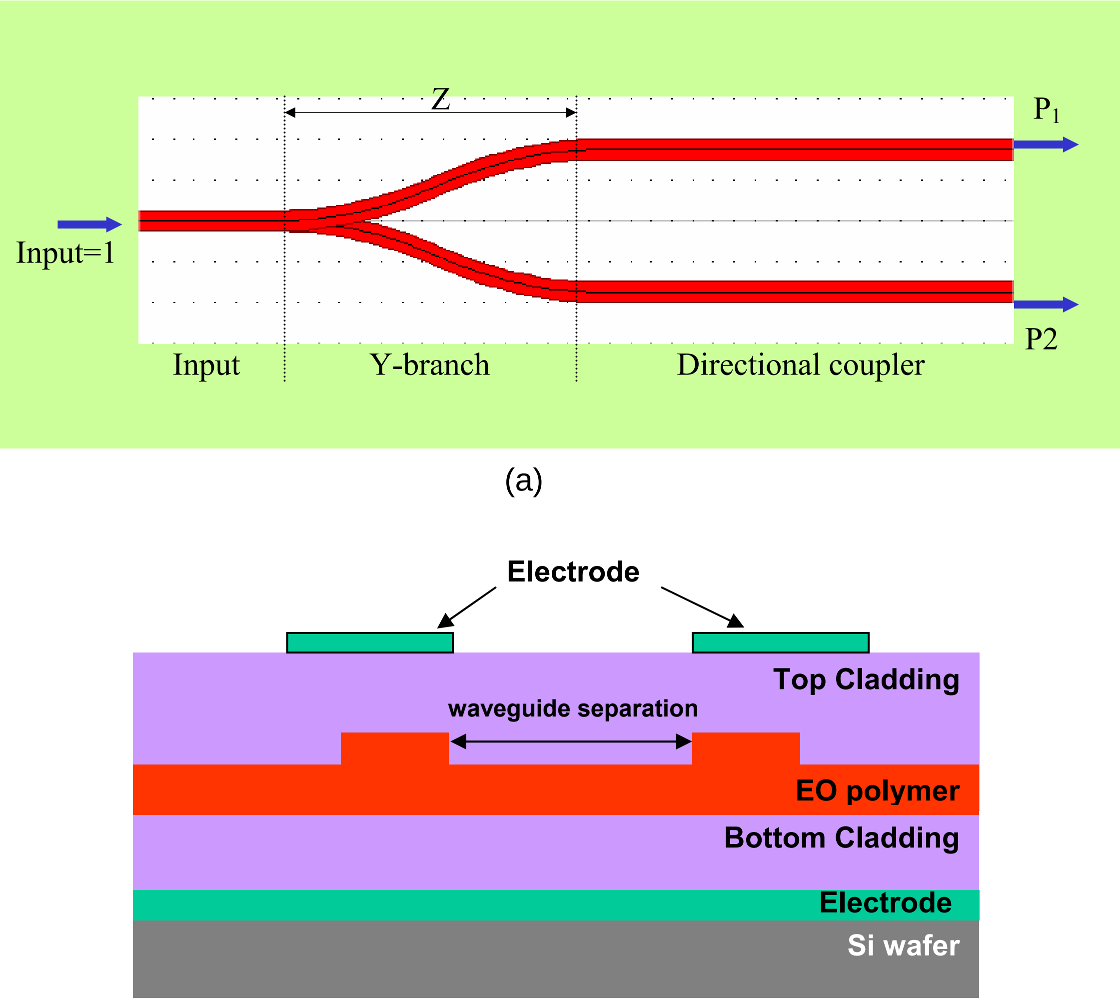

(a)

(b)

Figure 4.4. The waveguide structure of a Y-fed directional coupler: (a) Top view; (b) Waveguide cross section at the output end.

4.3.1. Design of Y-branches

For a Y-branch junction, the separation angle is typically less than 2 degrees. Otherwise, the radiation propagation loss within the junction area would be massive. The mode-conversion of a Y-junction has been analyzed by Burns.[58] When the taper slope is large, considerable mode conversion occurs, and the structure acts as a power divider. Otherwise, when the taper angle is small, mode conversion is negligible, and the structure acts as a mode splitter. In our simulation, we used two symmetric S-bends for the branch and set the separation of the two output channels to the desired value. Figure 4.5 shows the output power versus the length of the junction in the horizontal direction (i.e., Z in Figure 4.4(a)) for a U9120:FTC/PU:NOA61 Y-branch with the dimensions given in the figure. Notice that the radiation loss in the junction is significant when the Y-junction length is shorter than 800μm. In the real design, the Y-junction lengths for the two kinds of modulators were both set to be 1000μm.

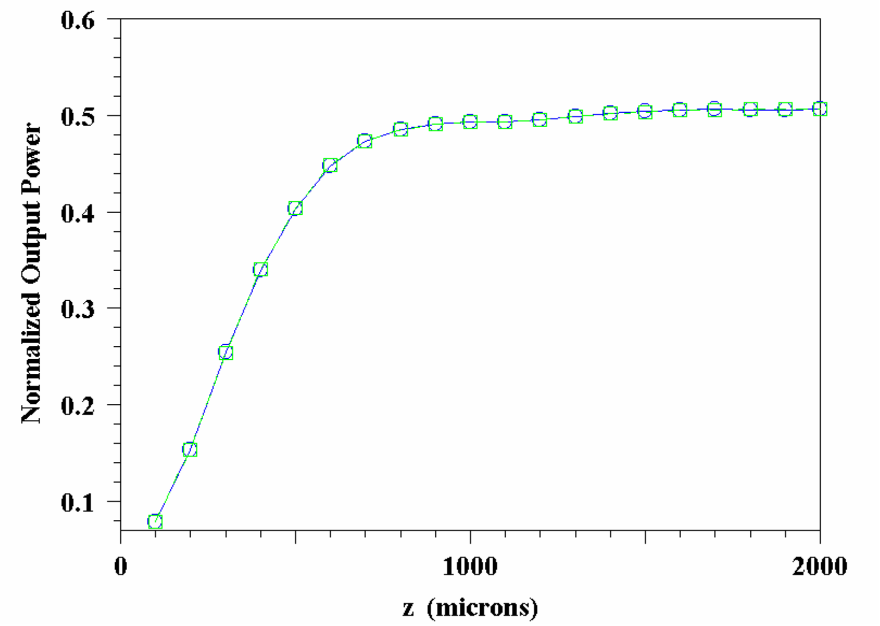

Figure 4.5. Simulation result: normalized output of each channel versus the junction length of an U9120:FTC/PU:NOA61 Y-branch junction. The separation of two channels at output is set at 8μm, the waveguide width=6μm, and the rib depth = 0.3 μm.

4.3.2. Design of 2x2 directional couplers

For a 2x2 directional coupler, the conversion length is the most important parameter since it defines the conversion length-to-interaction length ratio when the interaction length is fixed. The conversion length is determined by the waveguide dimensions and the separation between the two waveguides. Figure 4.6 shows the simulation result of a UV15:DR1/PMMA:UV11-3-based 2x2 directional coupler with a 13-μm waveguide separation and 1.44μm rib depth. Figure 4.6 (a) shows the top view of the 2x2 directional coupler when a light beam is coupled into the left channel first. When the light travels along the Z (vertical in (a)) direction, the light power in either channel changes due to the coupling between the two channels. In Figure 4.6 (b), the blue and green curves represent the light powers in the left channel and right channel respectively, and the vertical axis is the propagation distance. In the design process, we first determined the interaction length based on the device performance requirements and the material properties, then the simulation results were used as a guide to choose a waveguide separation value. Finally, the desired normalized interaction length was achieved by adjusting the rib depths to fine-tune the conversion length. The interaction length and the waveguide separation were 2.0cm and 13 μm respectively, for UV15:DR1/PMMA:UV11-3-based modulators. The corresponding values for U9120:FTC/PU:NOA61-based modulators were 2.0 cm and 8 μm respectively.

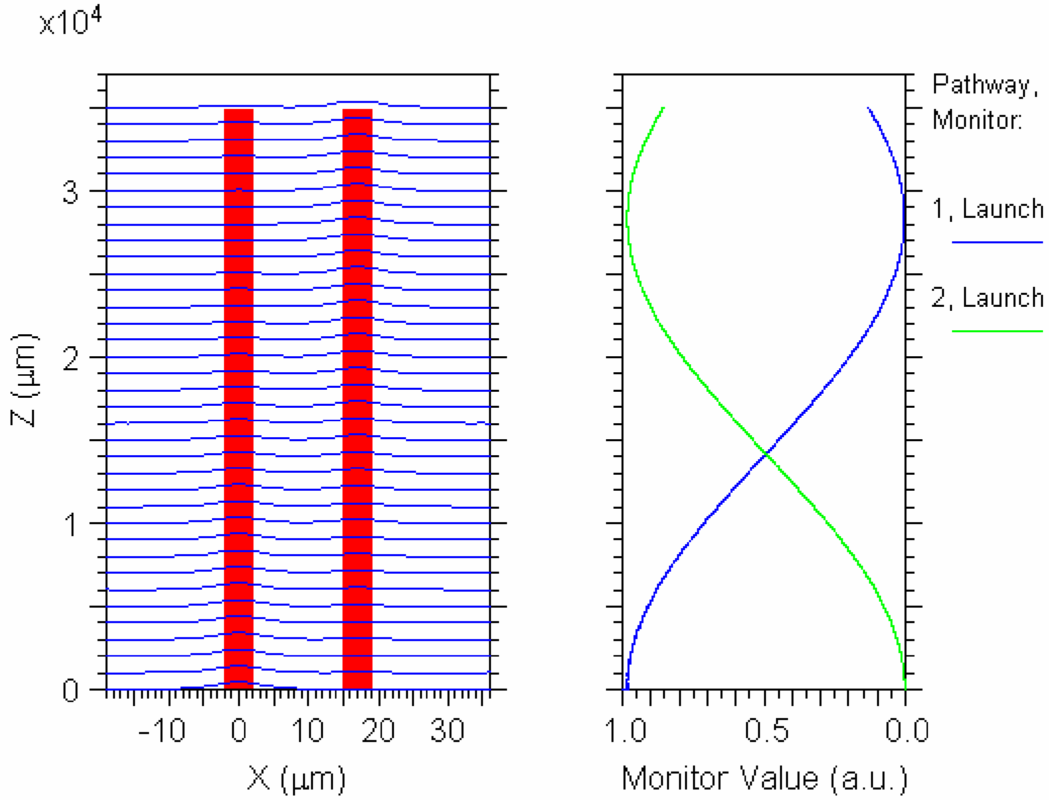

(a) (b)

Figure 4.6. The conversion length of a 2x2 directional coupler: (a) a diagram of the directional coupler (the light is coupled into the left channel at the beginning); (b) the light power intensities in the left channel (blue curve) and in the right channel (green curve)

4.4. DEVICE FABRICATION

The devices were fabricated employing the fabrication procedures described in Section 3.4. The rib depths were controlled to be around 1.44μm and 0.3μm for the UV15:DR1/PMMA:UV11-3 and U9120:FTC/PU:NOA61 waveguides respectively, in order to obtain the desired normalized interaction length of 0.707.

4.5. DEVICE TESTING AND EXPERIMENTAL RESULTS

4.5.1. The UV15:DR1/PMMA:UV11-3-based modulator

The UV15:DR1/PMMA:UV11-3-based modulator was tested using a Santec ECL-200 laser at a wavelength of 1.55μm. A polarization-maintained (PM) single-mode (SM) fiber was used to couple light, polarized in the TM direction, into the device, and the light was coupled out using a fiber. The driving voltage was applied to the two arms in push-pull fashion. Figure 4.7 shows the modulation voltage and modulated signal. In Figure 4.7, the sinusoidal curve is the modulation signal (electrical); the other curve with more curvatures is the modulated signal (optical); the horizontal axis is the time axis (200 μsec per division); and the vertical direction shows the voltage for the modulation signal (10 Volts per division) and the optical intensity for the modulated signal. The total insertion loss was around 14dB, and an extinction ratio of 20 dB was achieved.

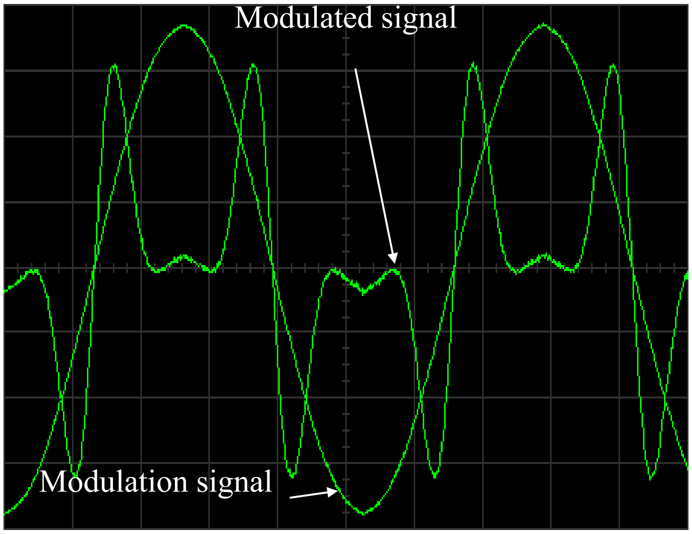

Figure 4.7. Modulation and modulated signals of the UV15:DR1/PMMA:UV11-3-based Y-fed directional coupler

4.5.2. The U9120:FTC/PU:NOA61-based modulator

The U9120:FTC/PU:NOA61-based modulator was tested using a diode-pumped Nd:YVO_4 laser at the wavelength of 1.34μm. The laser beam, polarized in the TM direction, was coupled into the device and collected by two 60X objectives respectively. The output light was measured with a photo-detector. The mode profile was recorded with an IR camera (Electrophysics Model 7290). Two equal but opposite voltage signals were applied to the top electrodes. The bottom electrode was grounded. Figure 4.7 shows the schematic diagram of the setup. Figure 4.8 shows the mode patterns and the intensity profiles of the modulator's two light beams, measured under different driving voltages. When no voltage was applied, the two intensity profiles of the two branches were almost identical, as shown in Figure 4.8(a), corresponding to an equal intensity splitting within 0.4% accuracy. Therefore, the modulator was intrinsically set at the 3-dB half-power point. While the driving voltage was increased to 1.8V, the light in the upper branch of the modulator was coupled into the lower branch, where the light pattern of the upper branch disappeared, and the intensity profile of the lower branch reached its maximum (Figure 4.8(b)). It was confirmed that the switching voltage applied to modulate the light of either branch from a bar-state (maximum intensity) to a cross-state (minimum intensity) was 3.6V, corresponding to a light extinction ratio of 26dB. The AC modulation responses of the two branches versus the driving voltage are further presented in Figure 4.9. The triangle curves in the figures were the driving voltage signals at the frequency of 50 kHz. Notice that the light intensities emanating from the two branches were complementary, i.e., $P_2 = 1 - P_1$. With a laser input of 35mW (~3×10^5 W/cm^2), the modulator operated for more than 500 hours, within which time the same experimental result was routinely observed without any drifting.

4.6. SUMMARY

We have demonstrated polymeric electro-optic modulators based on Y-fed directional couplers employing UV15:DR1/PMMA:UV11-3 and U9120:FTC/PU:NOA61 waveguides, respectively. The symmetric geometry of these couplers provided the modulators with the unique characteristics of an intrinsic 3-dB operating point and two complementary output ends. A low switching voltage of 3.6V and a high extinction ratio of 26dB were obtained with the U9120:FTC/PU:NOA61-based modulator, operating at a wavelength of 1.34μm. A theoretical analysis of the Y-fed directional coupler was presented. The design of the Y-branch junctions and the 2×2 directional couplers, which are components of the Y-fed directional couplers, was described as well.

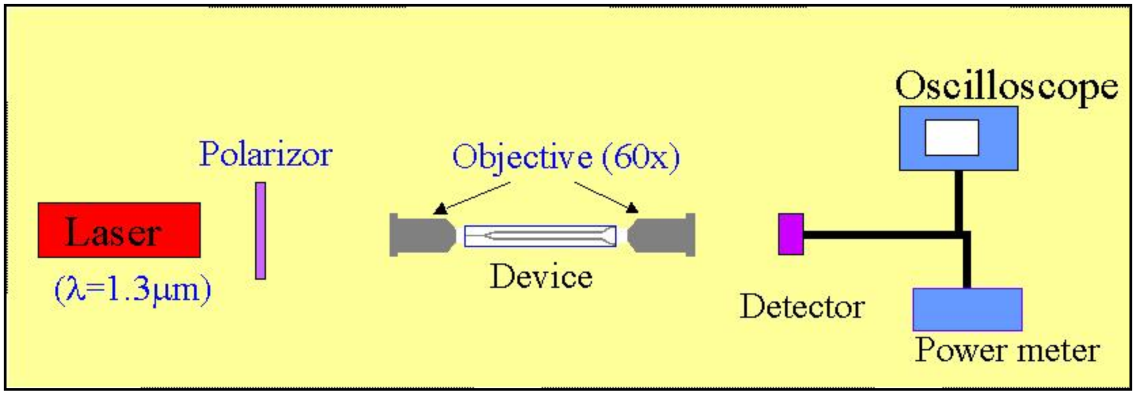

(a)

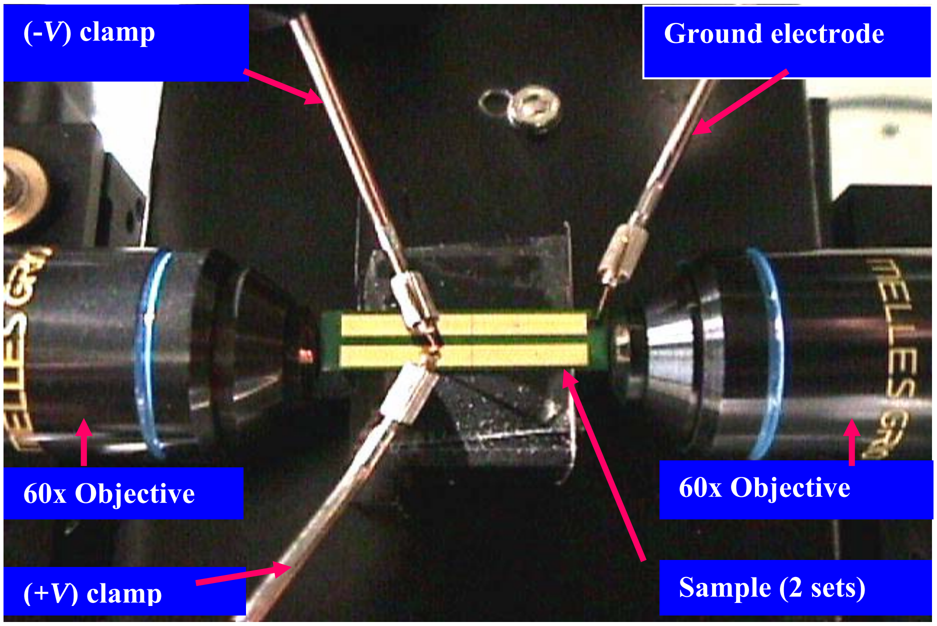

(b)

Figure 4.8. Setup for modulation testing: (a) schematic diagram; (b) modulator arrays under testing

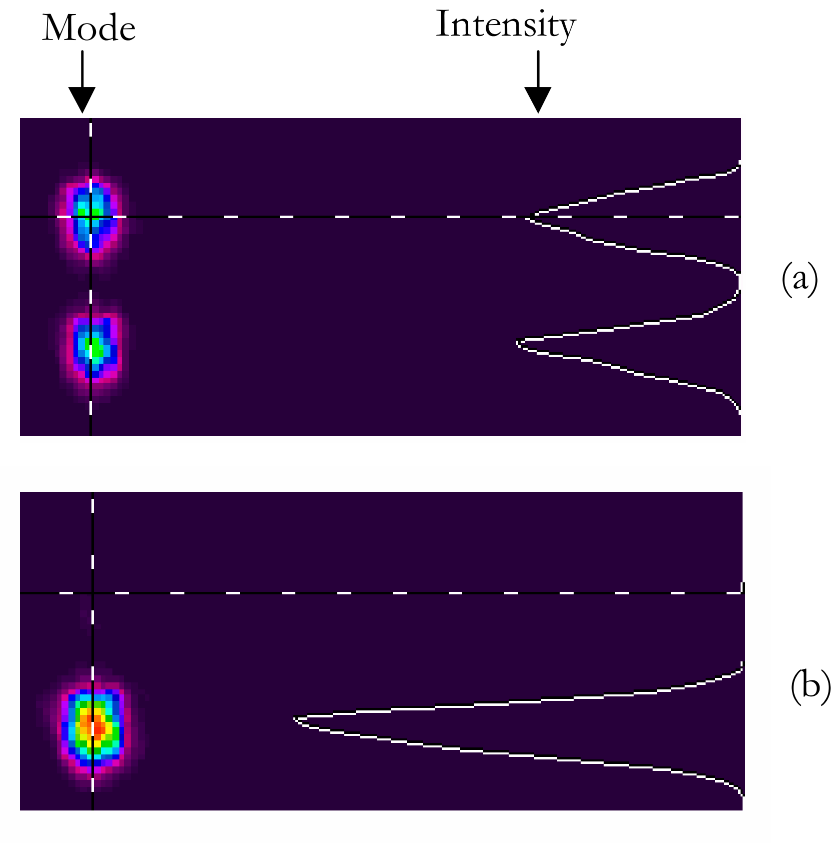

Figure 4.9. Mode profiles under (a) no voltage applied, (b) 1.8 V driving voltage, where the light originally in the upper channel was coupled into the lower channel.

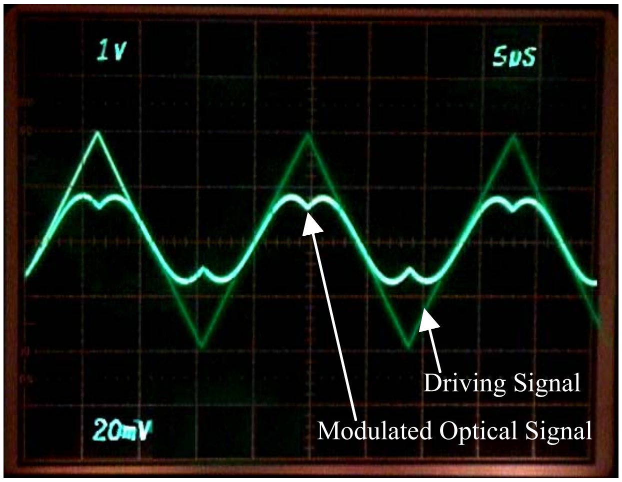

(a)

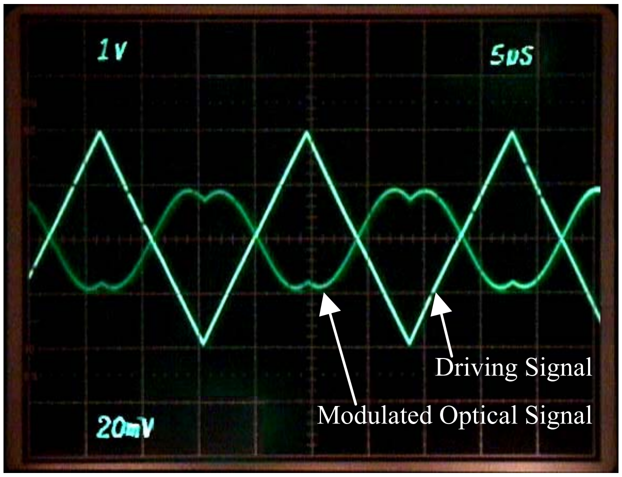

(b)

Figure 4.10. Modulation curves of the modulator: (a) upper branch and (b) lower branch

Chapter 5 A High-Linear Waveguide Modulator Based on a Δβ-Inverted EO Polymer

5.1. INTRODUCTION

Although several commercial integrated optical modulators are currently available, their performance is still adversely affected by the distortions caused by the nonlinearity of their modulation curves. These curves typically exhibit sine-squared behaviors. On the other hand, high-performance analog optical systems like CATV trunk links do require high suppression of the nonlinear distortions. In view of the rapidly increasing demand for linear external modulators, practical, viable schemes for linearizing the modulator performance are receiving considerable attention. A substantial R&D work has already been performed over the past several years, resulting in a number of linearization techniques. These can be subdivided into two categories, namely, electronic compensations and optical methods of linearization. A common shortcoming in these techniques is that the improvement in linearity comes at the expense of simplicity in device design and of simplicity of the driving circuits.

In this chapter, we first present the feasibility of building high-linear modulators that are based on two-section Y-fed directional couplers (Section 5.2). Then a Y-fed directional coupler based on domain-inverted EO polymer was designed, fabricated, and tested (Section 5.3). This coupler has a high-linear modulation curve, as well as a simple device structure.

In this chapter, we will present the investigation of a linear modulator based on a Δβ-inverted Y-coupler structure. Employing the two-section contact poling technique as described in Section 4.4, the two sections can be poled in opposite directions, resulting in the domain inversion of the polymer waveguide. By properly designing the interaction length of a Y-coupler, we found that the nonlinear response in the left half section can be canceled by that in the right half. Thus the intermodulation distortion is suppressed, and its linearity is improved.[54]

5.2. THE THEORY OF A Y-FED DIRECTIONAL COUPLER WITH Δβ-INVERTED SECTIONS

A schematic diagram of the proposed modulator based on a two-section directional coupler is shown in Figure 5.1, in which the sign of the first section's Δβ is opposite to that of the second section's. The sign opposition can be implemented by either applying opposite voltages to the two sections or by poling the two sections in opposite directions, employing the domain-inversion poling method described in Section 2.3. The interaction length L is divided into two sections with lengths L1 and L2 respectively.

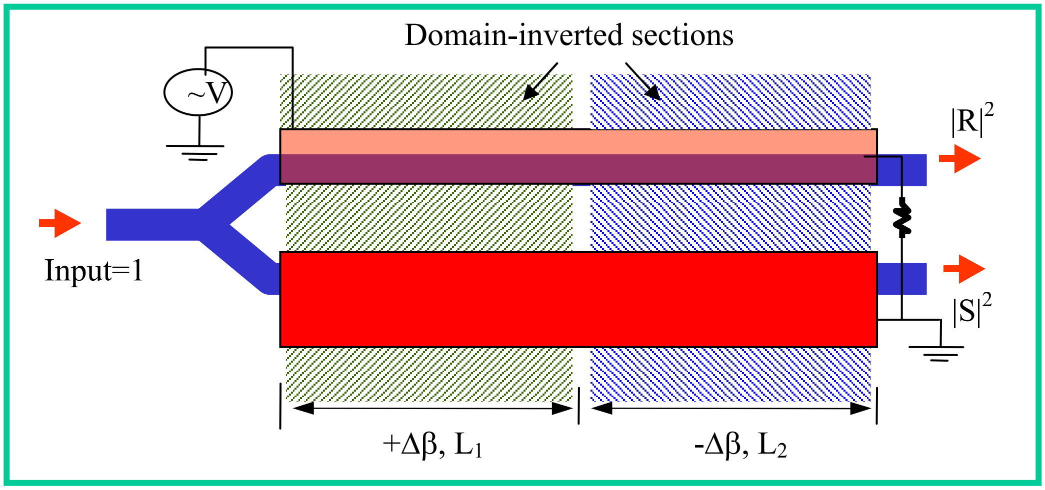

Figure 5.1. A Δβ-inverted Y-fed waveguide directional coupler

Based on the results presented in Chapter 4, the matrix expression relating the optical fields in the input and output channels is easily derived as follows:

$$\begin{bmatrix} R_o \\ S_o \end{bmatrix} = M_2 M_1 = \begin{bmatrix} A_2 & -jB_2 \\ -jB_2^{*} & A_2^{*} \end{bmatrix} \begin{bmatrix} A_1 & -jB_1 \\ -jB_1^{*} & A_1^{*} \end{bmatrix} \begin{bmatrix} R_i \\ S_i \end{bmatrix} \quad , \qquad \textbf{(Equation 5.1)}$$

where $R_i\,(S_i)$ and $R_o\,(S_o)$ are the optical fields in the input and output channels respectively; Matrix M_1 corresponds to the first section, and M_1's coefficients are given by the expressions

$$\begin{cases} A_1 = \cos\dfrac{\pi}{2}\sqrt{s_1^2 + \left(\dfrac{s_1 x}{s_1 + s_2}\right)^2} + j\dfrac{x}{\sqrt{(s_1+s_2)^2 + x^2}}\sin\dfrac{\pi}{2}\sqrt{s_1^2 + \left(\dfrac{s_1 x}{s_1 + s_2}\right)^2} \\ B_1 = \dfrac{(s_1+s_2)}{\sqrt{(s_1+s_2)^2 + x^2}}\sin\sqrt{s_1^2 + \left(\dfrac{s_1 x}{s_1 + s_2}\right)^2} \end{cases}$$

(Equation 5.2)

Matrix M_2 corresponds to the second section, and its coefficients can be calculated by

$$\begin{cases} A_2 = \cos\dfrac{\pi}{2}\sqrt{s_2^2 + \left(\dfrac{s_2 x}{s_1 + s_2}\right)^2} - j\dfrac{x}{\sqrt{(s_1+s_2)^2 + x^2}}\sin\dfrac{\pi}{2}\sqrt{s_2^2 + \left(\dfrac{s_2 x}{s_1 + s_2}\right)^2} \\ B_1 = \dfrac{(s_1+s_2)}{\sqrt{(s_1+s_2)^2 + x^2}}\sin\sqrt{s_2^2 + \left(\dfrac{s_2 x}{s_1 + s_2}\right)^2} \end{cases}$$

(Equation 5.3)

In the above equations, $s_1 = L_1 / l$ is the normalized interaction length of the first section; $s_2 = L_2 / l$ is the normalized interaction length of the second section; $x = \Delta\beta(L_1 + L_2)/\pi$ is the normalized driving voltage; $\Delta\beta = \beta_1 - \beta_2$ is the voltage-induced propagation-constant mismatch in the two channels; and l is the coupling length. In our case, i.e., for a symmetric input Y-junction, we have $R_i = S_i = 1/\sqrt{2}$.

5.3. IMPROVEMENT OF NONLINEAR DISTORTION SUPPRESSION

It is well known that there exist several possible definitions for the linearity of device performance, each being most appropriate for a specific practical application. One of the most important criterions is the level of the nonlinear distortions caused by the transfer curves, nonlinearity. The low distortion criterion is normally used when assessing the performance of devices to be deployed in analog optical systems such as fiber-optic CATV links and sensors.

When several sinusoidal modulating signals are applied to an electrooptic modulator, the RF spectrum at the output is known to contain, in general, both the frequencies of the input signals (fundamental output) as well as other frequencies represented by a set of combinatorial products (nonlinear distortions). It is customary to distinguish between harmonic and intermodulation nonlinear distortions (IMD). The presence of nonlinear terms with frequencies within the detection bandwidth can severely degrade the dynamic range. It is well known that even-order distortions can be effectively suppressed by biasing the modulator to the inflection point of the modulation curve. As pointed out above, the Y-fed coupler is automatically biased to this 3-dB point due to its symmetrical structure. In this case, the dynamic range is determined by the third-order nonlinear products that include, in general, both harmonic and intermodulation spectral components. The harmonics can be filtered out by using a sufficiently narrow photodetection bandwidth (suboctave reception). IMDs, on the other hand, can fall insider the detection bandwidth.

In order to investigate the linearity property of the Y-fed directional couplers in terms of nonlinear distortion suppressions, the distortion suppression (DS), defined as the ratio of the largest distortion to the fundamental output at a specific level of optical modulation depth (namely, 1%), was calculated for couplers with various parameters. Based on Equations 5.1, 5.2, and 5.3, the transfer curves of the Y-fed directional couplers are completely determined by the two normalized interaction lengths, s_1 and s_2. The investigation is consisted of simply calculating the DS as a function of s_1 and s_2. We employed a two-tone numerical procedure to calculate the level of the distortions by applying Fourier analysis to the time-dependent optical outputs coming from a Y-fed modulator with two electric signals of slightly different frequencies (f_1 and f_2) applied to the electrodes. Our goal is to determine the optimum device parameters that minimize the DS. Advantageously, the DS criterion is of a general nature, being independent of the noise level in any particular analog optical system.

Figure 5.2 shows the DS being calculated, at an optical modulation depth of 1%, as a function of the normalized section lengths (ratios s_1 and s_2) for two-section Y-fed directional couplers. Note that one-section Y-fed directional couplers were also included in our calculation in the cases of $s_1 = 0$ or $s_2 = 0$. The results indicate that high DSs in excess of 130 dB can be attained by carefully choosing the values of s_1 and s_2. Some points on the s_1 - s_2 plane, which have excellent distortion suppression capability, are picked up and marked in Figure 5.2. The properties of modulators with s_1 and s_2 values at these chosen points are evaluated and summarized in Table 5.1, which quantifies their DSs, driving voltages, and modulation depths. The corresponding values of a normal Y-fed directional coupler (NYCM ($s_1 = 1/\sqrt{2}$, $s_2 = 0$)) and a quadrature-biased Mach-Zednder modulator (MZM) are also given on Table 5.1 by comparison. Here, the driving voltages are calculated based on the slopes of their transfer curves at their direct-current biased points (the bias voltages for Y-fed directional couplers are 0), and are normalized to the value of the normal Y-fed directional coupler.

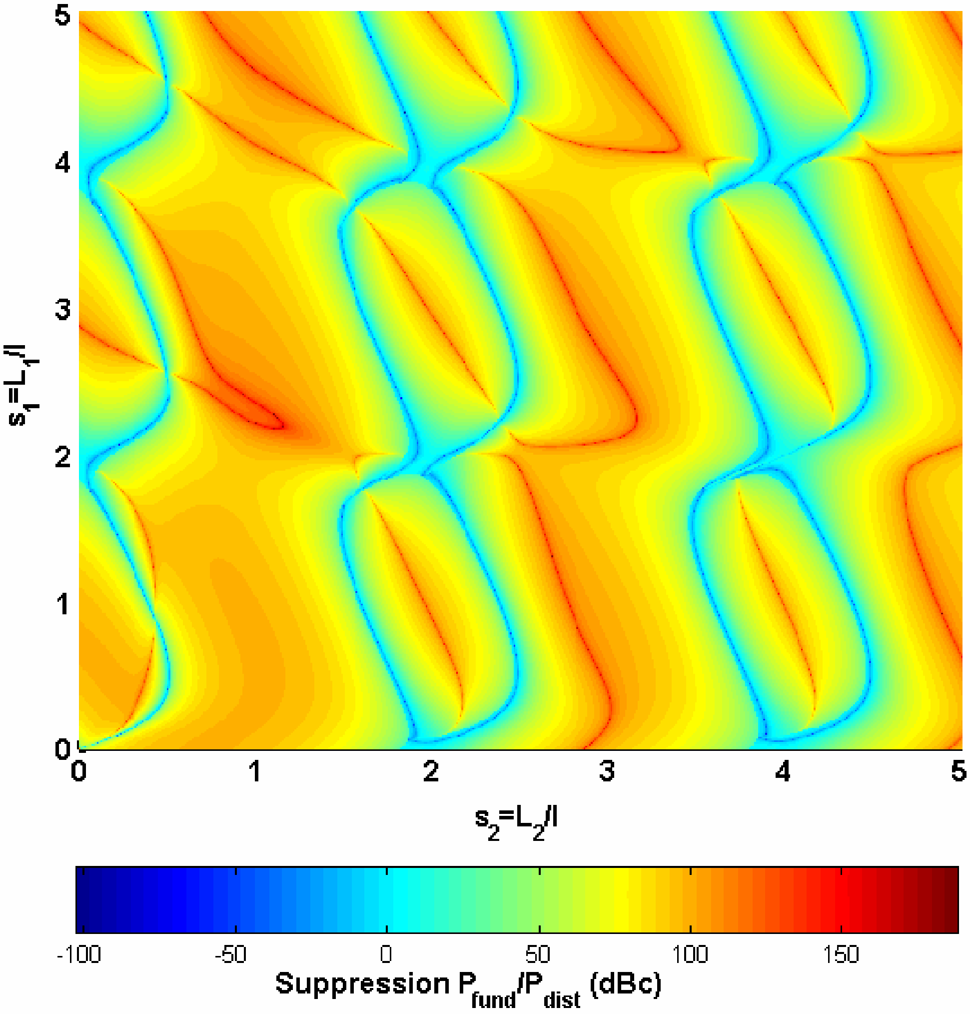

Figure 5.2 Relative level of the nonlinear distortion of the two-section Y-fed directional coupler versus the normalized section lengths

An IYCM2 ($s_1 = 2.86057$, $s_2 = 2.86057$) possesses a high distortion-suppression, a mediate driving voltage, and an excellent maximum-modulation depth. More importantly, it also has an excellent linearity performance at high operation frequencies, which will be discussed in Chapter 7. It will be worthwhile to further explore the IYCM2 experimentally.

Table 5.1 The properties of Y-fed directional couplers

Modulator Name	IYCM1	IYCM2	IYCM3	IYCM4	NYCM	MZM
Type	DC*	DC	DC	DC	DC	MZ**
Normalized 1st Section Length: S_1	2.17530	2.86057	2.12870	2.86050	0.70711	__
Normalized 2nd Section Length: S_2	1.14640	2.86057	3.09290	0.00000	0.00000	__
Distortion Suppression* (DS) (dB)**	187	183	180	172	98	98
Normalized Driving Voltage****	3.34	3.76	5.52	3.41	1.00	0.72
Maximum Modulation Depth	0.95	0.97	0.78	0.73	1.00	1.00

* DC: directional coupler
** MZ: Mach-zehnder interferometer
*** The Distortion Suppression is calculated at 1% modulation depths
**** The Driving Voltages are normalized to the value of the NYCM

5.4. DEVICE FABRICATION

A modulator, IYCM, which has similar normalized interaction lengths with those of the IYCM2, was demonstrated, employing the U9020D:FTC/PU:UV11-3 waveguide described in Chapter 3. In our design, both the first and the second interaction lengths are 1cm, and the waveguide separation is 4 μm. The rib depth was fine-tuned experimentally for obtaining the target normalized interaction length of about 2.86 for both the sections.

The U9020D:FTC/PU:UV11-3 waveguides were first fabricated using the processes described in Section 3.4. They were then poled employing the domain-inversion poling method as described in Section 2.3.3. To be used as the bottom electrode, a Cr(50Å)/Au(2000Å) layer was deposited on a <100> silicon wafer substrate. A 3μm-thick layer of Ultradel 9120 was coated on as the bottom cladding. The EO polymer was spin-coated onto the bottom cladding and then was patterned and etched to make the single-mode waveguides by the oxygen RIE technique. A 3μm thick layer of UV-curable polymer NOA61 was used as the top cladding. Then the top electrodes (Au, 2000 Å) were deposited by the electron beam method and patterned with the wet etching method. Finally, the device was poled and tested.

5.5. DEVICE TESTING AND EXPERIMENTAL RESULTS

The modulator was tested on a 5-axis waveguide coupling stage. Figure 5.3 is the schematic diagram for the intermodulation distortion measurements. A light beam from an Nd:YVO_4 laser (100μW, λ=1.34μm) polarized in the TM direction was coupled into and out of the modulator with two 60X objective lens respectively. The output light was received with a gain-switchable InGaAs detector (Thorlabs PDA400) connected to an HP8563E spectrum analyzer. Two sinusoidal modulating signals of equal amplitude at frequencies of 10 and 11 kHz from an HP 8904A multifunction synthesizer were combined and applied to the driving electrodes. The switching voltage of the IYCM was determined to be 12.5V, resulting in a maximum modulation depth of 97.6%. The experimental results, shown in Figure 5.4, with dots for the third-order intermodulation distortions (IMD3) and squares for the fundamentals, agreed well with the fitting curves for the IYCM modulator with s1=s2=2.85, except for the narrow sharp dip areas which was due to the sensitivity limitations of our testing system. To further confirm the suppression, we compared the experimental results of this IYCM to an NYCM with s=0.707. Figure 5.5 shows the spectrum analyzer displays of the outputs of these two modulators, where both were driven to 20% optical modulation depth and to the same fundamental level. For the NYCM, the IMD3 was 46.55dBc lower than the fundamental peak, while the IMD3 for the IYCM was 93.84dBc lower (below the noise level). In other words, the IMD3 level of the NYCM was 47.29dB higher than that of the IYCM. Therefore, a suppression of 47.29dB was obtained.

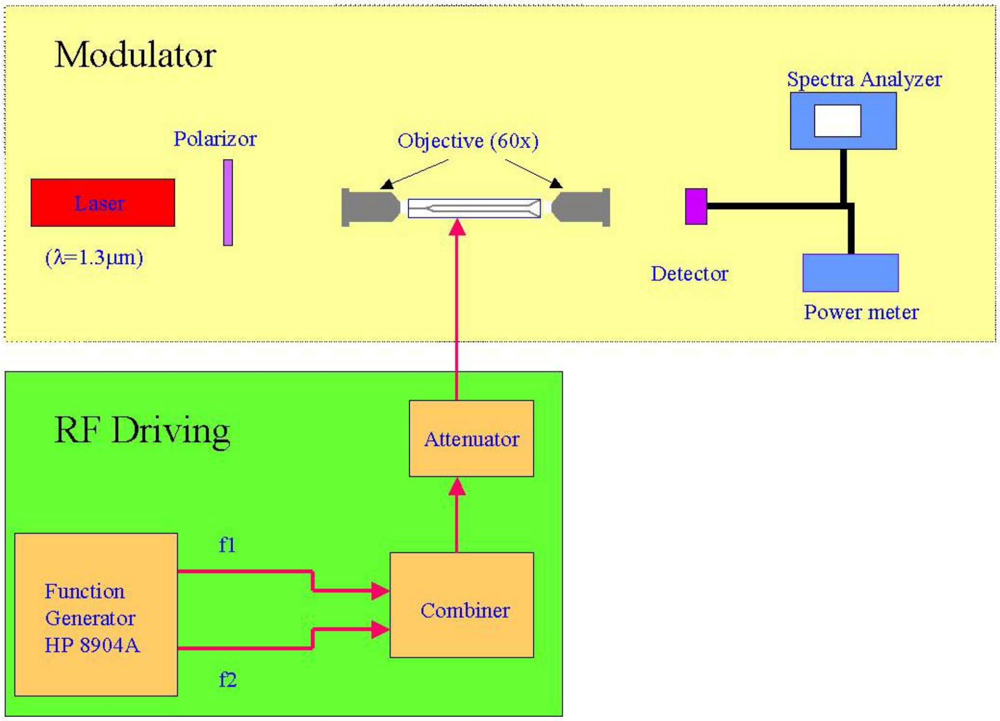

Figure 5.3. Setup for measurement of the modulator’s IMD

5.6. SUMMARY

The linearity properties of the two-section Y-fed directional couplers were theoretically and experimentally investigated in terms of the nonlinear distortion suppression. The theoretical results show that high-linear modulation can be achieved by properly choosing the normalized interaction lengths of the two sections. A polymeric two-section Y-fed directional coupler was demonstrated by employing the Δβ−inversion technique. Substantial suppressions were achieved by this modulator in a large range of modulation depths. An IMD3 suppression of 47.29dB was obtained by this modulator over that of a conventional Y-fed directional coupler at 20% modulation depth.

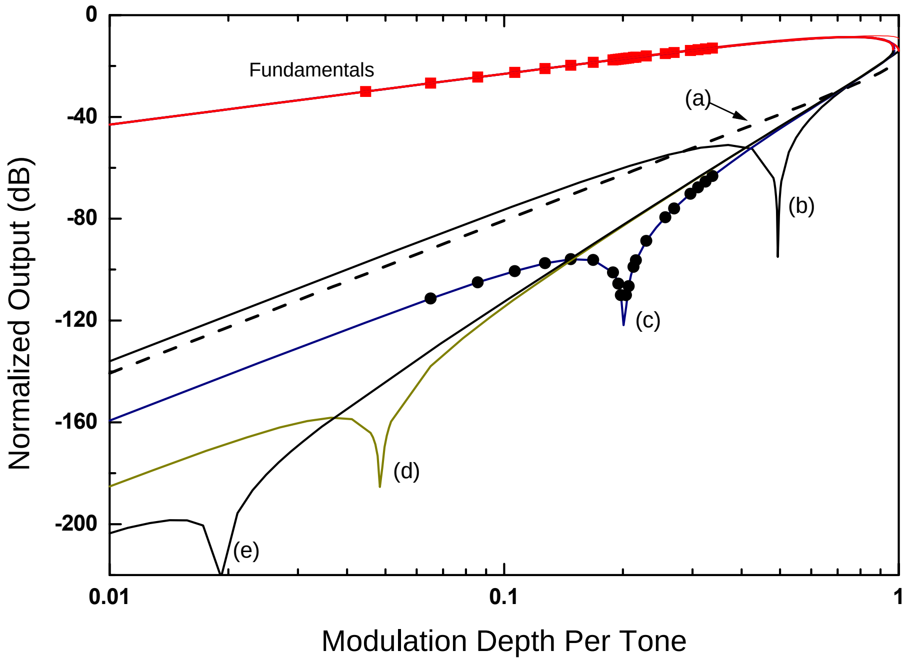

Figure 5.4. The simulated and experimental output powers of fundamentals and IMDs for different modulators versus their optical modulation depth (The vertical axis is normalized to the input power.): (a) NYCM ($s_1 = 0.707, s_2 = 0$) ; (b) IYCM ($s_1 = s_2 = 2.7715$) ; (c) IYCM ($s_1 = s_2 = 2.8500$) ; (d) IYCM ($s_1 = s_2 = 2.8600$) ; (e) IYCM ($s_1 = s_2 = 2.8605$) . The dots and squares in the figure are experimental results for an IYCM fitting with $s_1 = s_2 = 2.8500$. The square and dots in the figure are experimental data.

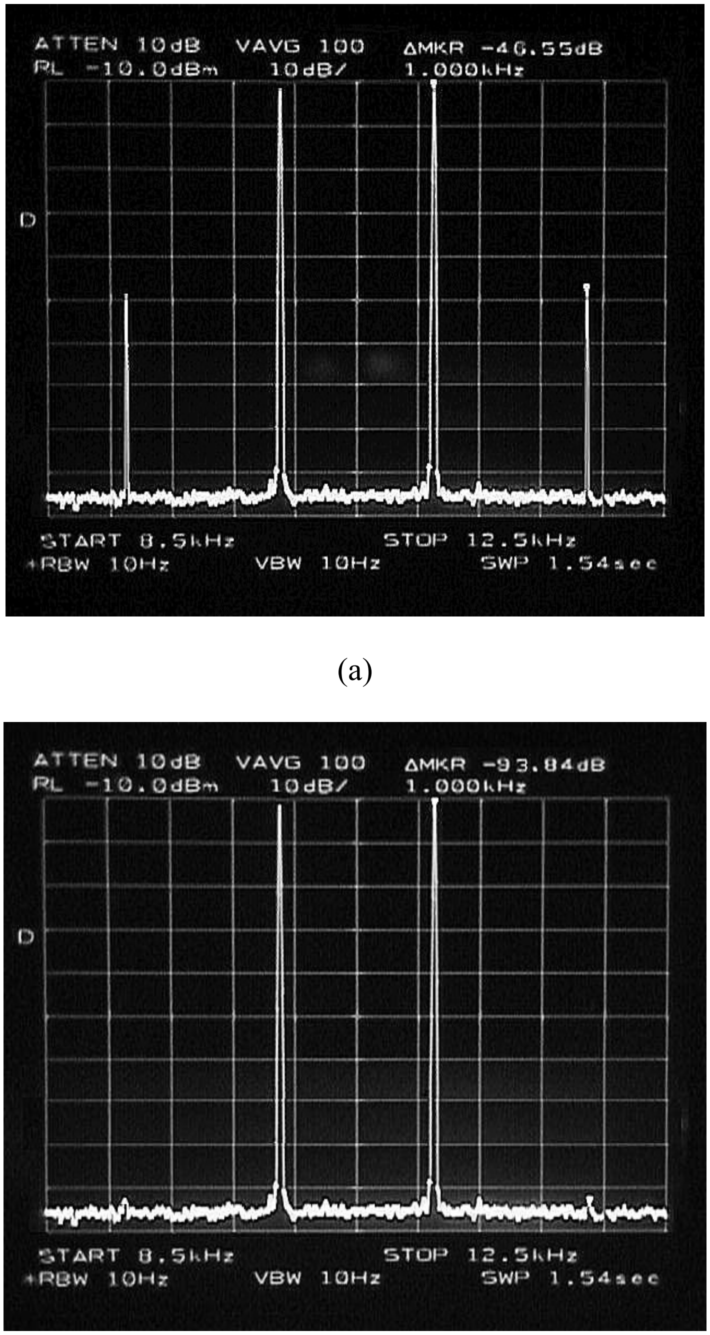

(a)

(b)

Figure 5.5. Displays on an oscilloscope of the fundamentals and IMD3s (a) for a conventional modulator; and (b) for a Δβ inverted modulator, where the IMDs were suppressed by 47.29 dB

Chapter 6 Traveling-Wave Electrode Design and Fabrication

6.1 INTRODUCTION

The Y-fed directional couplers have merit for fabricating bias-free and high-linear modulators. In order for them to be used in applications such as CATV, antenna remoting, etc., these modulators must be able to operate on RF or even microwave frequencies. For applications higher than 1 GHz, traveling-wave (TW) electrodes, as shown in Figure 6.1, are mandatory in overcoming the limitations resulting from inter-electrode capacitance and finite transit time. In this chapter, we will discuss the design and fabrication of TW electrodes for EO polymer-based directional couplers.

To find the optimal driving voltage and bandwidth for electro-optic (EO) polymer-waveguide-based directional couplers, four electrode structures are investigated in Section 6.2. An efficient simulation method for TW properties based on conformal-mapping is presented and used to optimize the electrode dimensions in Section 6.3. The taper regions and test structures are described in Section 6.4. The fabrication and testing of these TW electrodes are presented in Section 6.5. Note that, although we use the Y-fed directional coupler as the waveguide structure in both the theoretical and experimental investigations in this chapter, the traveling-wave electrodes discussed in this paper should generally be valid for a polymeric EO modulator based on any directional-coupler structures where the two optical waveguides are coplanar.

6.2 ELECTRODE STRUCTURES

6.2.1 Four candidate electrode structures

For an EO polymer-based high-speed directional coupler, the task of the traveling-wave electrode is to generate an electrical field whose vertical components are different in the two parallel optical waveguides. This field difference induces a difference between the effective indexes of the two waveguides, thus modulating the output optical intensities.

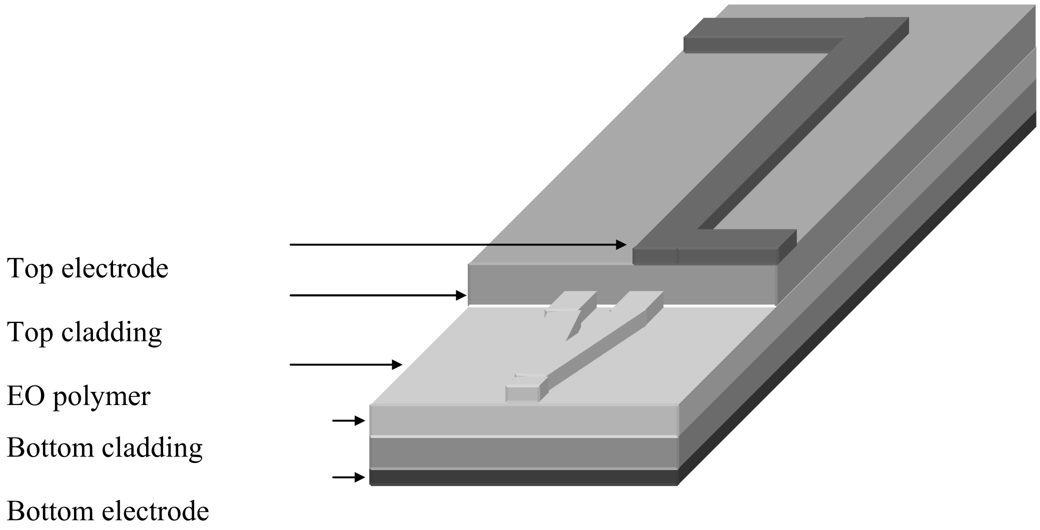

Figure 6.1. Schematic of an EO polymer-based directional coupler with a microstrip line

For an EO polymer-based high-speed Mach-Zehnder (MZ) modulator, the traveling-wave electrode is usually a microstrip line. The bottom electrode of the microstrip line is necessary for the poling process. When the EO-polymer layer is uniformly poled vertically, the microstrip line is usually applied to only one of the two arms of the MZ modulator. The electrode-induced electrical field in the other arm is almost zero since the separation between the two optical arms of an MZ modulator is much larger than the polymer layer (including the bottom cladding, active EO polymer layer, and top cladding) thickness (denoted by 'h'). However, the situation is quite different for polymer-based directional couplers since their optical waveguide separations are comparable to their polymer layer thickness, which is ~10 μm including the top and bottom claddings. Figure 6.2 shows a microstrip line's electrical field intensity (vertical component only) along the centerline of the polymer layers. The microstrip line that generated this electrical field is also shown in the same figure. In the figure, all the lengths are denoted in units of the polymer-layer thickness (h), and the electrical field intensity is normalized. The electrical field shown in Figure 6.2 is obtained by solving the Poisson equation. The dielectric constants of the polymers (again including the bottom cladding, EO layer, and top cladding) are equal to 2.40 in the calculation. Based on this figure, it is obvious that, if the optical waveguide separation is comparable to the polymer-layer thickness, the difference between the vertical electrical fields in the two optical waveguides will not be large. Since the modulated signal is proportional to the electrode-induced vertical electrical-field difference, and the microstrip line can not effectively induce such a field difference, the microstrip line is not an efficient traveling-wave electrode structure for the polymer-based directional coupler, and it is worthwhile to explore other electrode structures.

In order to find the optimal traveling-wave electrode formation for the EO polymer-based directional coupler, four electrode structures, as shown in Figure 6.3, are evaluated and compared in this paper by calculating the modulators' driving voltages and bandwidths, and by experimentally measuring their performance features. The four structures are (1) the microstrip line (MSL), (2) the asymmetric coplanar waveguide with ground (ACWG), (3) the coplanar waveguide with ground (CPWG), and (4) the edge-coupled microstrip line (CMSL).

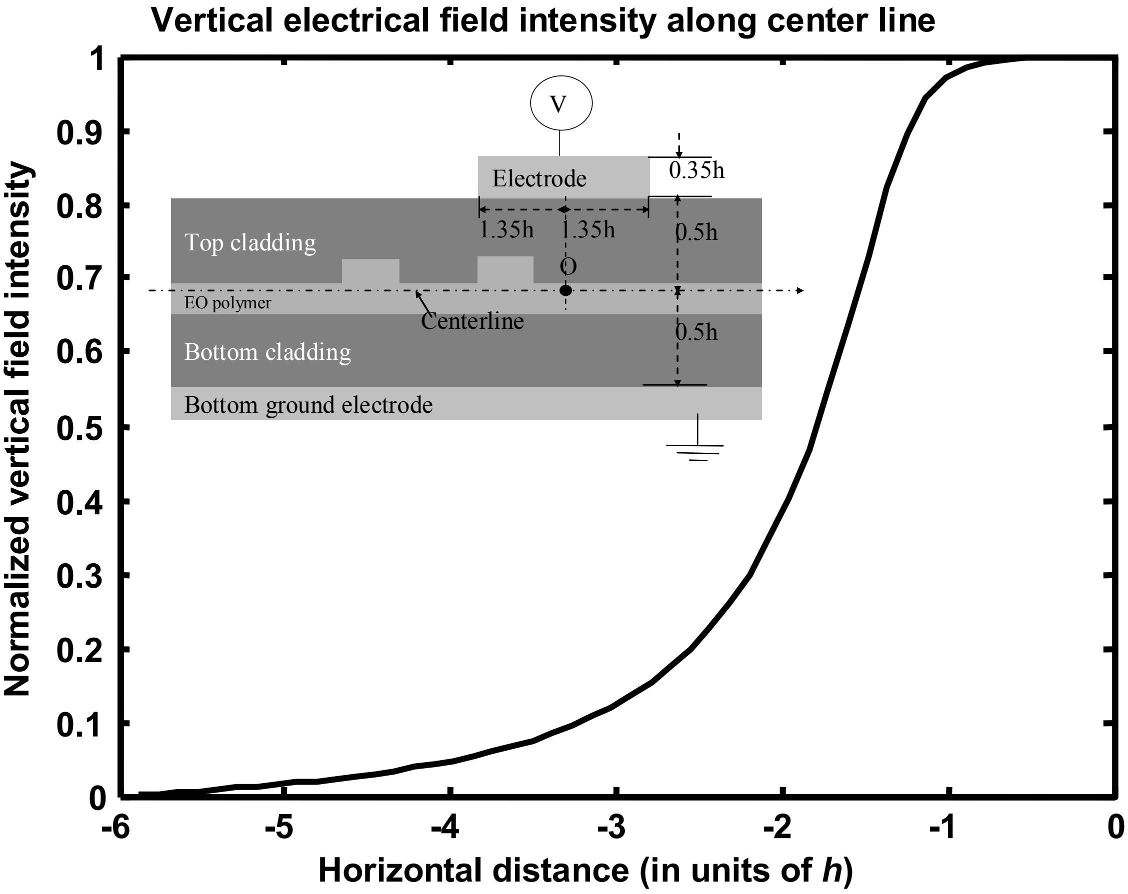

Figure 6.2. Vertical electrical field distribution along the centerline of the polymer layers (including the bottom cladding, EO polymer layer, and top cladding). The microstrip line that generated this field is also shown in the figure. (The original point of the horizontal distance axis corresponds to the "O" point shown in the picture.)

6.2.2 Waveguide and electrode dimensions

The TW electrode designed here is intended to be used to modulate UV15:DR1/PMMA:UV11-3 and UV15:CLD1/APC:UV11-3 waveguides operating at 1.55μm wavelength. The interaction length is set to be 2.0 cm for the

UV15:DR1/PMMA:UV11-3 modulators and 1 cm for the UV15:CLD1/APC:UV11-3, respectively, to optimize performance, which will be delineated in Chapter 7. Using the simulation results of the beam propagation method (BPM) for guidance, experiments were performed to find proper waveguide separations and rib depths with which the conversion lengths are around 2.8 cm and 1.4 cm, respectively, for DR1 and CLD1 modulators. In this case, their normalized interaction lengths are around $\sqrt{2}$; thus one arm of these Y-fed directional couplers can be switched off using the lowest driving voltages. All related parameters of the optical waveguides are listed on Table 6.1.

Table 6.1 Waveguide materials and parameters

WG No.	Bottom cladding			EO polymer layer					Top cladding			Effective index
	Material	Index	Thickness (μm)	Material	Index	Thickness (μm)	Rib depth (μm)	Waveguide separation* (μm)	Material	Index	Thickness (μm)	
1	UV15	1.501	4.0	DR1/PMMA	1.55	4.0	1.44	13.0	UV11-3	1.506	4.0	1.532
2	UV15	1.501	3.0	CLD1/APC	1.612	2.5	0.49	10.0	UV11-3	1.506	3.0	1.574

* Waveguides separation refers to the distance between the inner edges of the two optical channels.

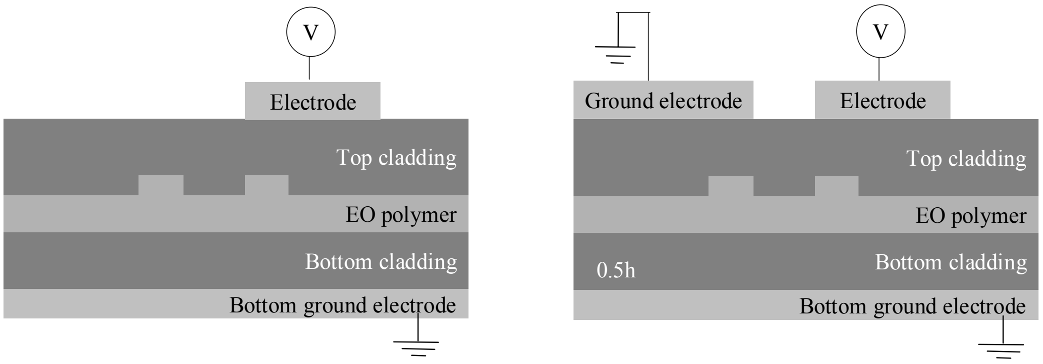

(1) Microstrip line (MSL)

(2) Asymmetric Coplanar waveguide with ground (ASWG)

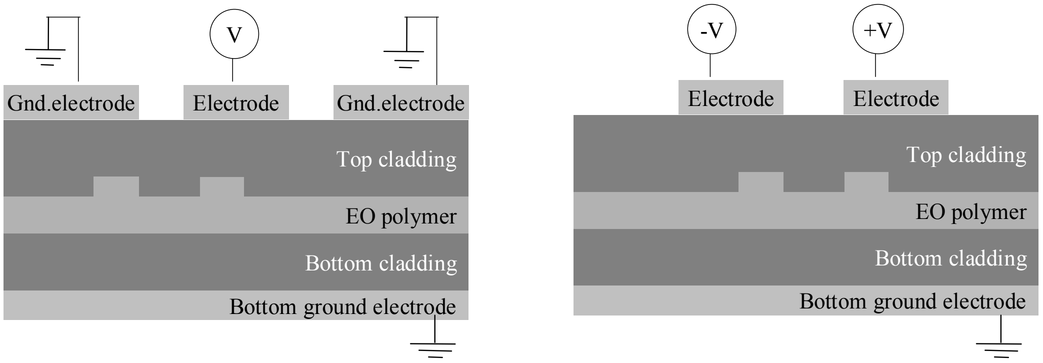

(3) Coplanar waveguide with ground (CPWG)

(4) Coupled microstripe line (CMSL)

Figure 6.3. Schematic of traveling-wave electrodes for EO polymer-based directional Couplers

As shown in Figure 6.3, four electrode structures are candidates here for the directional-coupler-based polymeric modulators. The electrode dimensions, which satisfy the 50Ω-characteristic-impedance requirement, are calculated using the finite element method. In these calculations, the polymers' dielectric constants are assumed to be equal to the square of their refractive indexes. The electrode's conductivity is set to be $4.1 \times 10^7 S/m$ for Gold. The calculated electrode dimensions and their characteristic parameters are given on Table 6.2.

Table 6.2 Electrode parameters

Polymer material	Electrode structure	Polymer thickness (µm)	Top electrode thickness (µm)	Bottom electrode thickness (µm)	Active electrode width (µm)	Electrode gap (µm)	Effective Index	Conductor loss (dB/cm/$\sqrt{GHz}$)
UV15: DR1/PMMA: UV11-3	MSL	12	3	2.4	35	12	1.42748	0.251067
	ACWG	12	3	2.4	33	12	1.40563	0.25901
	CPWG	12	3	2.4	31	12	1.3841	0.271244
	CMSL	12	3	2.4	26	12	1.34998	0.275128
UV15: CLD1/APC: UV11-3	MSL	8.5	3	2.4	24	10	1.42712	0.336661
	ACWG	8.5	3	2.4	23	10	1.40852	0.34459
	CPWG	8.5	3	2.4	22	10	1.39118	0.359211
	CMSL	8.5	3	2.4	18	10	1.35779	0.360226

6.2.3 Driving voltage

In this section, the four traveling-wave electrode structures are compared in terms of the driving voltages of the modulators that use these electrodes. The driving voltages are evaluated both theoretically and experimentally. In the four DR1-based modulators, the left edge of the right optical waveguide is located 0.5µm right corresponding to the left edge of the active electrode. In the four CLD1-based modulators, the left edge of the right waveguide is vertically aligned to the left edge of the active electrode.

The driving voltages are first theoretically calculated using the BPM method. The detailed calculation steps are listed below:

1) For a given applied voltage, the Poisson equation is solved to derive the electrical field distribution.

2) The index changes of the TM modes are calculated using $\Delta n = -0.5 n^3 \gamma_{33} E$, where n is the EO polymer's refractive index, γ_{33} is the EO efficient, and E is the electrical field in the vertical direction.
3) The output optical intensity is calculated using the beam propagation method based on the index distribution obtained in the second step.
4) Change the driving voltage value and repeat Steps (1) – (3).

Figure 6.4 gives the modulation curves of the modulators with varying electrode structures. In these calculations, γ_{33} of CLD1/APC is equal to 40 pm/v, and γ_{33} of DR1/PMMA is equal to 10 pm/v.

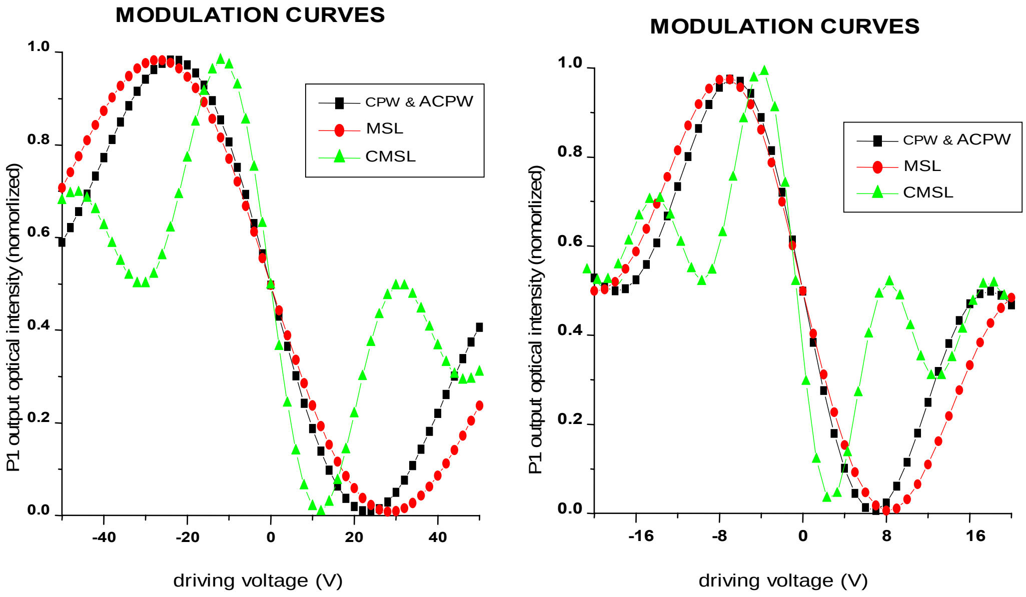

(a)

(b)

Figure 6.4. Modulation curves of EO polymer-based Y-fed directional couplers with various electrode structures: (a) DR1 directional couplers; (b) CLD1 directional couplers

The DR1-based modulators described above were fabricated and their driving-voltages were tested. The fabrication steps are listed below: (1) 0.5μm Al is deposited on silicon wafers. (2) UV15 is diluted with cyclopantanone, then a thin layer of UV15 is spin-coated on and UV-cured to serve as the bottom cladding. (3) The DR1/PMMA is dissolved into the cyclopentanone and the solution is then used to spin-coat an EO polymer layer. (4)A normal photolithography process is used to pattern the optical waveguide. (5) Waveguides are etched using RIE with oxygen and nitrogen. (6) A UV11-3 layer is coated on and UV-cured to serve as the top cladding. (7) A 0.5μm Al layer is deposited onto the top cladding to serve as both the poling electrode and the top electrode. (8) The samples are poled for 30 minutes using 1100V voltage. (9) The top electrodes are patterned using photolithography. (9) The samples are cleaved and are then ready for testing.

The fabricated modulators are tested at 1.55 μm using a Santec ECL-200 laser. The input single mode fiber is aligned to the waveguide, and the output is collected by a 40× objective lens and coupled to a photodetector. A fiber-optical polarization controller is used to adjust the input polarization to the TM.

In order to obtain the driving voltages of different electrode structures, an array of modulators with these different electrode structures are fabricated onto each chip. The switch voltage, V_s, is measured by applying a 1KHz signal. Figure 6.5 (a), (b), (c), and (d) show the modulation and the modulated signals of four modulators having different electrode structures. In each subfigure, the sinusoidal curve is the modulation signal (electrical); the other curve, which has more curvatures, is the modulated signal (optical); the horizontal axis is the time axis (200 μsec per division), and the vertical direction shows the voltage for the modulation signal (10V per division); and the optical intensity for the modulated signal. These measurements show that the switch voltages of the modulators under test are 24V for the CMSL, 48V for the ACWG and CPWG, and 60V for the MSL. Although the measured switch voltages from different Si wafers vary, the ratios between the measured switch voltages of the modulators with different electrode structures obtained from the same Si wafer are fixed. The ratios between the measured switch voltages of the modulators with different electrode structures are 1(CMSL) : 2(ACWG) : 2(CPWG) : 2.5(MSL).

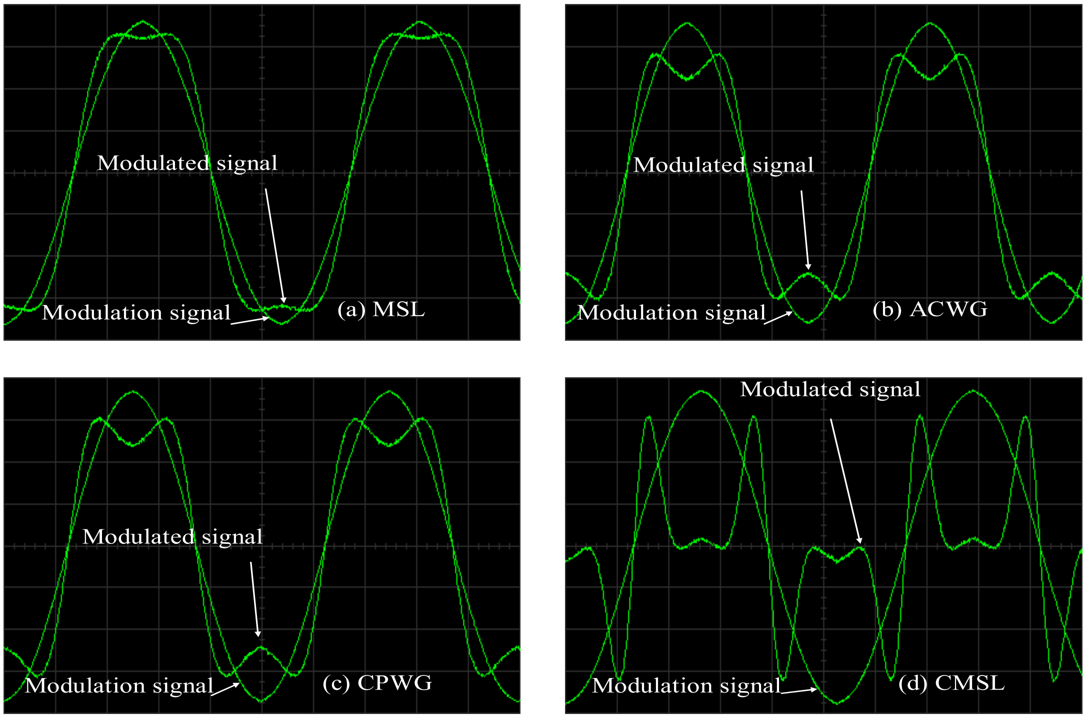

Figure 6.5. Measured modulation and modulated signals of UV15:PMMA/DR1:UV11-3 based Y-fed directional couplers with different electrode structures: (a) MSL, (b) ACWG, (c) CPWG and (d) CMSL.

The ratios between the driving voltages of different electrode structures agree well with the simulation results. Both the experimental and simulation results show that using CMLs, CPWGs or ACWGs can reduce the driving voltages. The CMSL is the best electrode structure in terms of driving voltage. When the electrodes' top electrode separations are the same and have a value similar to the polymer layer thickness, the CMSL's driving voltage is only half that of the CPWG or the ACWG; the CPWG and the ACWG have almost the same driving voltage; the MSL has the largest driving voltage, 20%-25% higher than the driving voltages of the CPWG and the ACWG.

6.2.4 Bandwidth

The bandwidth was estimated using the small-signal analysis method reported in Ref. [60]. Based on Equation (22) in Ref. [60] as well as on the optical refractive index, the microwave refractive index, and the attenuation constant obtained in Section 6.2.2, the frequency responses of the directional coupler were derived. Figure 6.6 (a) and (b) show the calculated frequency responses of Y-fed directional couplers made of UV15:DR1/PMMA:UV11-3 and of those made of UV15:CLD1/APC:UV11-3 respectively. The different lines in these figures correspond to the couplers with different electrode structures. The calculated 3-dB bandwidths of DR1 modulators with different electrode structures are 92 GHz (MSL), 77 GHz (ACWG), 66 GHz (CPWG), 54 GHz (CMSL). The 3-dB bandwidths of CLD1 modulators are 135 GHz (MSL), 121 GHz (ACWG), 109 GHz (CPWG), and 93 GHz (CMSL).

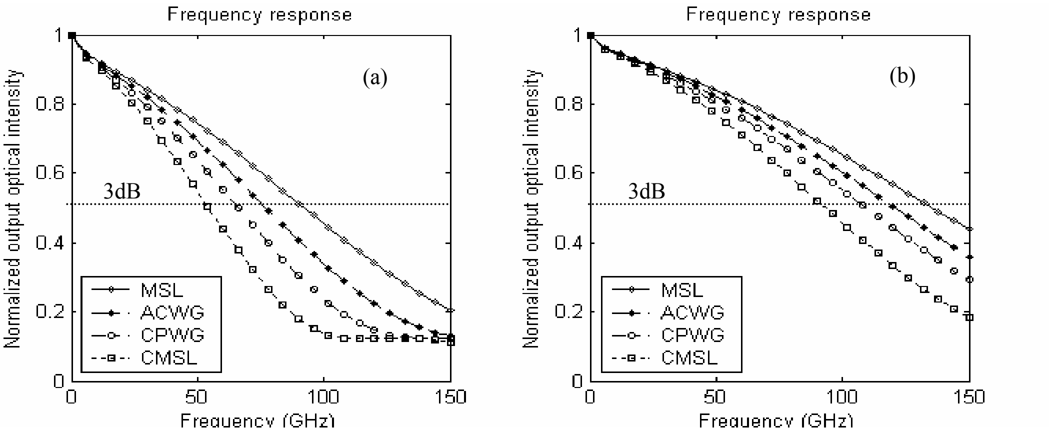

Figure 6.6. Frequency responses of EO polymer-based Y-fed directional couplers with different electrode structures: (a) DR1 directional couplers, and (b) CLD1 directional couplers

6.2.5 Conclusion

For electrodes with the same top electrode separations, a directional-coupler-based modulator with a CMSL has the lowest driving voltage, but its bandwidth is also the smallest; a modulator with an MSL has the largest driving voltage and the largest bandwidth; the driving voltage of a modulator with a CPWG is almost the same as that of a modulator with an ACWG; a modulator with a CPWG has a smaller bandwidth compared to that of a modulator with an ACWG. The experimental results for the driving voltage agree with the modeling results.

The results obtained in this paper indicate a trade-off between the driving voltages and the bandwidths. Different electrode structures may be suitable for different applications. If the EO polymer has a relatively smaller EO coefficient and the driving voltage is a critical concern, the CMSL is the best choice. On the other hand, if the EO polymer has a relatively larger EO coefficient or the bandwidth is the critical concern, the MSL may be the best choice. The CPWG and the ACWG are satisfactory for normal cases since their driving voltages are around 25% lower than those of an MSL and their bandwidths 20%~40% larger than those of a CMSL.

Taking into account the capability of a CPWG to achieve Δβ inversion, the CPWG is the choice of design for this research.

6.3 ELECTRODE OPTIMIZATION

The TW electrode geometry needs to be optimized to minimize propagation loss, speed mismatch, and low driving voltage. Such an optimization can be achieved by exploring the related parameters of the cross-section of the electrodes using a suitable analytical or numerical method. In this section, we will present a simulation method for the optimization of CPWG electrodes.

For a CPWG with arbitrary metal thickness and trapezoidal angles as shown in Figure 6.7, numerical methods seem the only candidate for the optimization task since the analytical approach can deal only with quite simple cross-sections. At present, the main numerical analysis tools are the quasi-static finite-element method (QS-FEM)[67]-[69] and the full-wave finite-element method (FW-FEM)[70]. Unfortunately, both of these are too time-consuming for a detailed exploration of the design's parameter space. Another important technique used in the study of microwave transmission lines in quasi-static approximation is the Conformal Mapping (CM) method, which directly enables the evaluation of the line capacitance and, therefore, the inductance. The skin-effect line resistance can also then be evaluated, while suitable approximation can also be found for the line capacitance and conductance in the presence of dielectrics. The computational efficiency of the CM approach is adequate to fulfill the task here (1) if a parameter determination method based on the conformal mapping results can be found and (2) if an effective conformal mapping tool is available. In this paper, we present an approach for evaluating the characteristic parameters for a traveling-wave electrode with a CPWG structure and with arbitrary symmetric polygon geometry based on the numerical CM solutions provided by the Schwarz-Christoffel (SC)[71]-[73] toolbox, which is a collection of MATLAB functions for interactive computation and for visualization of the Schwarz-Christoffel conformal mapping.

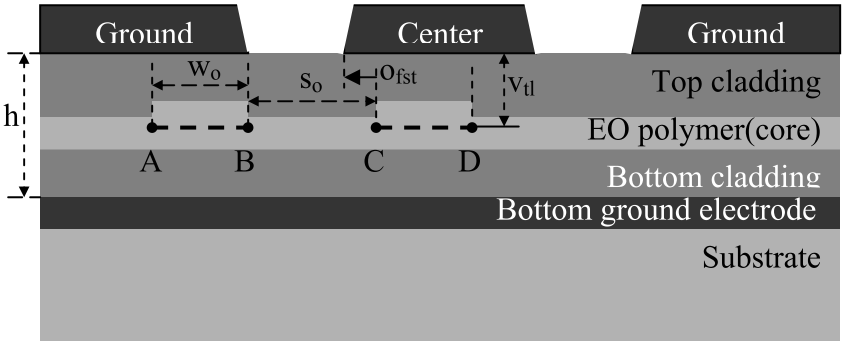

Figure 6.7. Cross-section of a polymeric EO modulator based on a directional coupler (h: polymer thickness, o_{fst}: waveguide position offset, AB & CD: test lines for calculating E_{diff}, v_{tl}= 0.5×h, w_o: waveguide width, s_o: waveguide separation)

Section 6.3 is organized as follow. The method for calculating the characteristic parameters for a CPWG with symmetric polygon geometry is introduced in 6.3.1. The results of this approach are validated through a comparison with an FW-FEM solution. In 6.3.2, a novel method for evaluating the electrode efficiency is presented, and the electrode geometry is optimized in terms of bandwidth and electrode efficiency by exploring the electrode's parameter space. (Here, “electrode efficiency” refers to the ability of the traveling-wave electrode to generate effective electrical fields that can modulate the optical signals; this subject is explained further at a later point.) The basic conclusions are given in 6.3.3.

6.3.1 Characteristic parameter calculation

Since the differences between the refractive indexes of the cladding materials and those of the core EO polymers are small, in order to simplify the calculation in this paper, we represent the cladding and core combination by a uniform distributed dielectric which we refer to as the UPD (Uniform Polymer Dielectric). The influence of ε_r, which denotes the UPD's dielectric constant in RF frequencies, on the modulators' properties is evaluated in Section III, where the value of ε_r is set to be in a range around the square of the UPD's refractive index in infrared frequencies, based on the fact that polymeric materials have low dispersion in the index of refraction between infrared and microwave frequencies.

The first step in calculating characteristic parameters using the conformal mapping method is to map the electrode geometry in the physical plane into a plane in which the electrode has a simpler geometry, usually a rectangle; hence the electrodes' characteristic parameters can then be easily evaluated. Under the uniform-polymer-dielectric assumption discussed in the previous paragraph, the cross-section shown in Figure 6.7 can be simplified to Figure 6.8(a), where the geometry of a symmetric CPWG with an arbitrary symmetric polygon geometry is described by seven geometric parameters (w, s, t_a, t_g, β_a, β_g, and h, where angles β_a and β_g are positive for over-cut electrodes). The half-structure (shown in Figure 6.8(b)) is simply a connected polygon with nine sides, $w_1 \rightarrow w_2 \rightarrow w_3 \rightarrow w_4 \rightarrow w_5 \rightarrow w_6 \rightarrow w_7 \rightarrow w_8 \rightarrow w_9 \rightarrow w_1$, where w_5 and w_8 are infinite vertices. Among these sides, there are two and only two non-metal sides, $w_4 \rightarrow w_5$ and $w_9 \rightarrow w_1$, along which the electrical field is parallel to the sides due to symmetry. If this polygon is transformed into a rectangle with a pair of opposite sides that are the images of these two non-metal sides, the rectangle is simply a parallel plate capacitor with two magnetic boundaries, and the characteristic parameters evaluation will be straightforward. This kind of mapping can be done easily by the SC toolbox following a method similar to that presented in ref. [71]. The vertices coordinators and the corresponding internal angles $\pi\alpha_1, \ldots , \pi\alpha_9$ are also shown in Figure 6.8(b) in terms of the geometric parameters of the transmission line. The polygon in the physical domain may be first transformed into the upper-half plane, the canonical domain shown in Figure 6.9(a), by means of an SC mapping; it is then transformed into the parallel plates of a rectangle, shown in Figure 6.9(b), via an inverse close-form SC mapping. Here, $z_1, \ldots , z_9$ and $\eta_1, \ldots , \eta_9$ are the corresponding images of vertices $w_1, \ldots, w_9$ in the canonical domain and in the rectangle domain respectively. The curve between z_2 and z_7 and that between η_2 and η_7 are the corresponding dielectric-air interfaces.

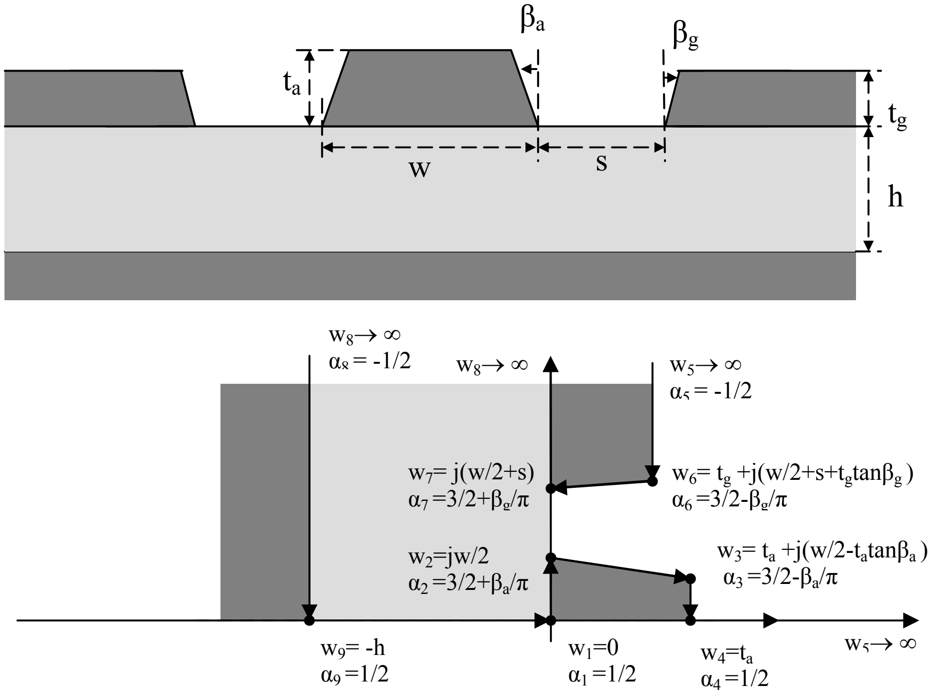

Figure 6.8. Cross-section of a trapezoidal CPWG and parametric representation of the corresponding polygon in the physical domain. The coordinators of the vertices ω_i (i = 1-9) and the internal angle at the vertices $\pi\alpha_i$ (i = 1-9) are also reported.

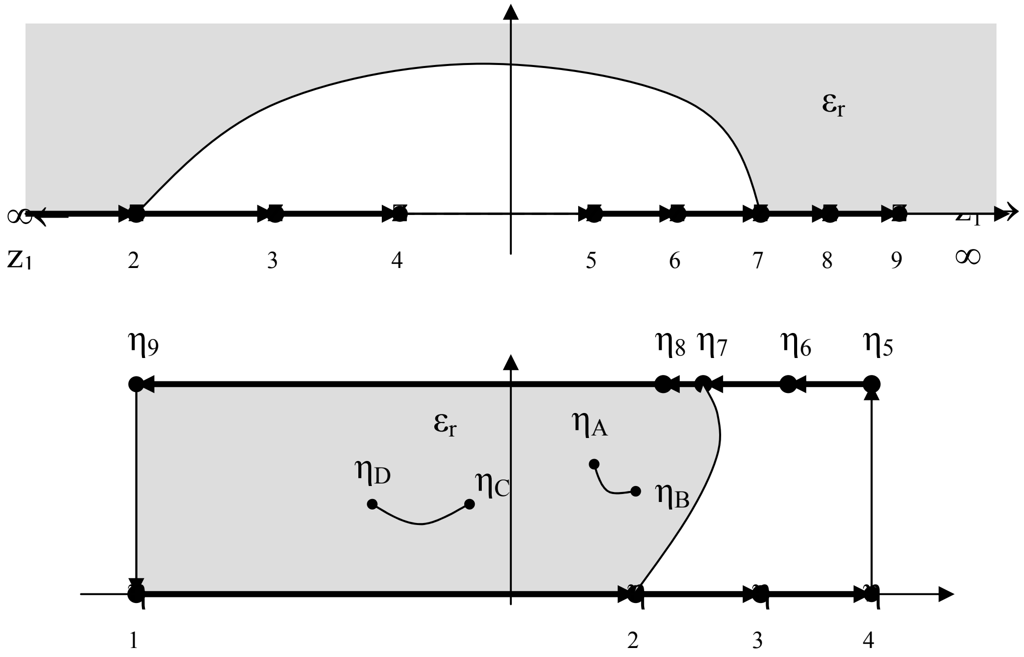

Figure 6.9. Mapping of the trapezoidal CPWG into the canonical plane and final transformation into a rectangle region (parallel plate capacitor). (Curves Z_2Z_7 and $\eta_2\eta_7$ are the images of the dielectric-air interface in the canonical and rectangle planes respectively; Curves $\eta_A\eta_B$ and $\eta_C\eta_D$ are the images of the test lines shown in Figure 6.7.)

The second step is to determine the characteristic parameters based on the conformal mapping solutions obtained in the first step. Here, we directly evaluate the four basic parameters: capacitance (C), inductance (L), conductance (G), and resistance (R). Then, we calculate the characteristic impedance (Z) and the propagation constant (γ) based on the values of C, L, G, and R using the well-known formulas $\gamma = \sqrt{(R + j\omega L)(G + j\omega C)}$ and $Z = \sqrt{(R + j\omega L)/(G + j\omega C)}$. The detailed approach is described below:

1) Capacitance

When no dielectric is presented, the capacitance (C_0) per unit length can be easily obtained by [71]

$$C_0 = 2\varepsilon_0 \frac{|\eta_{4,x} - \eta_{1,x}|}{|\eta_{5,y} - \eta_{4,y}|} \quad ,$$

(Equation 6.1)

where $\varepsilon_0 = 1/\mu_0 c^2$, $\mu_0 = 4\pi \bullet 10^{-7} H/m$, and $\eta_{i,x}$ and $\eta_{i,y}$ represent the x and y components of point η_i (i = 1, … , 9) in the rectangle plane, respectively. (These denotations will be used throughout the paper).

When a dielectric is presented, the best way to determine C is to solve the Laplace equation in the rectangle domain. However, to do so is too time-consuming for the optimization procedures. Here, we propose an approximation method for calculating C by assuming that the electrical fields at all points in the rectangle are perpendicular to the metal edges in the rectangle domain even when the dielectric is presented, as shown in Figure 6.10. Under this direction-maintained assumption, C may be computed as

$$C = 2\varepsilon_0 \left[\varepsilon_r \frac{|\eta_{2,x} - \eta_{1,x}|}{|\eta_{5,y} - \eta_{4,y}|} + \int_{\eta_{2,x}}^{\eta_{\max 1,x}} \frac{dx}{(\eta_{5,y} - \eta_{4,y}) - (1 - \frac{1}{\varepsilon_r})[f_1(x) - f_2(x)]} + \frac{|\eta_{4,x} - \eta_{\max 1,x}|}{|\eta_{5,y} - \eta_{4,y}|} \right] ,$$

(Equation 6.2)

where

$$f_1(x) = \begin{cases} \eta_{7,y} \text{ when } \eta_{2,x} \le x \le \eta_{7,x} \\ \text{the interface curve from } \eta_7 \to \eta_{\max}, \text{ when } \eta_{7,x} \le x \le \eta_{\max,x} \end{cases} ,$$

$$f_2(x) = \text{the interface curve from } \eta_2 \to \eta_{\max}, \text{ when } \eta_{2,x} \le x \le \eta_{\max,x}$$

and η_{max} is the point in the interface curve which has the largest x coordinator, as shown in Figure 6.10.

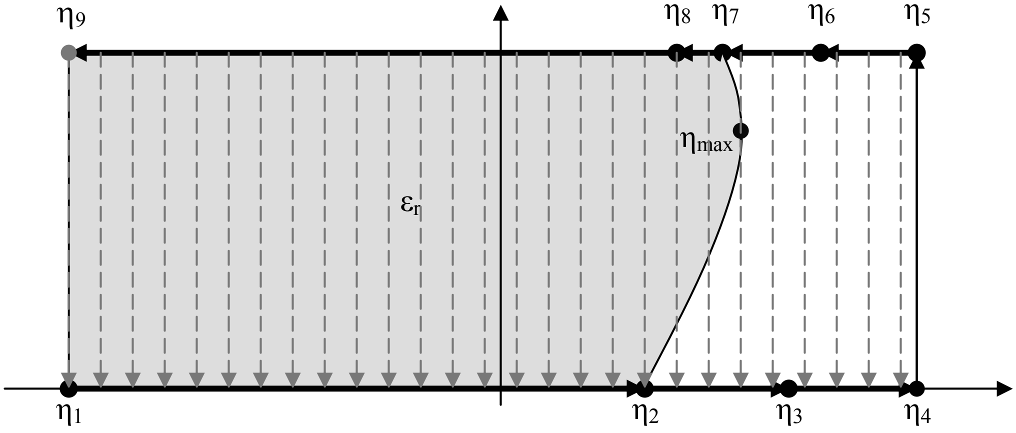

Figure 6.10. Schematic for direction-maintained approximation for the capacitance calculation (→ shows the electrical field direction).

2) Inductance

The per-unit-length inductance (L) is evaluated based on C_0 by the conventional expression [71]

$$L_0 = \frac{1}{c^2 C_0}$$

3) Conductance

If the dielectric-air interface is assumed to be a straight line which, located at $\eta = \eta_{eff,x}$, is perpendicular to the metal edge of the rectangle plane, the per-unit-length conductance (G) can be calculated using the following equation:

$$G = -\varepsilon_r \tan \delta \varepsilon_0 \omega \frac{\left|\eta_{eff,x} - \eta_{1,x}\right|}{\left|\eta_{5,y} - \eta_{4,y}\right|}$$

(Equation 6.3)

The interface position, $\eta_{eff,x}$, is defined by this equation:

$$C = 2\varepsilon_0 \left[\varepsilon_r \frac{|\eta_{eff,x} - \eta_{1,x}|}{|\eta_{5,y} - \eta_{4,y}|} + \frac{|\eta_{4,x} - \eta_{eff,x}|}{|\eta_{5,y} - \eta_{4,y}|} \right] \quad ,$$

(Equation 6.4)

which means that the "re-distribution" of the dielectric does not change the capacitance value. Since the interface itself has a tendency to be a vertical straight line (see Figure 6.9), and the dielectric loss (due to non-zero G) plays only a minor role compared to that of the conduct loss in the transmission lines with dimensions in this case, the error caused by the straight-line assumption will not have a great influence on the final results.

4) Resistance

The incremental inductance rule is used to calculate the per-unit-length resistance (R) as below[74]:

$$R(f) = \omega \left[L_{\frac{\delta(f)}{2}} - L \right] = \frac{\omega}{c^2} \left[\frac{1}{C_{0,\frac{\delta(f)}{2}}} - \frac{1}{C_0} \right] \quad ,$$

(Equation 6.5)

where $L_{\delta(f)/2}$ and $C_{0,\delta(f)/2}$ are the per-unit-length inductance and the per-unit-length capacitance respectively without the presence of the dielectrics, when the conductor surface recedes by $\delta(f)/2$ in the physical domain; $\delta(f) = 1/\sqrt{\pi f \mu_0 \sigma}$ is the frequency-dependent skin-effect current penetration depth; σ is the metal conductivity, and its value is $4.1 \times 10^7 S/m$. $C_{0,\delta(f)/2}$ and C_0 are both calculated using the direction-maintained approximation method.

The CM approach presented in the previous several paragraphs has been validated through comparison with the results of the FW-FEM method. The results of these two approaches are compared in Figure 6.11, in which Subfigures (a), (b), (c), and (d) give the impedance magnitudes, the impedance phases, the attenuation constants, and the effective refractive indexes respectively. Here, the FW-FEM results were obtained using the Ansoft high-frequency structure simulator (HFSS) which is a software package coded by the Ansoft Corporation for calculating the electromagnetic behavior of a structure. The characteristic impedance in the FW-FEM method is calculated from the values of power (P) and current (I) by $Z = P/(I \bullet I^*)$ [75]. The power and current are computed directly from the simulated fields. The power passing through a port is equal to $P = \iint_s (\vec{E} \times \vec{H}^*) ds$, where the surface integration is over the whole port. The current is calculated by applying the Ampere's law to a path around the port as follows: $I = \oint_l \vec{H} \bullet d\vec{l}$. Rectangles with side length greater than 4 times the sum of the central electrode width (w) and twice the ground electrode separation (s) are used as the ports in the FW-FEM simulation. Although there is some discrepancy between the solutions of these two approaches at low frequency, due to the inaccuracy of quasi-static approximation when the frequency is low, still, generally speaking, the solutions actually agree quite well, especially at high frequencies. The solutions of the CM approach and the FW-FEM approach for different electrode geometric dimensions and for different non-geometric parameters, such as the dielectric constant and metal conductivity, are also compared. These comparisons show that the CM approach can accurately evaluate the characteristic parameters for electrodes with a CPWG structure.

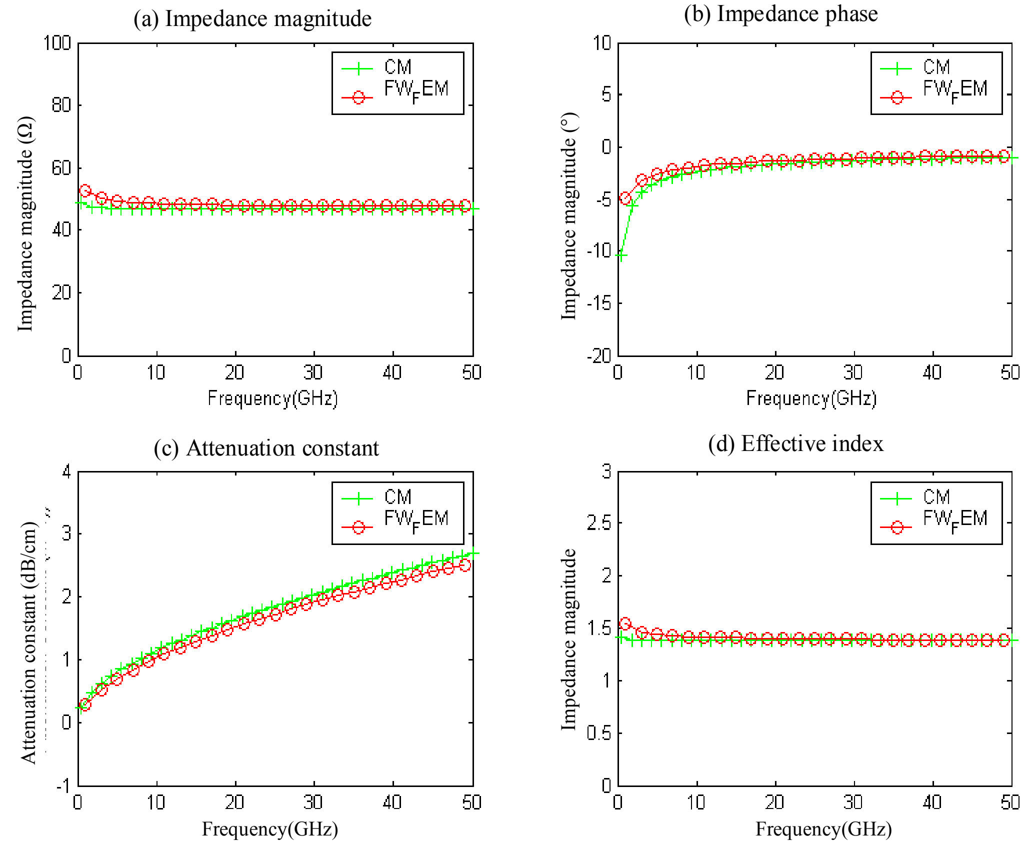

Figure 6.11. Comparison between the characteristic parameters of a CPWG (w = 23 μm; s = 14 μm; h = 8.5 μm; $t_g = t_a = 5$ μm; $\varepsilon_r = 2.40$; tanδ = 0.005; $\beta_a = \beta_g = 0°$) computed with FW-FEM and the present CM approach, respectively, as a function of frequency.

Due to its geometric transformation nature, this CM approach has great computational efficiency; meanwhile, its numerical method nature (the conformal mapping is numerically solved) enables it to evaluate symmetric CPWG electrodes with almost arbitrary 2-dimensional geometry (any 2-dimensional geometry can be infinitely approached by a polygon). These properties make this approach an excellent one for the optimization process.

6.3.2 Geometry optimization

In this section, we intend to find the optimal electrode geometry in terms of modulation bandwidth and electrode efficiency. The electrode efficiency refers to the ability of the traveling-wave electrode to generate an effective electrical field that can modulate the optical signal. Electrode efficiency directly relates to modulation depth. The means for evaluating bandwidth and electrode efficiency are discussed below.

The bandwidth is estimated using small-signal analysis. For a small microwave signal, the modulated optical output of a Y-fed directional-coupler-based modulator can be expressed as [62]

$$\begin{aligned}\Delta I(\omega) = k_m\{&[\sin 2\delta L(\Phi_c(\xi_+)+\Phi_c(\xi_-)) - \cos 2\delta L(\Phi_s(\xi_+)-\Phi_s(\xi_-))]^2 \\ &+[\sin 2\delta L(\Phi_s(\xi_+)+\Phi_s(\xi_-)) - \cos 2\delta L(\Phi_c(\xi_-)-\Phi_c(\xi_+))]^2\}^{\frac{1}{2}}\end{aligned},$$

(Equation 6.6)

where

$$\begin{aligned}&\Phi_s(\zeta) = \int_0^L e^{-\alpha(f)x}\sin\zeta x dx \\ &\Phi_c(\zeta) = \int_0^L e^{-\alpha(f)x}\cos\zeta x dx \\ &\xi_+ = \xi + 2\delta \\ &\xi_- = \xi - 2\delta \\ &\xi = \frac{2\pi f}{c}\left[n_m(f) - n_o\right] \\ &\delta = (\beta_s - \beta_a)/2\end{aligned}$$

and L is the interactive length; f is the frequency; $\alpha(f)$ is the attenuation constant; $n_m(f)$ is the microwave refractive index; n_o is the optical refractive index; β_s, β_a are the propagation constants of the symmetric and asymmetric optical modes in the interaction region respectively; k_m is a constant proportional to the applied modulation signal and the EO coefficient. Since $\alpha(f)$ and $n_m(f)$ can be evaluated using the CM approach, a frequency $f_{1/2}$ can be easily found at which the output optical intensity is only half of that when the frequency is zero. An excellent 3-dB bandwidth indicator is $f_{1/2}$, and it is used to optimize the electrode geometry. In this paper, we assume that the 3-dB bandwidth simply equals $f_{1/2}$, and $f_{1/2}$ is obtained by numerically solving the equation $I(f_{1/2}) = 0.5I(0)$ based on $\alpha(f)$ and $n_m(f)$ being evaluated using the CM approach described in Section 6.3.1. In bandwidth calculation, we set L = 1.0 cm, and $\delta = 1/(\sqrt{2}\pi L)$, which corresponds to the fact that the conversion length equals $\sqrt{2}$ times the interaction length.

To accurately evaluate the electrode efficiency, the details of the interaction between the optical signal and the applied electrical field should be considered. This interaction is usually most complex both because of the complexity of the interactive mechanism and because of the complexity of the spatial distribution of the optical and the electrical signals. As a simpler approximation, for a vertically poled EO polymer-based directional coupler modulator, the optical intensity change is assumed to be proportional to the difference between the vertical components of the electrical fields applied to the two optical waveguides. This field difference, denoted in this paper by E_{diff}, is used to optimize the electrode geometry.

In this paper, E_{diff} is evaluated by calculating the difference between the average vertical field along the segments AB and CD. As shown in Figure 6.7, AB and CD are simply two straight-line segments that are parallel to the bottom electrode and vertically located at the center of the UDP layer. Their ends A, B, C, and D are horizontally aligned to the rib edges of the two optical waveguides respectively. Assuming that the images of AB and CD in the rectangle plane are curves $\eta_A\eta_B$ and $\eta_C\eta_D$ respectively, as shown in Figure 6.9(b), E_{diff} can be derived as

$$E_{dff} = \frac{U}{(\eta_{5,y} - \eta_{4,y})}\left[\frac{\eta_{D,x} - \eta_{C,x}}{|CD|} - \frac{\eta_{B,x} - \eta_{A,x}}{|AB|}\right] = \frac{\sqrt{2P|Z|^2 / Z_r}}{(\eta_{5,y} - \eta_{4,y})}\left[\frac{\eta_{D,x} - \eta_{C,x}}{|CD|} - \frac{\eta_{B,x} - \eta_{A,x}}{|AB|}\right],$$

(Equation 6.7)

where P is the power flow along the transmission line, U is the voltage between the center and ground electrodes, Z is the per-unit-length impedance, Z_r is the real component of Z, and |AB| and |CD| are the lengths of segments AB and CD respectively in the physical domain.

There is another factor, the position of the electrodes relative to the optical waveguides, which can also affect electrode efficiency. This factor is accounted for simply by horizontally sweeping the electrodes to search for the best position where the maximum electrode efficiency can be achieved. This relative position is represented by a variable called O_{fst}, as shown in Figure 6.7; this variable is the horizontal displacement of the left side of the right waveguide relative to the left side of the central electrode. When O_{fst} is in the same direction as the arrow in Figure 6.7, it is considered positive; otherwise, it is negative. All the electrical field differences (E_{diff}) given in this section are calculated at the point ($O_{fst} = O_{fst\_best}$), where E_{diff} has the largest value.

The center electrode width (*w*) and the top electrode separation (*s*) are the two most important parameters which can be adjusted to satisfy the design criteria. Their influences on the characteristic parameters, bandwidth, etc., are shown in Figure 6.12 and Figure 6.13, where the horizontal coordinator is *w* and the vertical coordinator is *s*. Figures 6.12(a) and (b) show the magnitude of the impedance and the effective refractive index respectively, and Figure 6.12(c) shows the attenuation constant. Figure 6.13(a) shows the bandwidth ($f_{1/2}$), and Figure 6.13(b) gives the value of the electrode's relative position (O_{fst_best}), where the largest electrical field difference (E_{diff}) can be achieved. Figure 6.13(c) and Figure 6.13(d) show the corresponding values of E_{diff} (evaluated as $O_{fst} = O_{fst\_best}$) for constant input power (P=0.01 W) and for constant applied voltage (U=1V) respectively. The parameters used in the calculations are given in the figures. These results show that a large bandwidth can be achieved by using electrodes with a large center electrode width and a large separation because large w and s can not only reduce loss, but also increase the effective refractive index. To obtain the best electrode efficiency for constant microwave power, the electrode separation should be slightly smaller than the corresponding optical waveguides separation. The electrode efficiency for constant applied voltage can be improved by using electrodes with small separations. When the separation is larger than about 20μm, the influence of the two top ground electrodes begins to disappear, and the electrode efficiency drops. It appears that a negative O_{fst} is necessary to achieve the best electrode efficiency.

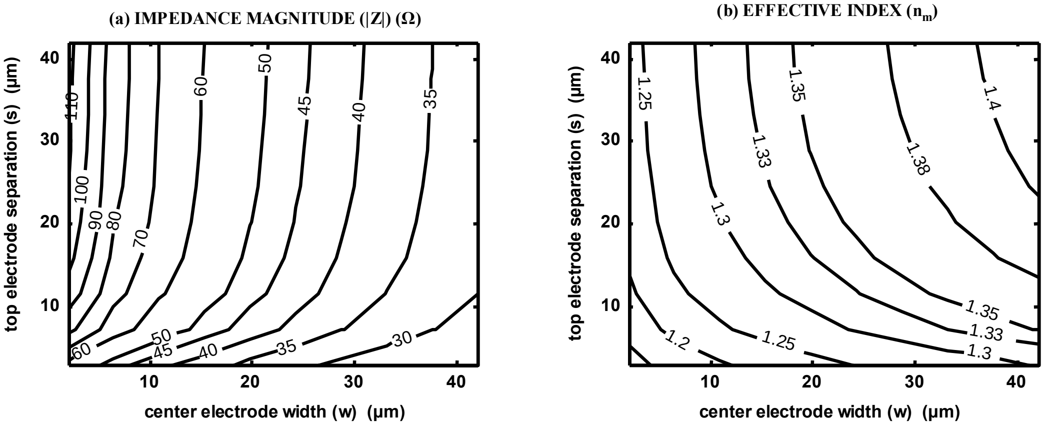
(a) IMPEDANCE MAGNITUDE (|Z|) (Ω)

(b) EFFECTIVE INDEX (n_m)

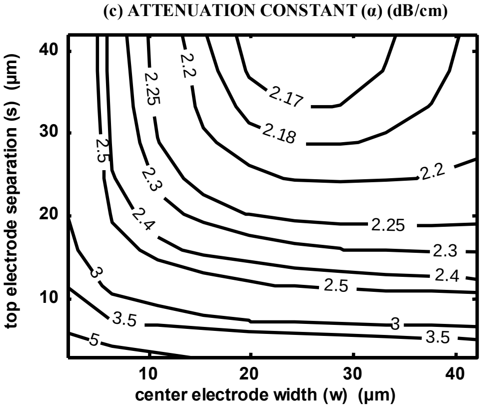
(c) ATTENUATION CONSTANT (α) (dB/cm)

Figure 6.12. Characteristic parameters of a CPWG (h = 8.5 μ m, ε r = 2.40, tan δ =0.005, f = 40 GHz, tg = ta = 5 μ m, β a = β g = 0°) as a function of the center electrode width (w) and the top electrode separation(s). (a) Impedance magnitude (|Z|); (b) Effective index (nm); (c) Attenuation constant (α).

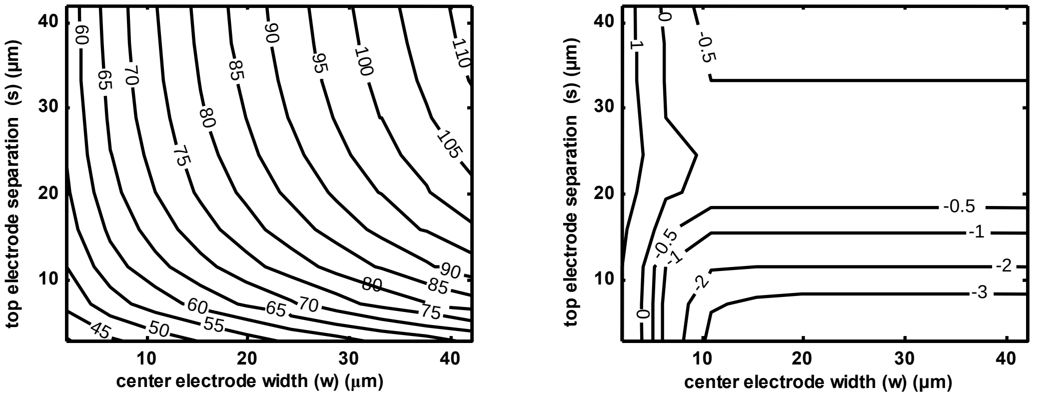

(a) BANDWIDTH ($f_{1/2}$) (GHz)

(b) OPTICAL WAVEGUIDES RELATIVE POSITIONS (O_{fst_best}) (μm)

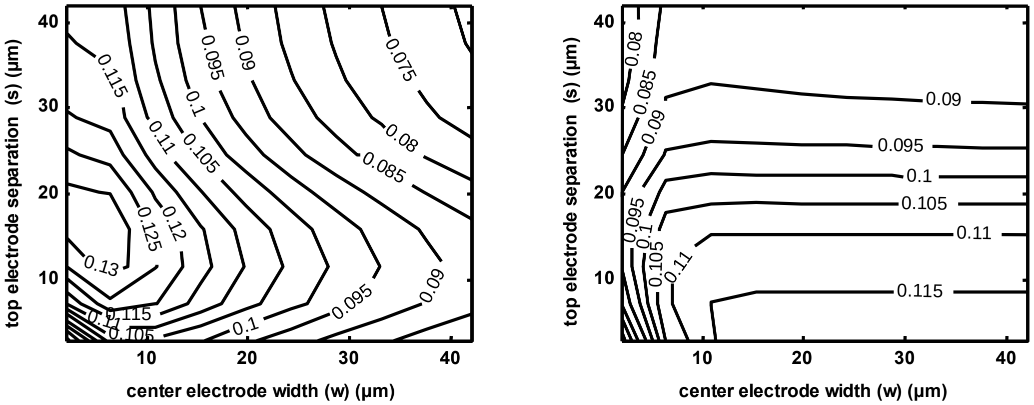

(c) FIELD DIFFERENCE FOR CONSTANT POWER (E_{diff}) (V/μm)

(d) FIELD DIFFERENCE FOR CONSTANT VOLTAGE (E_{diff}) (V/μm)

Figure 6.13. Bandwidth and electrode efficiency of a CPWG (h = 8.5 μm, ε_r=2.40, tanδ=0.005, f = 40 GHz, t_g = t_a = 5 μm, β_a = β_g =0°, s_o= 12 μm, w_o= 4μm, n_o=1.59) as a function of the center electrode width (w) and the top electrode separation (s). (a) Bandwidth ($f_{1/2}$). (b) Optical waveguide relative position (O_{fst_best}). (c) Field difference (E_{diff}) for constant applied microwave power (P=0.01W). (d) E_{diff} for constant applied voltage (U=1V).

The influence of the dielectric layer thickness is evaluated as follow: The dielectric thickness and the electrode separation are allowed to change within certain ranges. For each combination of the values of these two parameters, a value, w_{50}, of the center electrode width is sought with which the impedance match ($\left|Z\right|=50\Omega$) can be achieved. Then w_{50} is used to evaluate the $f_{1/2}$ and the E_{diff}. Figure 6.14 shows the contour maps of $f_{1/2}$, E_{diff}, w_{50}, and the corresponding O_{fst_best}. Since the impedance is a constant here, the E_{diff} for constant input power and the E_{diff} for constant voltage are the same. Based on these results, high electrode efficiency can always be obtained by reducing the polymer layer thickness, while a reduced dielectric thickness can result in small bandwidth. However, when the electrode separation is smaller than about 15μm, the influence of the dielectric thickness on the bandwidth becomes quite small under the impedance match condition. (In this paper, the impedance match condition means $\left|Z\right|=50\Omega$, which is achieved by adjusting the value of the center electrode width when the values of all other parameters are specified.) The reason for this phenomenon may be that, when separation is small, the capacitance between the center electrode and the top ground electrodes is dominant over the capacitance between the center electrode and the bottom ground electrode.

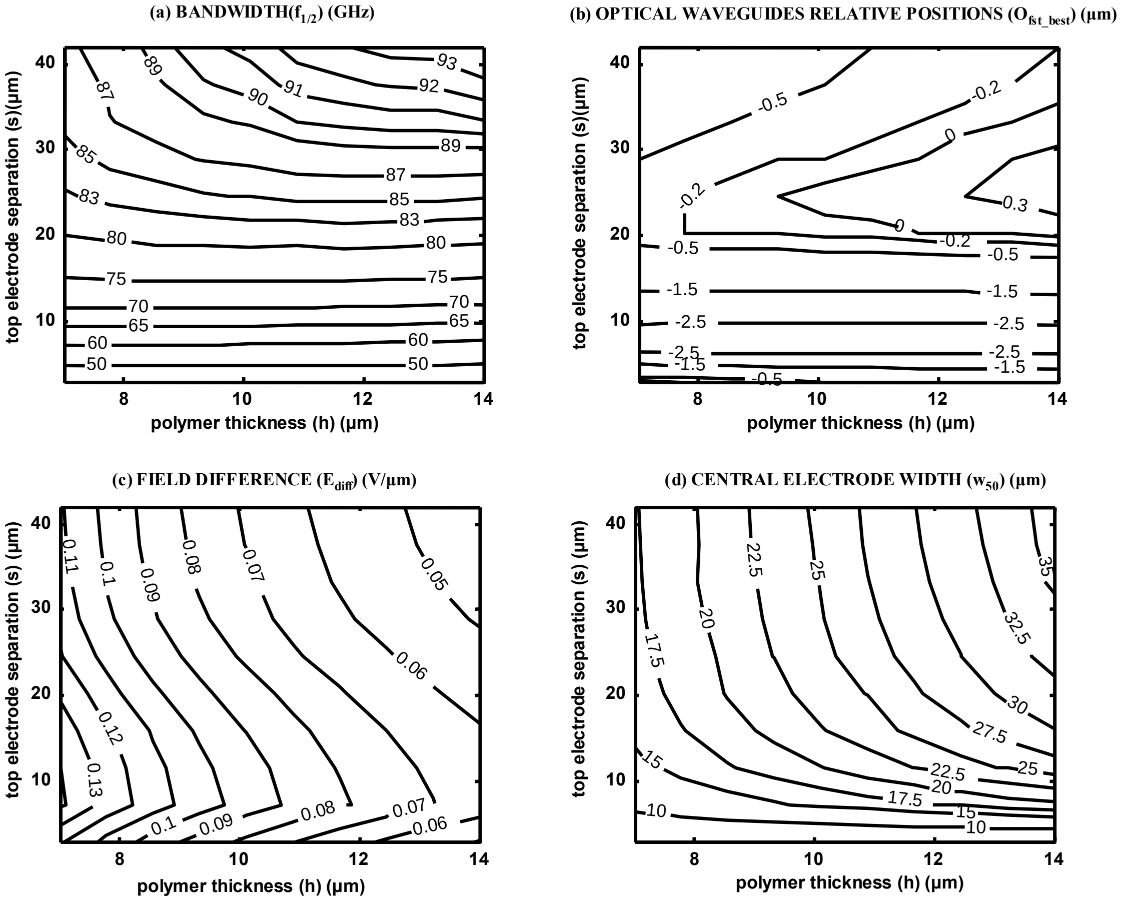

Figure 6.14. Bandwidth and electrode efficiency of a CPWG ($\varepsilon_r = 2.40$, $\tan\delta = 0.005$, $f = 40$ GHz, $t_g = t_a = 5$ µm, $\beta_a = \beta_g = 0°$, $s_o = 12$ µm, $w_o = 4$ µm, $n_o = 1.59$) as a function of the polymer thickness (h) and the top electrode separation (s). (a) Bandwidth ($f_{1/2}$). (b) Optical waveguides relative position (O_{fst_best}). (c) Field difference (E_{diff}) for constant applied voltage (U=1V). (d) Center electrode width (w_{50}) in order to achieve impedance match ($|Z|=50\Omega$).

The influences of the optical waveguide separation and of the dielectric constant are evaluated using the same method as that used to evaluate the dielectric thickness, and the results are shown in Figure 6.15 and 6.16 respectively (only contour maps of the bandwidth and the E_{diff} are given). It can be observed that the dielectric constant can greatly affect bandwidth, while it has only small influence on the electrode efficiency under the impedance match condition, especially when the top electrode separation is greater than 6-7 μm. Satisfactory electrode efficiency can be obtained by using a large optical waveguide separation, while at the same time the optical waveguide separation does not affect bandwidth. Both Figure 6.15(b), and Figure 6.14(b) show that, under the impedance match condition, there is one best value for the electrode separation with which the largest E_{diff} can be obtained, and this value does not change appreciably with the changes in the dielectric layer thickness and in the optical waveguide separation. The best value for electrode separation in these simulations is in the 7-8 μm range.

The influence of the trapezoidal angle is evaluated in a similar manner. It was found that the trapezoidal angles have only minor effect on the driving voltage and bandwidth. Electrodes with a small negative trapezoidal angle have the lowest loss; however, a positive trapezoidal angle can increase the effective refractive index so that the bandwidth in increased.

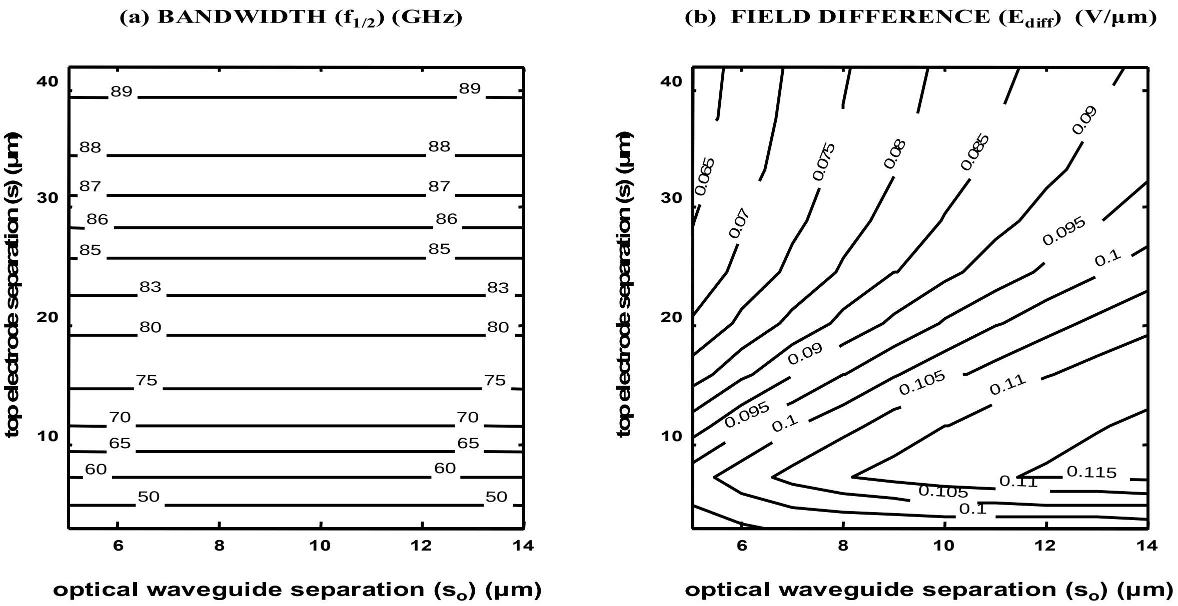
(a) BANDWIDTH ($f_{1/2}$) (GHz)

(b) FIELD DIFFERENCE (E_{diff}) (V/µm)

Figure 6.15. Bandwidth and electrode efficiency of a CPWG (h = 8.5 µm, $\varepsilon_r = 2.40$, tanδ = 0.005, f = 40 GHz, $t_g = t_a = 5$ µm, $\beta_a = \beta_g = 0°$, $w_o = 4$ µm, $n_o = 1.59$) as a function of the optical waveguide separation (s_o) and the top electrode separation (s). (a) Bandwidth ($f_{1/2}$). (b) Field difference (E_{diff}) for constant applied voltage (U=1V).

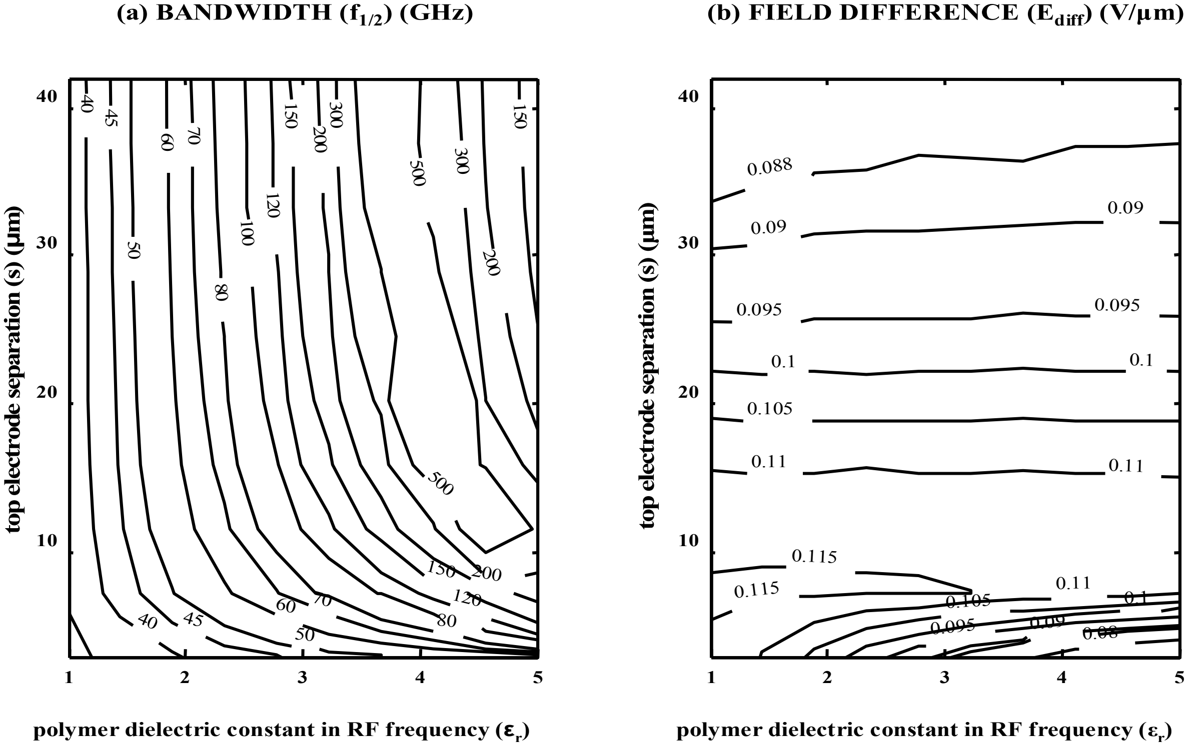

Figure 6.16. Bandwidth and electrode efficiency of a CPWG ($h = 8.5$ μm, $\tan\delta = 0.005$, $f = 40$ GHz, $t_g = t_a = 5$ μm, $\beta_a = \beta_g = 0°$, $s_o = 12$ μm, $w_o = 4$ μm, $n_o = 1.59$) as a function of the polymer dielectric constant (ε_r) and the top electrode separation (s). (a) Bandwidth ($f_{1/2}$). (b) Field difference (E_{diff}) for constant applied voltage (U=1V).

6.3.3 Conclusion

The CPWG was chosen as the structure of the traveling-wave electrodes for a directional-coupler-based polymeric EO modulator. A characteristic-parameter-determination approach is presented, which, based on the conformal mapping solution of the Schwarz-Christoffel (SC) toolbox of MATLAB, can give an approximate evaluation of all the characteristic parameters for a CPWG with an arbitrary symmetric polygon geometry. The results given from this approach agree closely with the FW-FEM results obtained using the Ansoft HFSS. A method to evaluate bandwidth and electrode efficiency is also given and is used to optimize the electrode geometry.

The optimization results may be summarized as follows: (1) There is a trade-off between the bandwidth and the electrode efficiency; the modulation bandwidth can be enlarged by using an electrode with a relatively large center electrode width and a large electrode separation, while small electrodes can improve the electrode efficiency. (2) A large optical waveguide separation can improve the electrode efficiency, meanwhile not affecting the bandwidth. (3) A thin dielectric layer can greatly increase the electrode efficiency. Under the impedance match condition, its influence on the bandwidth is small when the top electrode separation is small. (4) The electrode separation value, with which the largest electrode efficiency can be obtained, is almost independent of the corresponding optical waveguide separation, and of the polymer layer thickness under the impedance match condition. The best electrode separation value is around 6-8 μm for typical modulator dimensions. (5) The influence of the trapezoidal angle is small, and an electrode with a small negative trapezoidal angle has the lowest loss.

6.4 TAPER REGIONS AND TEST STRUCTURES

To apply RF signals to the TW electrode, an RF connecter or an RF probe must be connected to the end of the electrode. The electrodes are usually too small to be connected directly, thus taper regions are usually needed to increase the lateral dimensions of the electrodes. The taper region designed here is illustrated in Figure 6.17. A V-shaped opening was first etched in the bottom electrode, and then the width of the active electrode and the separation of the top electrodes were increased gradually along the propagation direction. All the dimensions, which are carefully calculated to satisfy the 50-Ω-impedance requirement, are given on Table 6.3. Note that the taper regions for the CPWGs listed on Table 6.4 are basically the same as each other except in their small ends, where they are adapted to the sizes of the electrodes to which they connect.

Table 6.3 Dimensions of the Electrode Taper Regions

Distance ***z*** (×10μm)	0	97	127	152	177	202	227	252	277	302	327	352	277	450
Active electrode width ***w*** (μm)	*	120	150	175	200	225	250	275	300	325	350	375	400	400
Top electrode separation s_t (μm)	*	38	46	53	63	74	86	99	113	128	144	161	179	179
Bottom electrode separation s_b (μm)	*	190	242	281	326	373	422	473	526	581	638	697	758	758

* The size of the small end of the taper is adjusted according to the size of the electrode to which it connects.

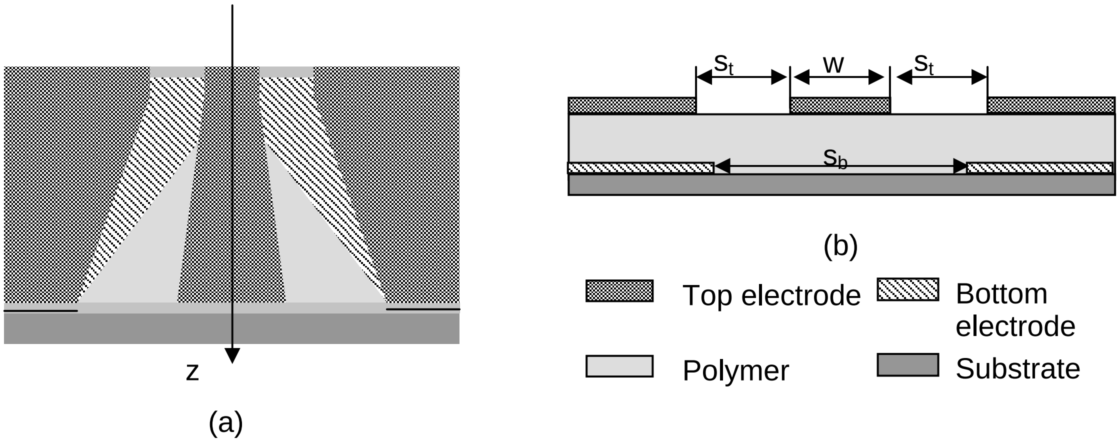

Figure 6.17. Schematic of the electrode taper regions: (a) Top view, (b) Cross-section (S_t: top electrode separation; S_b: bottom electrode separation; W: center electrode width)

Due to the existence of the taper regions, we cannot de-embed the propagation constant of the electrode directly based the measured S parameters. The test structures were designed to fulfill this task. These structures are actually two electrode segments of different lengths (l_a and l_b), but with the same taper regions as shown in Figure 6.18. The transmission matrixes of the test structures M_a and M_b can be expressed as

$$\begin{aligned} M_a &= X\begin{bmatrix} e^{\gamma l_a} & 0 \\ 0 & e^{-\gamma l_a} \end{bmatrix} Y \\ M_b &= X\begin{bmatrix} e^{\gamma l_b} & 0 \\ 0 & e^{-\gamma l_b} \end{bmatrix} Y \end{aligned} ,$$

where X and Y refer to the transmission matrixes of the left and right tapers respectively, and γ is the complex propagation constant of the electrode. After simple manipulation, we can derive

$$M_a M_b^{-1} = X\begin{bmatrix} e^{\gamma (l_a - l_b)} & 0 \\ 0 & e^{-\gamma (l_a - l_b)} \end{bmatrix} X^{-1} \quad .$$

The above equation shows that $e^{\gamma (l_a - l_b)}$ and $e^{-\gamma (l_a - l_b)}$ are the two eigenvalues of matrix $M_a M_b^{-1}$, thus, γ can be easily calculated based on M_a and M_b. The values of M_a and M_b can be obtained using the following equations based on the corresponding scattering matrix S:

$$\begin{aligned} M_{11} &= \frac{(1+S_{11})(1-S_{22})+S_{12}S_{21}}{2S_{21}} \\ M_{12} &= \frac{(1+S_{11})(1+S_{22})-S_{12}S_{21}}{2S_{21}} \\ M_{21} &= \frac{(1-S_{11})(1-S_{22})-S_{12}S_{21}}{2S_{21}} \\ M_{22} &= \frac{(1-S_{11})(1+S_{22})+S_{12}S_{21}}{2S_{21}} \end{aligned} ,$$

where S_{ij} and M_{ij} (i=1,2, j=1,2) are the four elements of the S and M matrixes respectively. S can be directly measured by employing a Network analyzer. In our design, l_a = 2.5 cm, and l_b =1.0 cm.

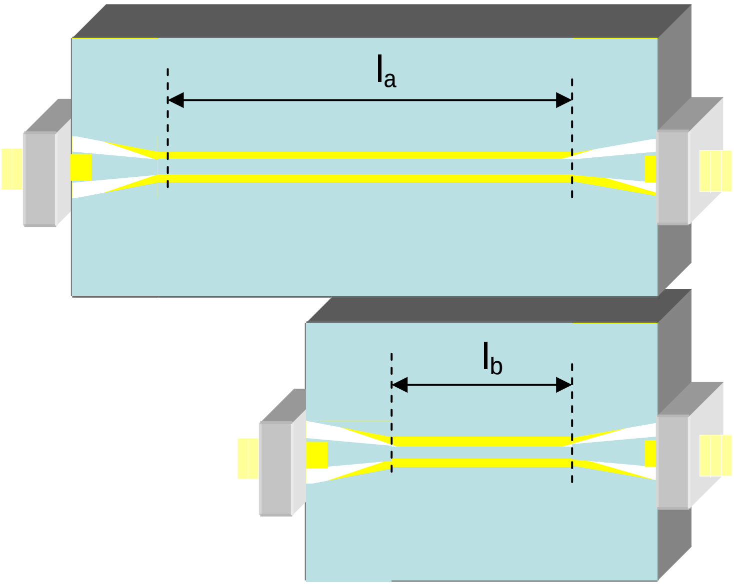

Figure 6.18. Electrode Test Structures with RF Connectors

6.5 ELECTRODE FABRICATION AND TESTING

The test structures for the CPWG electrode listed on Table 6.4 were fabricated and tested. The characteristics of these CPWGs were de-embedded based on the test results.

The bottom electrode was 50Å Cr and 3 μm Au deposited by sputtering. The polymer layers were spin-coated as described in Chapter 3. A 50 Å Cr and 2000 Å Au were then deposited using e-beam to serve as the seed layer for electroplating. AZ4620P was applied and patterned to serve as the plating buffer. Then electrodes were electroplated to 3 μm with Au as shown in Figure 6.19. After the photoresist was removed, the seed layer was etched away finally. The chip was diced for testing.

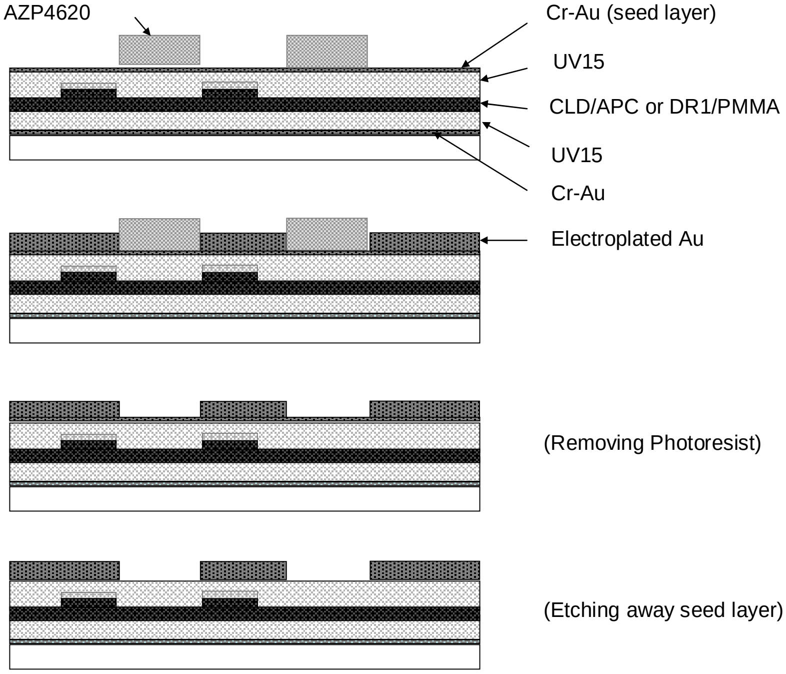

Figure 6.19. The traveling-wave electrode fabrication procedure

The Aritsu Universal Test Fixture (UTF) Model 3860V was used to connect the fabricated electrodes to a HP8510C Network Analyzer which are employed to test the electrodes. Figures 6.20(a) and (b) show the schematic and a photo of the test set-up respectively. A chip (with an electrode test structure) mounted in the UTF3860V is shown in Figure 6.20(c).

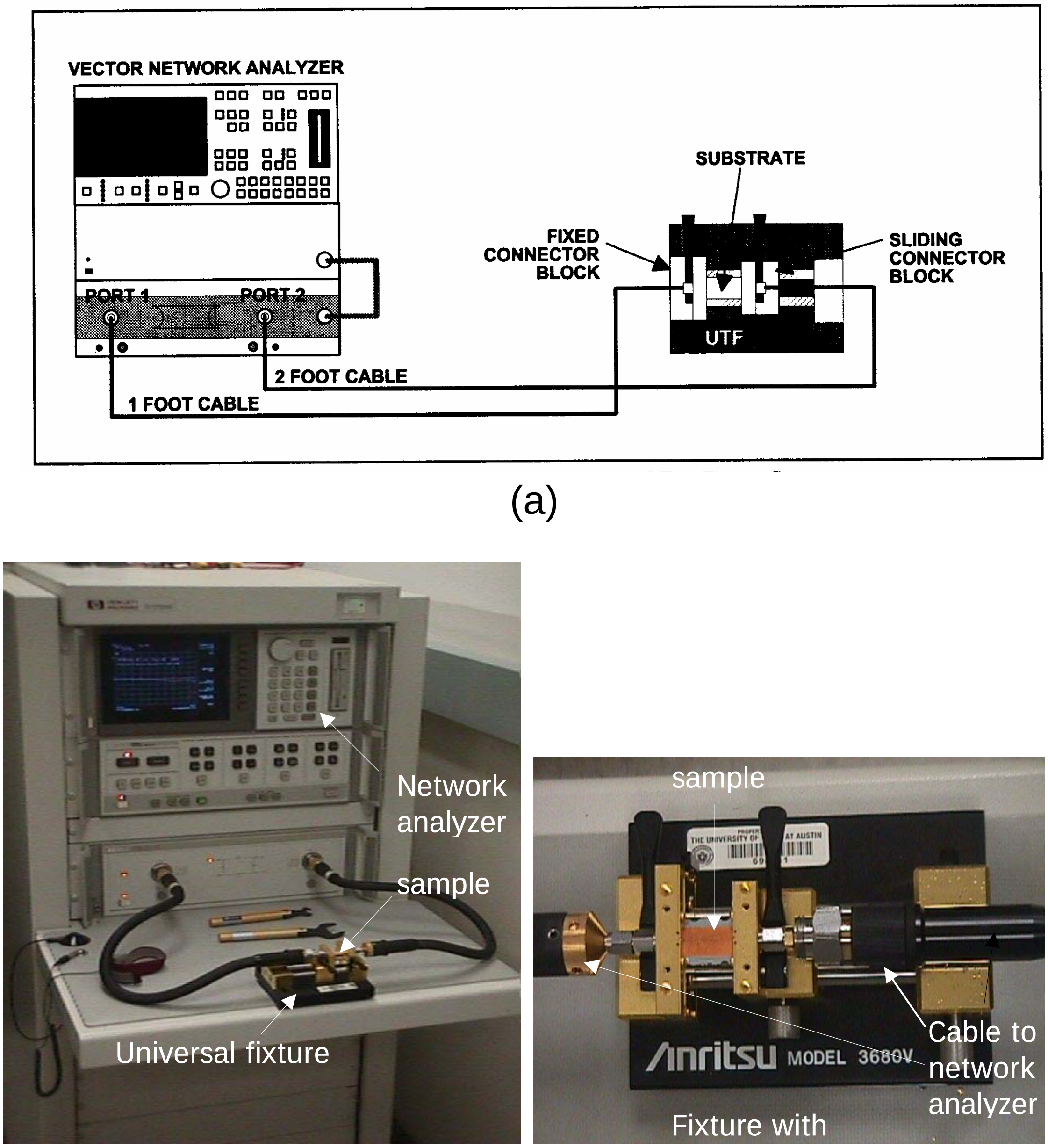

(a)

(b)

(c)

Figure 6.20. Electrode test set-up: (a) schematic, (b) photo of the whole set-up and (c) photo of test fixture and tested sample

Figure 6.21 shows a typical test result of S_{11}, $S_{12,}$ and the Smith chart of a test structure with a 1-cm electrode. The return is smaller than 20 dB from DC to 50

GHz. Figure 6.22 shows the de-embedded electrode losses and effective index vs. frequency of two CPWGs. The dimensions of these two CPWGs are listed on Table 6.4. The frequency-square-root dependence of their loss indicates the domination of conductor loss over dielectric loss. This qualitative conclusion agrees with the simulation results in Sections 6.2 and 6.3. The measured electrode properties are listed on Table 6.4. The electrical effective indexes agree well with the simulation results given in Table 6.2. However, the losses are much larger than the simulated results. The large loss is likely due to the roughness of the plated electrode surface.

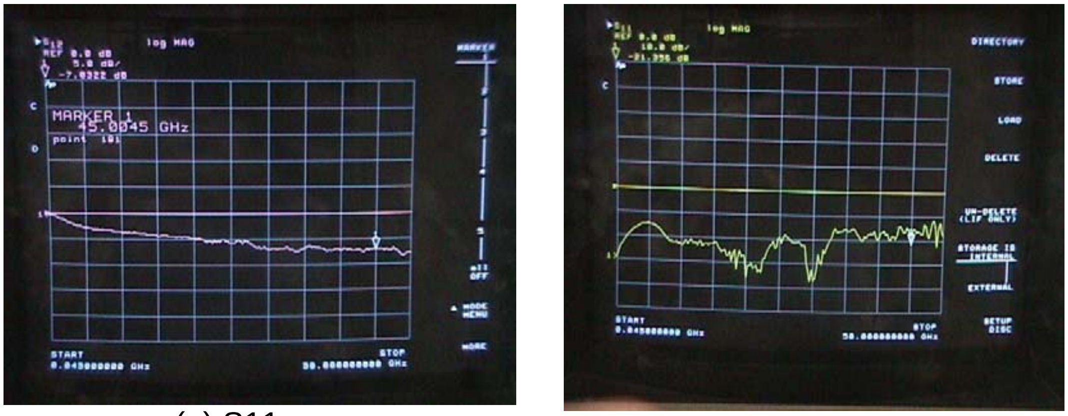

(a) S11

(b) S12

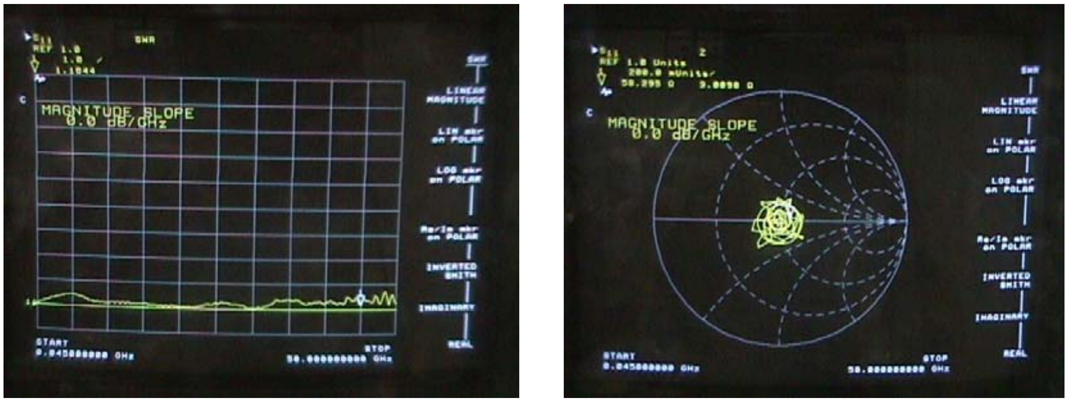

(c) SWR

(d) Smith chart

Figure 6.21. Test results of the test structure with 1-cm electrode length

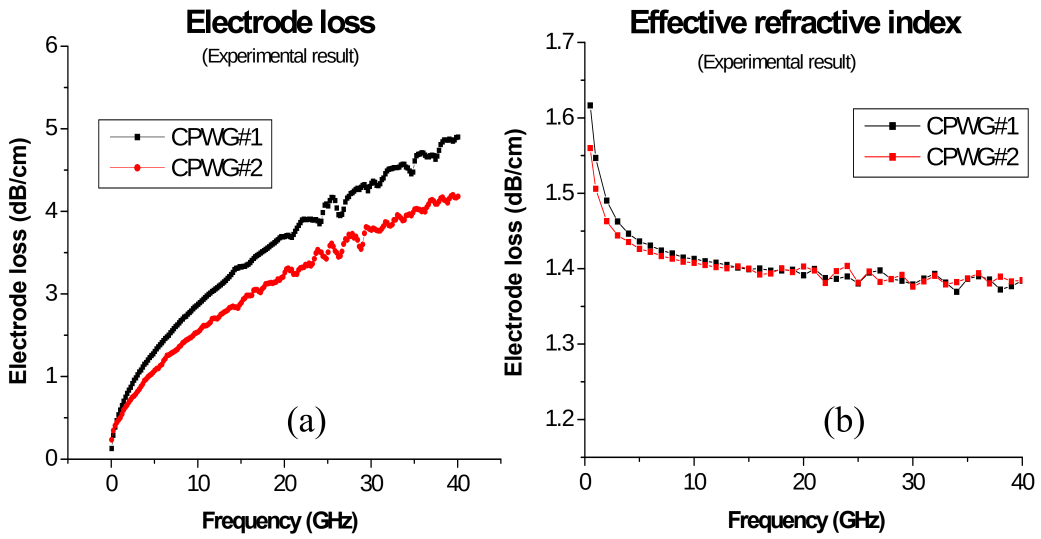

Figure 6.22. Electrode measurement results: (a) electrode losses and (b) the effective refractive indices

Table 6.4 De-embedded electrode properties

Electrode structure	**Polymer thickness (μm)**	**Top electrode thickness (μm)**	**Bottom electrode thickness (μm)**	**Active electrode width (μm)**	**Electrode gap (μm)**	**Effective Index**	**Conductor loss** $\left(dB/cm/\sqrt{GHz}\right)$	**Dielectric** $\left(dB/cm/\sqrt{GHz}\right)$
CPWG#2	12	3	3	31	12	1.38	0.65	0.012
CPWG#1	8.5	3	3	21	8	1.40	0.80	0.012

6.6 SUMMARY

To find the optimal driving voltage and bandwidth for electro-optic polymer-waveguide-based directional couplers, four electrode structures: MSL, ACWG, CPWG, and CMSL are investigated. The CPWG and the ACWG have almost the same driving voltages which are about 2 times of the driving voltage of the CMSL. The MSL has the largest driving voltage that is 20%-25% higher than the diving voltages of the CPWG and the ACWG. The MSL has the largest bandwidth and its bandwidth is about 1.6 time of the bandwidth of the CMSL which has the narrowest bandwidth. The bandwidths of the ACWG and the CPWG are 1.4 times and 1.2 times of that of the CMSL, respectively. The driving voltages for the four different devices are experimentally confirmed by using UV15:PMMA/DR1:UV11-3 based directional couplers. Taking into account the capability of a CPWG to achieve $\Delta\beta$ inversion, the CPWG is the choice of design for this research. A conformal-mapping approach to the optimum TW electrode design of a coplanar waveguide with ground (CPWG) was developed and employed to optimize the electrode dimensions. Taper regions were designed to increase the lateral dimensions of the electrodes to accommodate RF connecters or RF probes. Test structures were designed to de-embed the electrodes' characteristics. Two CPWGs with their test structures were fabricated and tested.

Chapter 7 High-Speed EO Modulators Based on Polymeric Y-fed Directional Couplers

7.1. INTRODUCTION

The performance of current commercially available EO intensity modulators is adversely affected by the distortions caused by the nonlinearity of the modulation curve which typically exhibits sine-squared behavior. Furthermore, the direct-current (*dc*) biases, required in order to bring these modulator to their best working points, result in more complicated circuit fabrications. As discussed in the previous chapters, these problems can be alleviated or even be avoided by employing carefully designed Y-fed directional couplers.

In this chapter (Section 7.3), we will demonstrate an intrinsic-3dB-biased high-speed EO modulator based on a Y-fed directional coupler employing the UV15:CLD1/APC:UV11-3 waveguide described in Chapter 3 and the traveling-wave electrode set forth in Chapter 6. Without a *dc* bias, this modulator gave a performance similar to that of a quadrature-biased high-speed MZ modulator. This attractive property comes from the fact that the Y-fed directional coupler is intrinsically biased in the best point of its transfer curve.

As discussed in Chapter 4, carefully designed two-section Y-fed directional couplers are promising for fabricating high-linear EO modulators, which are themselves superior to other currently developed high-linear-modulation techniques in their ultra-simple device structure and their ultra-simple driving requirements, i.e., not needing *dc* bias voltages and optical or electrical power splits. These couplers' excellent capability in suppressing distortions has been explored theoretically under the uniform-$\Delta\beta$-in-each-section assumption, and demonstrated experimentally, at low operation frequencies, using a polymeric modulator with a lumped electrode (Chapter 4). However, a high-linear modulator's major applications such as the CATV, antenna remoting, need them to operate in the RF or even microwave frequencies. For applications higher than 1 GHz, traveling-wave electrode structures are mandatory in order to overcome the limitations resulting from inter-electrode capacitance and finite transit time. Due to propagation loss in the electrical modulation signal, and to the velocity mismatch between the electrical and optical signals, the modulation-induced $\Delta\beta$ is not uniform along the waveguides of a modulator working at high frequencies. Therefore, the uniform $\Delta\beta$ assumption made in Chapter 4 and Reference 11 is not applicable for high-speed modulators. For two-section directional couplers, the situation is even more complex since the impacts of the velocity mismatch and the electrical propagation loss are different for the 'upstream' section and for the 'downstream' section. All these factors cause a high-speed directional coupler to perform differently than its low-speed counterpart does. However, based on our knowledge, there is no systematic analysis of two-section polymeric directional couplers in terms of high linear modulation, and high-linear EO modulator based on a two-section polymeric Y-fed directional coupler has not yet been demonstrated. In the following Section, 7.2, we will first investigate two-section Y-fed directional couplers with emphasis on their high-linear modulation capability. Then, Sections 7.3 and 7.4 describe the design, fabrication and test of two high-speed EO modulators based on a one-section Y-fed directional coupler and a two-section Y-fed directional coupler, respectively, employing the UV15:CLD1/APC:UV11-3 waveguides whose design is outlined in Chapter 3 and the traveling-wave electrodes dealt with in Chapter 6.

7.2. HIGH-SPEED PROPERTIES OF Y-FED DIRECTIONAL COUPLERS

In this Section, our exploration is focused on the transfer curve linearity. Other high-speed properties of Y-fed directional couplers can be found elsewhere.

7.2.1. Simulation method

When calculating the output optical intensity of a high-speed modulator, both the space and time dependency of the modulation voltage need to be taken into consideration. Thus, the complex amplitudes of the optical signals in the two channels R and S and the modulation-induced propagation constant change, Δβ, are now functions of *z* (the coordinate along the optical waveguide) and *t* (time), i.e., R(z, t), S(z, t) and Δβ(z, t). Based on the coupler theory, the following equation can be obtained:

$$\begin{cases} \lim\limits_{\Delta x\to 0}\dfrac{R[z+\Delta z,t+\frac{n_0}{c}(z+\Delta z)]-R(z,t+\frac{n_o}{c}z)}{\Delta z}=j\dfrac{\Delta\beta(z,t+\frac{n_o}{c}z)}{2}R(z,t+\frac{n_o}{c}z)-j\dfrac{\pi}{2l}S(z,t+\frac{n_o}{c}z) \\ \lim\limits_{\Delta x\to 0}\dfrac{S[z+\Delta z,t+\frac{n_o}{c}(z+\Delta z)]-R(z,t+\frac{n_o}{c}z)}{\Delta z}=-j\dfrac{\Delta\beta(z,t+\frac{n_o}{c}z)}{2}S(z,t+\frac{n_o}{c}z)-j\dfrac{\pi}{2l}R(z,t+\frac{n_o}{c}z) \end{cases}$$

(Equation 7.1)

where n_o is the refractive index of the optical signal, *c* is free-space light speed and *l* is coupling length. Given Δβ(z, t) and the initial values of S(0, t) and R(0, t), the output complex amplitudes at the end of the interaction section with a length of L, S(L, t+n_oL/c*)* and R(L, t+n_oL/c) can be calculated using Equation 7.1. A reasonable result can seen that the optical signal S(0, t) that entered the interactive section at moment *t* comes out from the interaction section at t+n_oL/c. The elapsed time, n_oL/c, is exactly the time needed for the optical signal to travel through the interactive section. For modulators employing the linear EO effect, Δβ is proportional to the modulation voltage. Under a two-tone modulation signal with frequencies f1 and f2,

$$\Delta\beta(z,t+\frac{n_o}{c}z)=\beta_1\exp[-\alpha(f_1)z]\cos\left[2\pi f_1 t+\phi_1+2\pi\frac{\{n_o-n_e\}f_1}{c}z\right]+$$
$$\beta_2\exp[-\alpha(f_2)z]\cos\left[2\pi f_2 t+\phi_2+2\pi\frac{\{n_o-n_e\}f_2}{c}z\right] \quad ,$$

(Equation 7.2)

where n_e is the electrical refractive index of the traveling-wave electrode, β_1 (β_2), $\alpha(f_1)$ ($\alpha(f_2)$), and ϕ_1 (ϕ_2) are the amplitude, microwave attenuation constant, and initial phase, respectively, of the signal with frequency f_1 (f_2). Here, n_m is assumed to be a constant. For two section directional couplers, the sign of Δβ is assumed to change instantly at the interface of the two sections, and the outputs of the first section serve as the input of the second section.

A program was coded to calculate the output signal by solving Equation 7.1. The two-tone electrical test signal drives the modulator. The Fourier transform of the output was evaluated to find the fundamental and distortion components. In the calculation, the parameters of the UV15:CLD1/APC:UV11-3 waveguide whose design is laid out in Chapter 3 and the 8-µm-separation CPWG electrode whose fabrication is reported in Chapter 6 are used to set the values of n_e, n_o and α, i.e., $n_e = 1.40$, $n_o = 1.58$, $\alpha(f) = 0.80 \times 5\ln(10) \times \sqrt{f/10^9}\, m^{-1}/\sqrt{GHz}$ for polymeric modulators. Sometimes the corresponding properties of a LiNbO$_3$-based directional coupler were also evaluated as a comparison. In the LiNbO$_3$ modulator, α was assumed to have the same value as that of the polymeric modulator, n_e and n_o were assumed to be 4.0 and 2.2, respectively, typical values for LiNbO$_3$ modulators. The values of β_1 and β_2 are determined by the target modulation depth. For Y-fed directional couplers, $S(0,t) \equiv R(0,t) \equiv 1/\sqrt{2}$.

7.2.2. Linear properties at high operation frequencies

The nonlinear distortion suppression (DS), as defined in Chapter 5, of several Y-fed directional couplers are shown in Figure 7.1: IYCM1(s1 = 2.17530, s2 = 1.14640), IYCM2(s1 = 2.86057, s2 = 2.86057), IYCM3(s1 = 2.12870, s2 = 3.09290), IYCM4(s1 = 2.86050, s2 = 0.0) and NYCM(s1 = 0.70711, s2 = 0.0). These are shown as a function of operation frequency. Here, s1 and s2 are the normalized interaction lengths of the first and second sections respectively. In Figure 7.1, the DS of the corresponding Mach-Zehnder modulator (MZM) are also given as a comparison. The low-speed properties of these modulators are listed on Table 5.1. In Figures 7.1(a) and (b), the modulators are assumed to be built with polymers and $LiNbO_3$ respectively. Figure 7.1(c) shows the corresponding results of polymeric modulators with lossless traveling-wave electrodes. As expected, these results indicate the decay of DS as the frequency increases. However, it is still possible to build broadband high-linear modulators by employing well-designed Y-fed directional couplers. Their linearity degradations show quite different characteristics between each other. Based on their degradation characteristics, these modulators can be divided into three categories. The first category includes MZMs and NYCMs, whose distortion suppressions do not change or change very low with frequencies. The MZM's DS is independent of frequency due to the identical decays of the fundamental and distortion signals. The NYCMs show similar behavior to that of the MZMs except for the $LiNbO_3$-based NYCM at frequencies larger than 10 GHz. The second category includes the IYCM1 and IYCM3, whose DSs are linearly dependent on logarithm of frequency, implying an exponential dependence on frequency. The

IYCM2 and IYCM4 belong to the third category. They behave similarly to the second category modulators at lower frequency but have deep DS drops at higher frequencies. The effect of electrode loss can be estimated by comparing Figures 7.1(a) and 7.1(c). The loss seems to have relative larger influence on the DS at low frequency. This linearity degradation is much more extreme in $LiNbO_3$-based modulators. In this regard, EO polymers show an advantage over $LiNbO_3$ because of the small dispersion in their refractive indexes at microwave and at optical frequencies. Among these modulators, IYCM2 has the best linearity performance. The DS of the polymeric IYCM2, as shown in Figure 7.1 (a), is at least 20 dB larger than that of the MZM in the whole range between *dc* and up to 20GHz.

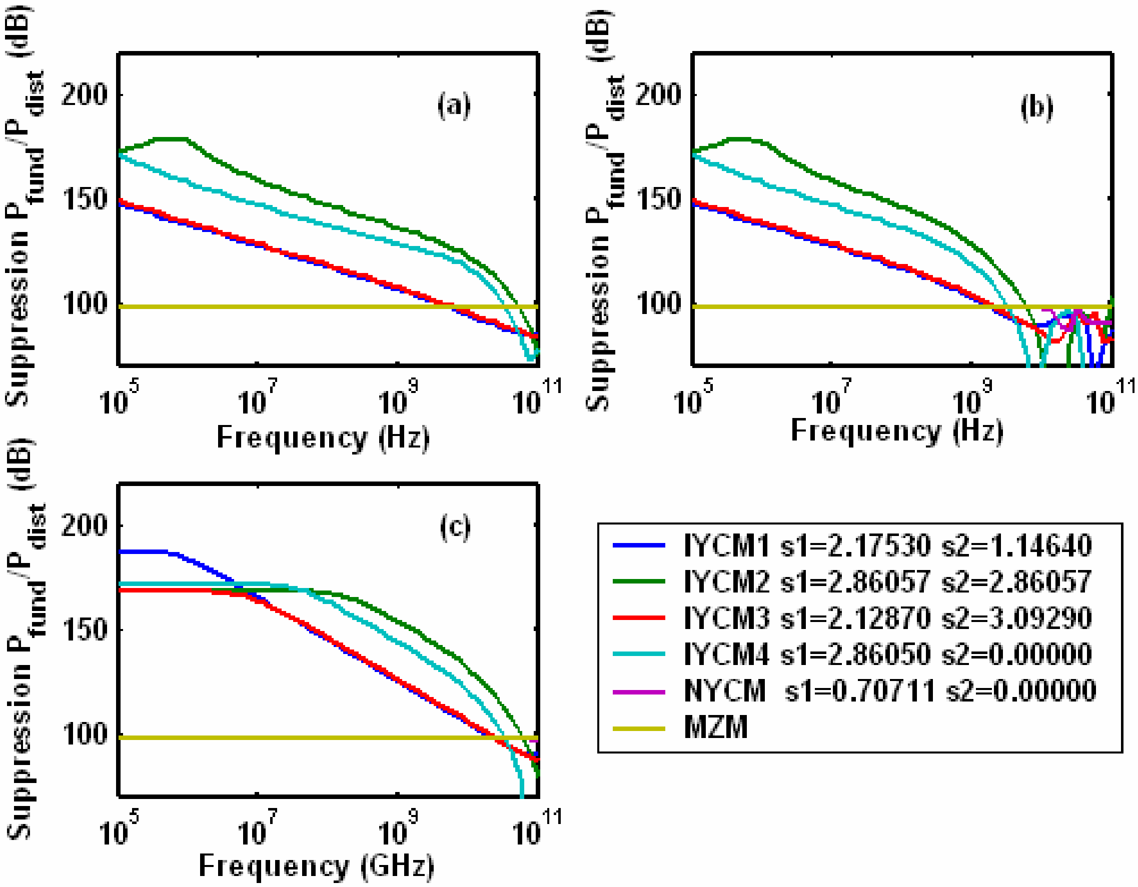

Figure 7.1. Simulated distortion suppressions vs. frequency of an MZM and directional couplers with different normalized intersection lengths as indicated in the legend: (a) n_o=1.58, n_e=1.40, α=0.80dB/cm/$\sqrt{GHz}$, and L=1.0cm; (b) n_o=2.2, n_e=4.0, α=0.80dB/cm/ $\sqrt{GHz}$ and L=1.0cm; (c) n_o=1.58, n_e=1.4, α=0, and L=1.0cm

7.2.3. Interaction length

The interaction length is more critical for high-speed directional couplers than for low-speed. In a high-speed directional coupler, the interaction length affects its performance not only through the ratio between the interaction length and the coupling length, as it does in a low speed directional coupler, but also through the velocity mismatch and electrode loss. The impacts of velocity mismatch and electrode loss are larger for longer interaction length. Figure 7.2 shows DS versus interaction length of the modulators that are discussed in the previous Section. Now their operation frequency is fixed at 10 GHz. It is obvious that the linearity of polymeric Y-fed directional couplers degrades as their interaction length increases and it decays fast in higher operation frequencies. Once again, the EO polymer shows advantages over $LiNbO_3$ since it is almost impossible to build a $LiNbO_3$-based Y-fed direction coupler which has larger DS at 10GHz than that of an MZM. Our design of choice is 1-cm interaction length.

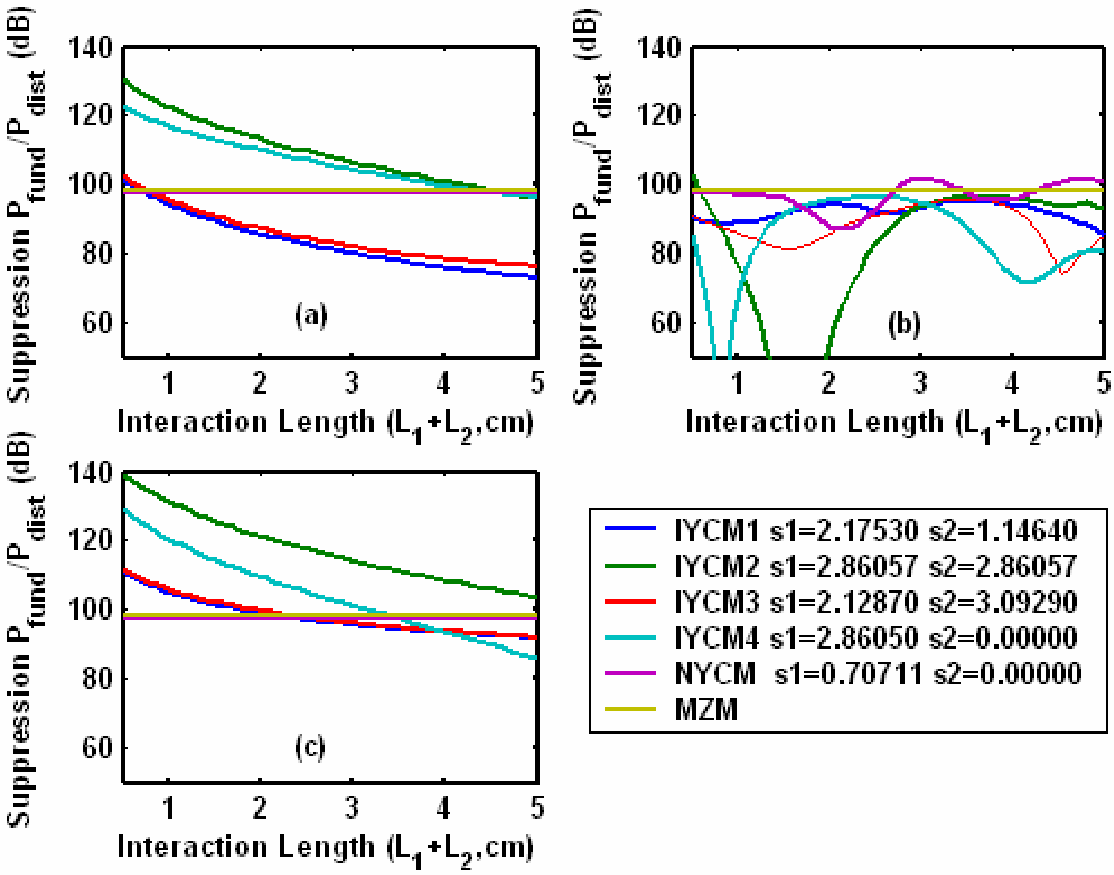

Figure 7.2. Simulated distortion suppressions vs. interaction length of the MZ modulator and directional couplers with different normalized intersection lengths as indicated in the legend: (a) n_o=1.58, n_e=1.40, α=0.80dB/cm/$\sqrt{GHz}$, and f=10GHz; (b) n_o=2.2, n_e=4.0, α=0.80dB/cm/$\sqrt{GHz}$, and f=10GHz; (c) n_o=1.58, n_e=1.4, α=0 and f=10GHz

7.2.4. Driving voltage and modulation depth

The driving voltages, maximum modulation depths, and DS values of the above-mentioned modulators with 1-cm interaction length and 10 GHz operation frequency are listed on Table 7.1. The DS values are calculated at 1% modulation depth. The driving voltages, which were calculated using the same method as that on

Table 5.1, are normalized to the value of the driving voltage of the NYCM at direct current. Comparing the results on Tables 5.1 and 7.1, besides the DS decreases, we can also observe a 10%-20% increase in the driving voltages at 10 GHz. However, the maximum modulation depths remain approximately the same.

Table 7.1 Modulation depth and driving voltage

Modulator	IYCM1	IYCM2	IYCM3	IYCM4	NYCM	MZM
Type	DC	DC	DC	DC	DC	MZ
Normalized 1st Section length:S_1	2.17530	2.86057	2.12870	2.86050	0.70711	__
Normalized 2nd Section length:S_2	1.14640	2.86057	3.09290	0.00000	0.00000	__
Interaction length (cm)	1.00	1.00	1.00	1.00	1.00	1.00
Optical refractive index (n_o)	1.58	1.58	1.58	1.58	1.58	1.58
Electrical refractive index (n_e)	1.40	1.40	1.40	1.40	1.40	1.40
Electrode loss (dB/cm/sqrt(fGHz))	0.80	0.80	0.80	0.80	0.80	0.80
Frequency (GHz)	10	10	10	10	10	10
Distortion suppression* (DS) (dB)	94	122	96	116	98	98
Normalized Driving Voltage **	4.38	4.41	6.99	3.99	1.13	0.72
Maximum Modulation Depth	0.98	0.97	0.84	0.72	1.00	1.00

* The distortion suppressions are calculated at 1% modulation depth

** The driving voltages are normalized to the driving voltage of the NYCM at direct current

Based on the simulation results in this Section, the IYCM2 has the best performance in terms of distortion suppression. A polymeric IYCM2 with 1.0-cm interaction length has DS at least 20 dB larger than that of an MZM from *dc* up to 20 GHz. The polymeric NYCM with 1-cm interaction length has performance similar to that of an MZM, but it does not need a *dc* bias. In the following two Sections, we will demonstrate an IYCM2 and an NYCM using polymers.

7.3. A HIGH-SPEED BIAS-FREE EO MODULATOR BASED ON A POLYMERIC Y-FED DIRECTIONAL COUPLER

A high-speed NYCM was fabricated by integrating the UV15:CLD1/APC:UV11-3 waveguide discussed in Chapter 3 and the 8-µm-separation CPWG traveling-wave electrodes put forth in Chapter 6. A schematic of the fabricated NYCM is illustrated in Figure 7.3(a), and a picture of the actual device is shown in Figure 7.5(b). The fabrication and poling procedures are described in Chapters 2, 3, and 6. In this modulator, the separation between the two optical waveguides is 10µm, and the top-electrode separation is 8µm. The left edge of the right optical waveguide is located 1µm to the right corresponding to the left edge of the active electrode. The rib depth was fine-tuned to achieve a normalized interaction length close to $1/\sqrt{2}$.

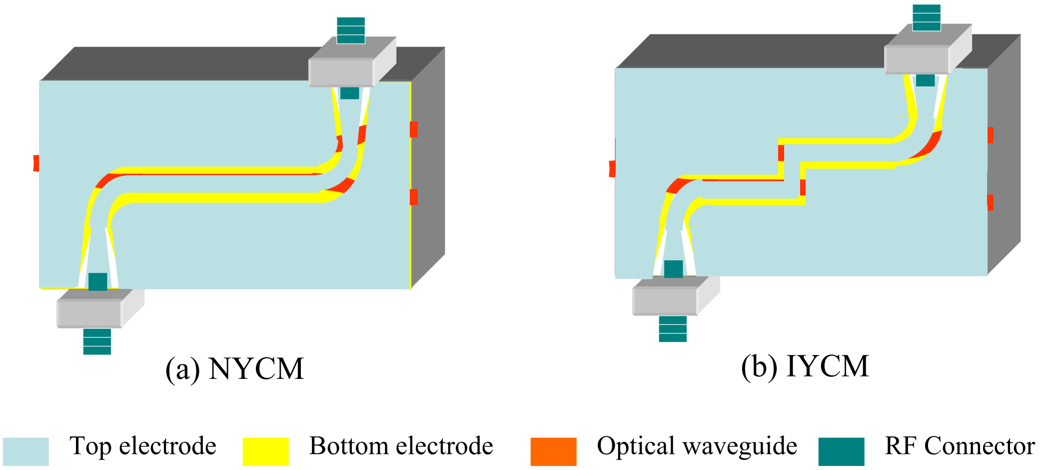
(a) NYCM

(b) IYCM

Figure 7.3. Schematics of the bias-free high-speed EO modulator based on a polymeric normal Y-fed directional coupler (NYCM) and the broad-band high-linear EO modulator based on a Δß-inverted polymeric Y-fed directional coupler (IYCM)

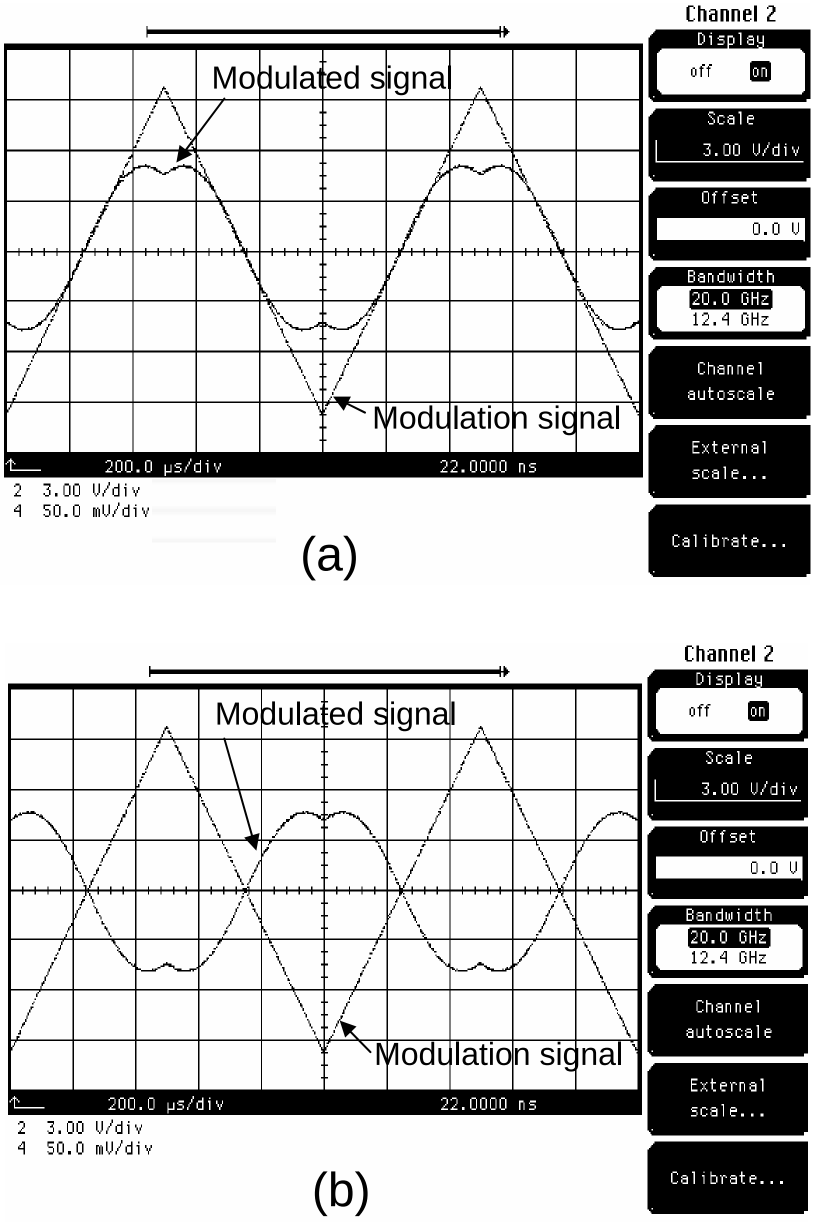

Scale 3.00 V/div
Offset 0.0 V
Bandwidth 20.0 GHz 12.4 GHz
200.0 µs/div 22.0000 ns
2 3.00 V/div
4 50.0 mV/div

Figure 7.4. Measured modulation and modulated signals of the NYCM: (a) upper branch; (b) lower branch

The fabricated NYCM was tested at 1.55 µm using a Santec ECL-200 laser. The input polarization-maintained (PM) single-mode (SM) fiber was aligned to the waveguide, and the output was collected by an output fiber and guided to a photodetector. A fiber-optical polarization controller was used between the laser and the modulator to adjust the input polarization to TM. The total insertion loss was around 17dB.

The switch voltage at low speed, V_s, is measured by applying a 1KHz signal. The output signals were detected by an AAA detector and monitored by an oscilloscope. The modulation and the modulated signals are shown in Figure 7.4, in which the triangle signal is the modulation signal (electrical) and the other curve with more curvatures is the modulated signal (optical). The horizontal axis is the time axis (200 μsec per division), and the vertical direction shows the voltage for the modulation signal (3V per division) and shows the optical intensity for the modulated signal. This test result indicates a 14V switch voltage.

The set-up for high-speed testing is illustrated in Figure 7.5. A picture of the under-tested modulator is also given in the same figure. When we tested the small-signal frequency response, the RF signal provided by an HP83651B synthesized sweeper, which in turn was part of an HP8510C network analyzer system, was applied to the modulator directly. The output optical signals were boosted by an Erbium-doped fiber amplifier (EDFA) and were then detected by a Newport 1014 high-speed detector. The detected electrical signal from the detector was finally measured by an HP8563E Spectrum Analyzer. The measured frequency response of the NYCM is shown in Figure 7.6. This result shows that a more than 20GHz 3dB bandwidth has been achieved.

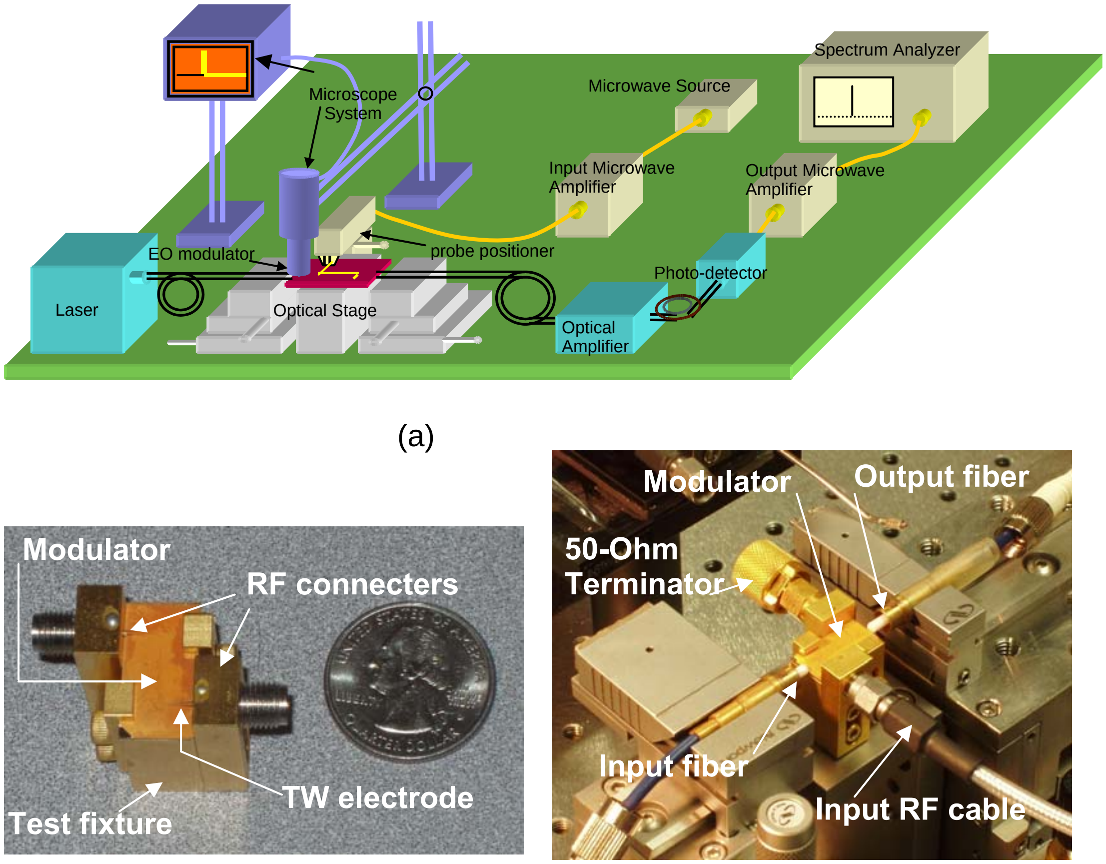

(a)

(b)

(c)

Figure 7.5. Pictures of a fabricated high-speed modulator and schematic of the test set-up for frequency response: (a) set-up schematic, (b) a picture of the modulator, and (c) the modulator on the testing stage.

The nonlinear distortion of this NYCM was also tested. The test methods and results are described in Section 7.4. The test results show that the bias-free NYCM has a performance similar to that of a quatrature-biased MZM in terms of nonlinear distortion suppression. Although the NYCM has higher driving voltage than the corresponding MZM, it eliminates the need of the *dc* bias.

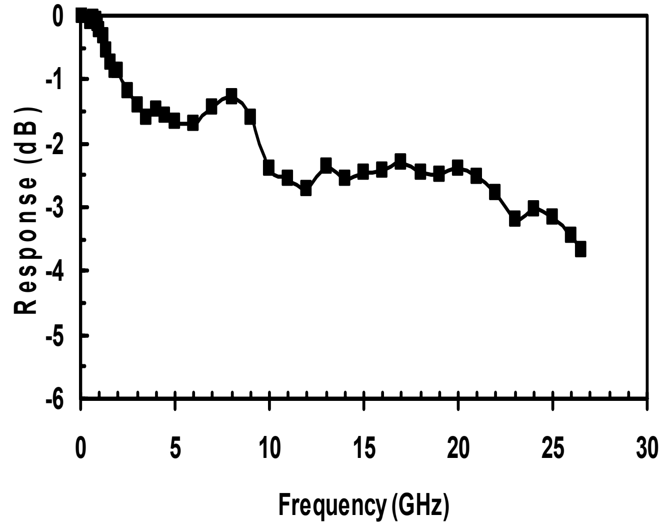

Figure 7.6. Measured frequency response of the NYCM.

7.4. A BROADBAND HIGH-LINEAR EO MODULATOR BASED ON A POLYMERIC Δβ-INVERTED Y-FED DIRECTIONAL COUPLER

An IYCM was fabricated by integrating a UV15:CLD1/APC:UV11-3 Y-fed directional coupler with an 8-μm separation CPWG electrode. This TW electrode is the same as the one used in the NYCM described in the previous Section except for an offset in the middle of the interaction section designed to achieve Δβ-inversion, as shown in Figure 7.3(b). The interaction length is 1 cm, and the optical waveguide separation is 6 μm. The left edge of the right waveguide is vertically aligned to the left edge of the active electrode. The rib depth is adjusted to attain a normalized interaction length of around 2.86.

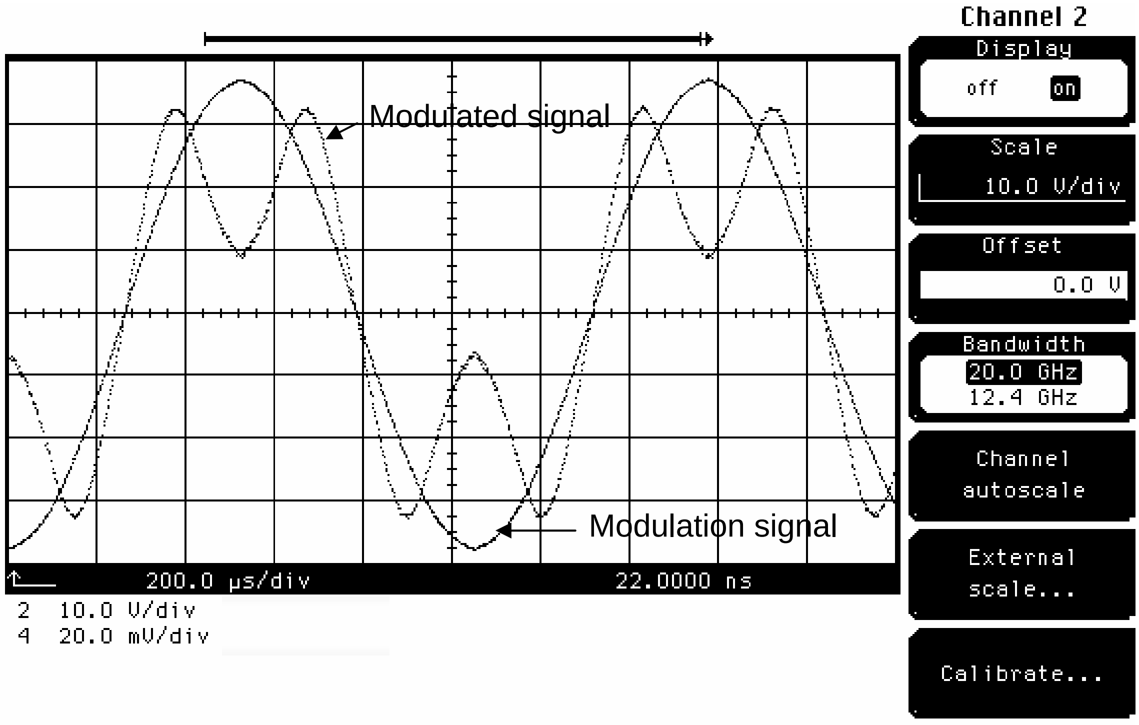

Figure 7.7. Measured modulation and modulated signals of the IYCM

The driving voltage and frequency response of the IYCM were tested using the same approach as that used in the NYCM test. Figure 7.7 shows the modulation and modulated signals. The horizontal axis is the time axis (200 µsec per division), and the vertical direction shows the voltage of the modulation signal (10V per division) and the optical intensity of the modulated signal. The switch voltage is around 46 V. Figure 7.8 gives the IYCM's frequency response, which, although with more fluctuations, has a similar tendency to that of the NYCM. A 20 GHz 3-dB bandwidth was achieved.

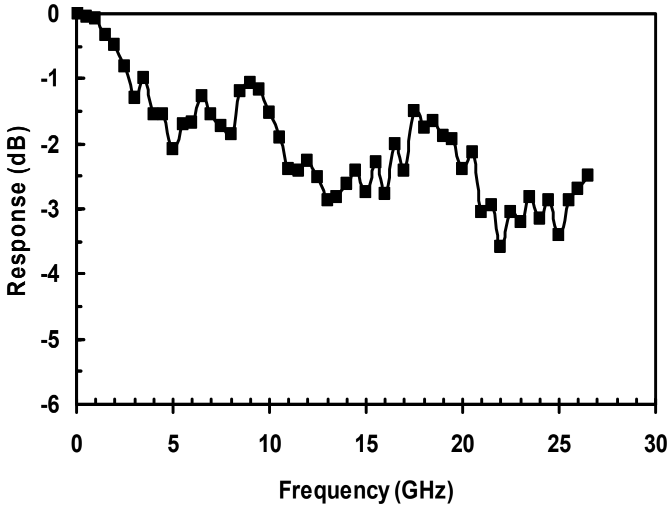

Figure 7.8. Measured frequency response of the IYCM.

The linearity properties of the IYCM were tested using the set-up schematized in Figure 7.9. An HP8620C sweep oscillator was used as the second RF source. Agilent 83020A and Agilent 8449B power amplifiers served as the RF pre-amplifier and RF post-amplifier respectively. Two RF signals with about 10% difference in frequency from each other were applied to the modulator to test its nonlinear distortion.

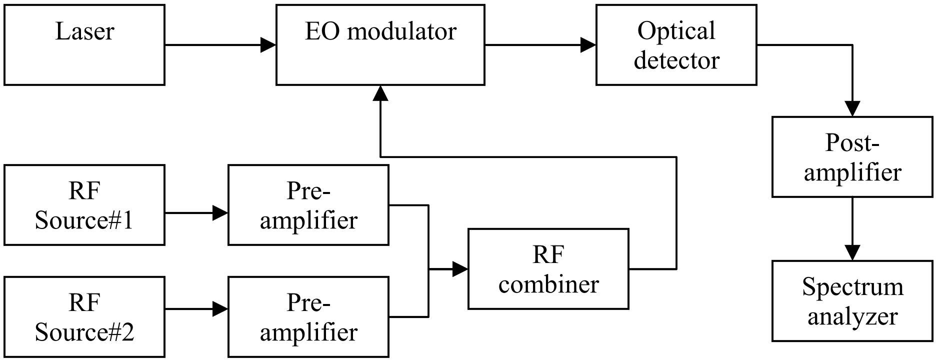

Figure 7.9. Schematic of test set-up for inter-modulation distortion (IMD)

The measured fundamental and distortion signals of the IYCM and the NYCM at 4GHz are given in Figure 7.10. The corresponding theoretical results of a quadrature-biased MZM are also drawn in the same figure as a comparison. It can be seen that the bias-free NYCM has a performance similar to that of an MZM in terms of distortion suppression. The IYCM has around 20 dB lower distortions than the corresponding MZM from 0.05 to 0.2 modulation depths. When testing the nonlinear distortion, we checked the intermodulation distortion (IMD) (third-order and fifth-order), and harmonic distortion (second-order and third-order) simultaneously; it was found that the third-order IMD always dominated in our measurements.

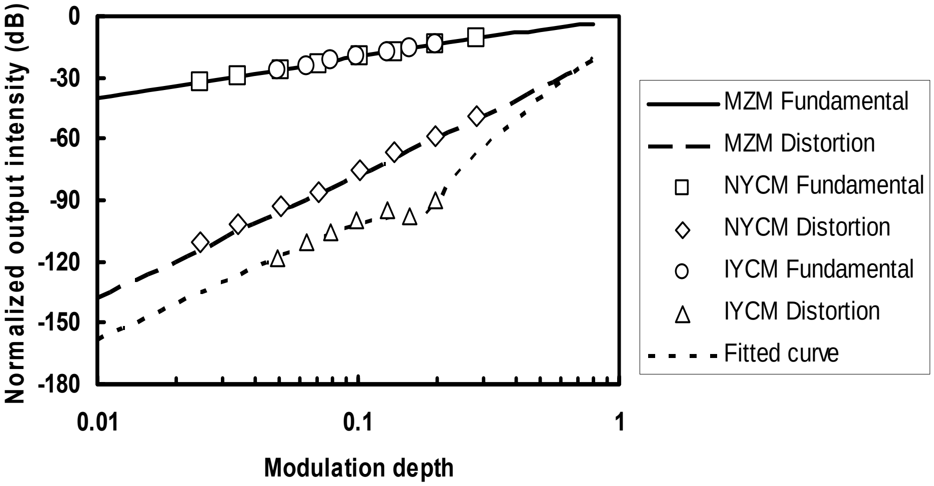

Figure 7.10. Measured fundamental and distortion signals of the NYCM and IYCM (the theoretical values of a quadrature-biased MZM are given as reference)

Figures 7.11(a), (b), (c) show the tested distortion suppressions vs. frequency for these two modulators at modulation depths of 0.2, 0.1, and 0.05 respectively. It can be observed that around 20 dB distortion suppression improvement was obtained in the whole range from 0 to 8 GHz. Although we did not test the distortion suppression at higher frequencies because of the limitations of our set-up, it is expected that this suppression improvement will continue for higher frequencies. In Figures 7.11(b) and (c), the suppression decreases as the frequency increases. But in Figure 7.11(a), the suppression increases as the frequency increases. This phenomenon may be caused by the dip structure of the suppression like that shown in Figure 7.10 between 0.1 and 0.2 modulation depths. It was found that the position of such dips changed as the frequency changed. Figure 7.11(d) shows the extrapolated results at 0.01 modulation depth. It can be observed that the IYCM has the potential to provide a 115-dB dynamic range up to 8 GHz at a modulation depth of around 0.01.

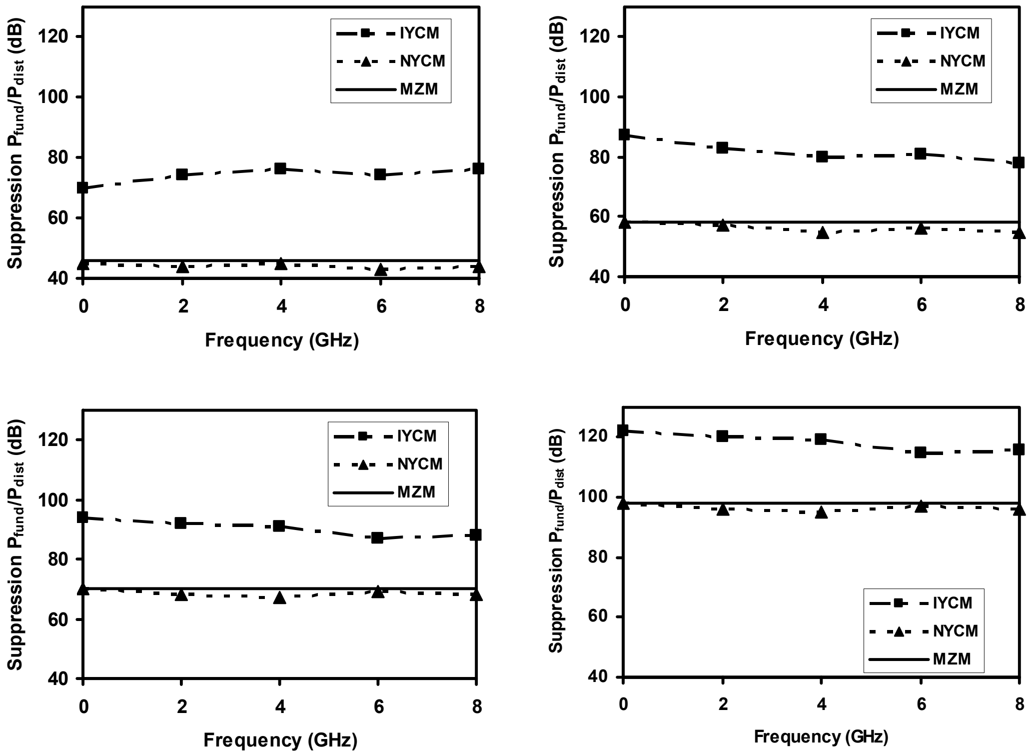

Figure 7.11. Measured distortion suppressions at different frequencies for the IYCM and the NYCM (The corresponding theoretical values of a quadrature-biased MZM are plotted with solid lines.)

7.5. SUMMARY

A CLD1-based high-speed Y-fed directional coupler with 22GHz 3-dB bandwidth demonstrated a performance similar to a quadrature-biased MZM in terms of distortion suppression when no direct-current bias was applied. The linearity properties of the high-speed Y-fed directional coupler were investigated theoretically. The results show that broadband high-linear modulators can be achieved by taking advantage of the small dispersion in EO polymers' refractive indexes at microwave and optic frequencies, and by taking advantage of their high EO coefficient. A broadband high-linear modulator based on a Δβ-inverted Y-fed directional coupler made of CLD1 was demonstrated. This modulator has 20GHz 3-dB bandwidth and a about 20-dB larger nonlinear distortion suppression, in the range between 0 to 8 GHz, than that of a quadrature-biased Mach Zehnder modulator.

References

[1] E. I. Ackerman and C. H. Cox III, “RF fiber-optic link performance”, *IEEE Microwave Magazine*, vol. 2 , no. 4, pp. 50-58, Dec. 2001.

[2] E. I. Ackerman and C. H. Cox III, “State of the art in analog fiber-optic link technology”, in *URSI International Symposium on Signals, Systems, and Electronics (ISSSE 98),* Sept. 29 - Oct. 2, 1998, pp. 372–377.

[3] G. L. Li and P. K. L. Yu, “Optical intensity modulators for digital and analog applications”, *J. Lightwave Technol.*, vol. 21, no. 9, pp. 2010–2030, Sept. 2003.

[4] M. Nazarathy, J. Berger, A. J. Ley, I. M. Levi, and Y. Kagan, “Progress in externally modulated AM CATV transmission systems”, *J. Lightwave Technol.*, vol. 11, no. 1, pp. 82-105, Jan. 1993.

[5] K. Wakita, *Semiconductor Optical Modulators*, Kluwer Academic Publishers, 1998.

[6] L. R. Dalton, “Nonlinear Optical Polymetic Materials: From Chromophore Design to Commercial Applications”, *Advances in Polymer Science*, vol. 158, pp. 1-86, 2002.

[7] W. B. Bridges and J. H. Schaffner, “Distortion in linearized electrooptic modulators*”, IEEE Trans. Microwave Theory Technol.*, vol. 43, no. 9, pp. 218–2197, Sept. 1995.

[8] U. V. Cummings and W. B. Bridges, “Bandwidth of linearized electrooptic modulators”, *J. Lightwave Technol.*, vol. 16, no. 8, pp. 1482-1490, Aug. 1998.

[9] E. I. Ackerman, “Broad-band linearization of a Mach-Zehnder electrooptic modulator”, *IEEE Trans. Microwave Theory Technol.*, vol. 47, no. 12, pp. 2271-2279, Dec. 1999.

[10] J. H. Schaffner, et al. “Spur-free dynamic range measurements of a fiber optic link with traveling wave linearized directional coupler modulators”, *IEEE Photon. Technol. Lett.*, vol. 6, no. 2, pp. 273-275, Feb. 1994.

[11] R. F. Tavlykaev, and R. V. Ramaswamy, “Highly linear Y-fed directional coupler modulator with low intermodulation distortion”, *J. Lightwave Technol.*, vol. 17, no. 2, pp. 282-291, Feb. 1999.

[12] T. Kishino, R. F. Tavlykaev, and R. V. Ramaswamy, “A Y-fed directional coupler modulator with a highly linear transfer curve”, *IEEE Photon. Technol. Lett.*, vol. 12, no. 11, pp. 1474-1476, Nov. 2000.

[13] L. R. Dalton, A. W. Harper, R. Ghosn, W. H. Steier, M. Ziari, H. R. Fetterman, Y. Shi, R. V. Mustacich, A. K. Y. Jen, and K. J. Shea, “Synthesis and Processing of Improved Organic Second-Order Nonlinear Optical Materials for Applications in Photonics”, *Chem. Mater.*, vol. 7, pp. 1060-1081, 1995.

[14] F. Kajzar, K. S. Lee, and A. K. Y. Jen, “Polymeric Materials and their Orientation Techniques for Second-Order Nonlinear Optics”, *Advances in Polymer Science*, vol. 161, pp. 1-85, Springer-Verlag Berlin Heidelberg 2003.

[15] J. Zyss and I. Ledoux, “Nonlinear Optics in Multipolar Media: Theory and Experiments”, *Chem. Rev.*, vol. 94, no. 1, pp. 77-105, 1994.

[16] C. Andraud, T. Zabulon, A. Collet, and J. Zyss, “Nonlinear optical properties of polyenoctupoles: a multipolar tensorial quantum analysis”, *Chemical Physics*, vol. 245, pp. 243–261, 1999.

[17] L. R. Dalton, “Polymers for electro-optic modulator waveguides”, in: Wise DL, Wnek G, Trantolo DJ, Cooper TM, Gresser JD (eds) *Electrical and optical polymer systems*, Marcel Dekker, New York, 1998, ch. 18.

[18] Sekkat Z, Dumont M (1992) *Nonlinear Opt.,* 2:359.

[19] Dumont M, Sekkat Z, Loucif-Saibi R, Nakatani K, Delaire J (1993) *Nonlinear Opt.,* 5:229.

[20] Dumont M, Froc G, Hosotte S (1995) *Nonlinear Opt.,* 9:327.

[21] Charra F, Kajzar F, Nunzi JM, Raimond P, Idiart E (1993) *Opt. Lett.*, 18:941.

[22] F. Kajzar, F. Charra, J. M. Nunzi, P. Raimond, E. Idiart, M. Zagorska, “Third-order nonlinear optical properties of functionalized polymers”, in: Prasad PN (ed) *Proceedings of international conference on frontier of polymers and advanced materials*, Plenum Press, New York, 1995, pp. 141.

[23] Comizzoli B (1987) *J Electrochem Soc Solid Sci Technol* 134:424.

[24] K. D. Singer, M. G. Kuzyk, W. R. Holland, J. E. Sohn, S. J. Lalama, B. Comizzoli, H. E. Katz, and M. L. Schilling, "Electro-optic phase modulation and optical second-harmonic generation in corona-poled polymer films", *Appl Phys Lett*, vol. 53, no. 19, pp. 1800-1802, Nov. 1998.

[25] M. Date, T. Furukawa, T. Yamaguchi, A. Kojima, and I. Shibata, "Opto-ferroelectric memories using vinylidene fluoride and trifluoroethylene", *IEEE Trans. Dielect. El. In.*, vol. 24, no. 3, pp. 537-540, 1989.

[26] S. Yilmaz, S. Bauer, and R. Gerhard-Multhaupt, "Photothermal poling of nonlinear optical polymer films", *Appi. Phys. Lett.*, vol. 64, no. 21, pp. 2770-2772, 1994.

[27] B. Gross, R. Gerhard-Multhaupt, A. Berraisoul, G. M. Sessler, "Electron-beam poling of piezoelectric polymer electrets", *J. Appl. Phys.*, vol. 62, no. 4, pp. 1429-1432, Aug. 1987.

[28] S. Bauer, *Appl. Phys. Rev.*, 80:5531, 1996.

[29] D. Healy, P. R. Thomas, M. Szablewski, and G. H. Gross, *Proc SPIE*, 2527:32, 1995.

[30] Meyrueix R, Tapolsky G, Chan YP, Lecomte JP (1995) Mol Cryst Liq Cryst S&T B Nonlin. Opt 9:293.

[31] K. D. Singer, J. E. Sohn, and S. J. Lalama, "Second harmonic generation in poled polymer films", *Appl. Phys. Lett.*, vol. 49, no. 5, pp. 248-250, 1986.

[32] G. Gadret, F. Kajzar, and P. Raimond, "Nonlinear optical properties of poled polymers", In: Singer KD (ed) *Nonlinear optical properties of organic materials IV. Proc SPIE* 1560:226, 1991.

[33] M.-C. Oh, H. Zhang, C. Zhang, H. Erlig, Y. Chang, B. Tsap, D. Chang, A. Szep, W. H. Steier, H. R. Fetterman, and L. R. Dalton, "Recent Advances in Electrooptic Polymer Modulators Incorporating Highly Nonlinear Chromophore", *IEEE J. On Sellected Topics In Quantum Electronics*, vol. 7, no. 5, pp. 826-835, 2001.

[34] I. Liakatas, C. Cai, M. Bösch, M. Jäger, Ch. Bosshard, P. Günter, C. Zhang, and L. R. Dalton, "Importance of intermolecular interactions in the nonlinear optical properties of poled polymers," *Appl. Phys. Lett.*, vol. 76, no. 11, pp. 1368–1370, 2000.

[35] S. Ermer, D. G. Girton, L. S. Dries, R. E. Taylor, W. Eades, T. E. van Eck, A. S. Moss, and W. W. Anderson, "Low-voltage electro-optic modulation

using amorphous polycarbonate host material," *Proc. SPIE*, vol. 3949, pp. 148–155, 2000.

[36] S. N. Tang, Z. Shi, D. C. An, et al, "Highly efficient linear waveguide modulator based on domain-inverted electro-optic polymers," *Opti. Eng,.* vol. 39, no. 3, pp. 680-688, 2000.

[37] S. Sonoda, I. Tsuruma I, and M. Hatori, "Second harmonic generation in a domain-inverted MgO-doped LiNbO3 waveguide by using a polarization axis inclined substrate", *Appl. Phys. Lett.*, vol. 71, no. 21, pp. 3048-3050, 1997.

[38] W. D. Wang, R. Tavlykaev, and R. V. Ramaswamy, "Bandpass traveling-wave Mach-Zehnder modulator in LiNbO3 with domain reversal", *IEEE Photonics Technology Letters,* vol. 9, no. 5, pp. 610-612, 1997.

[39] S. M. Garner, S.-S. Lee, V. Chuyanov, A. Chen, A. Yacoubian, W. H. Steier, and L. R. Dalton, "Three-dimensional integrated optics using polymers", *IEEE J. Quant. Electron.*, vol. 35, no. 8, pp. 1146-1155, Aug. 1999.

[40] R. A. Soref, J. Schmidtchen, and K. Petermann, "Large single-mode rib waveguides in GeSi-Si and Si-on-SiO_2," *IEEE J. Quantum Electron.*, vol. 27, no. 8, pp. 1971-1974, 1991.

[41] S. P. Pogossian, L. Vescan, and A. Vonsovici, "The single-mode condition for semiconductor rib waveguides with large cross section," *J. Lightwave Technol.*, vol. 16, no. 10, pp. 1851-1853, 1998.

[42] U. Fisher, T. Zinke, J. R. Kropp, F. Arndt, and K. Petterman, "0.1 dB/cm waveguide losses in single-mode SOI rib waveguides," *IEEE Photon. Technol. Lett.*, vol. 8, no. 5, pp. 647-648, 1996.

[43] R. C. Alferness, *Integrated Photonics Research*, **7**, paper L2-1, Dana Point, CA (1995).

[44] Paul R. Ashley, *Proc. SPIE*, **2290**, 114 (1994).

[45] R. C. Alferness, "Waveguide Electrooptic Modulators", *IEEE Trans. Microwave Theory Tech.*, vol. 82, no. 8, pp. 1121-1137, 1982.

[46] K. Noguchi, O. Mitomi, K. Kawano, and M. Yanagibashi, "Highly efficient 40-GHz bandwidth Ti:LiNbO3 optical modulator employing ridge structure", *IEEE Photon. Technol. Lett.*, vol. 5, no. 1, pp. 52-54, Jan. 1993.

[47] D. G. Girton, S. L. Kwiatkowski, G. .F. Lipscomb, and R. S. Lytel, “20 GHz electro-optic polymer Mach–Zehnder modulator”, *Appl. Phys. Lett,* vol. 58, no. 16, pp. 1730-1732, 1991.

[48] D. Chen, D. Bhattacharya, A. Udupa, B. Tsap, H. R. Fetterman, A. Chen, S.-S. Lee, J. Chen, W. H. Steier, and L. R. Dalton, “High-frequency polymer modulators with integrated finline transitions and low Vπ”, *IEEE Photon. Technol. Lett.*, vol. 11, no. 1, pp. 54-56, Jan. 1999.

[49] Y. Shi, W. Wang, J. H. Bechtel, A. Chen, S. Garner, S. Kalluri, W. H. Steier, D. Chen, H. R. Fetterman, L. R. Dalton, and L. Yu, “Fabrication and characterization of high-speed polyurethane-disperse red 19 integrated electrooptic modulators for analog system applications”, *IEEE J. Sel. Top. Quant. Electron.*, vol. 2, no. 2, pp. 289-299, June 1996.

[50] T. A. Tumolillo and P. R. Ashley, “Multilevel registered polymeric Mach–Zehnder intensity modulator array”, *Appl. Phys. Lett*, vol. 62, no. 24, pp. 3068-3070, June 1993.

[51] Y. Shi, W. Wang, W. Lin, D. J. Olson, and J. H. Bechtel, “Long-term stable direct current bias operation in electro-optic polymer modulators with an electrically compatible multilayer structure”, *Appl. Phys. Lett*, vol. 71, no. 16, pp. 2236-2238, Oct. 1997.

[52] Heuk Park, Wol-yon Hwang, and J.-J. Kim, *Proc. SPIE*, **2852**, 286 (1996).

[53] S. Thaniyavarn, “Modified 1×2 directional coupler waveguide modulator,” *Electron. Lett.*, vol. 22, no. 18, pp. 941-942, Aug. 1986.

[54] H. Kogelnik and R. V. Schmidt, "Switches directional couplers with alternating Δß", *IEEE J. of Quantum Electron.*, vol. 12, pp. 396-401, July 1976.

[55] A. Yariv, "Coupled mode theory for guided wave optics", *IEEE J. Quantum Electron.,* vol. 9, no. 9, pp. 919-933, Sep. 1973.

[56] E. A. J. Marcatili, "Dielectric rectangular waveguide and directional coupler for integrated optics," *Bell System Technical Journal*, vol. 53, no. 4, pp. 2071-2102, 1974.

[57] F. Wang, A. Ren, M. He, M. Lee, A. W. Harper, L. R. Dalton, H. Zhang, S. M. Garner, A. T. Chen, and W. H. Steier, *Polymer Preprints*, **39**(2), 1065 (1998).

[58] W. K. Burns and A. F. Milton, “Mode conversion in Planar-dielectric separating waveguides”, *IEEE J. Quantum Electron.*, vol. 11, no. 1, pp. 32-39, 1975.

[59] D. An, Z. Shi, L. Sun, J. M. Taboada, Q. Zhou, X. Lu, R. T. Chen, S. Tabg, H. Zhang, W. H. Steier, A. Ren, and L. R. Dalton, “Polymeric electro-optic modulator based on 1Ã2 Y-fed directional coupler”, *Appl. Phys. Lett.*, vol. 76, no. 15, pp. 1972-1974, 2000.

[60] H. Chung, W.S.C. Chang, “Normal-mode small-signal analysis of traveling-wave directional couplers,” *IEEE J. Quantum Electron.*, vol. 28, no. 5, pp. 1353-1359, May 1992.

[61] H. Bulmer, “Sensitive, highly linear lithium niobate interferometers for electromagnetic field sensing,” *Appl. Phys. Lett.*, vol. 53, pp. 2368-2370, 1988.

[62] H. Zmuda and E. N. Toughlian, *Photonic Aspects of Modern Radar.* Boston, MA: Artech House, 1994.

[63] Y. Chen and R. T. Chen, “A fully packaged true time delay module for a K-band phased-array antenna system demonstration,” *IEEE Photon. Technol. Lett.*, vol. 14, no. 8, pp. 1175- 1177, 2002.

[64] G. Girton, S. L. Kwiatkowski, G. F. Lipscomb, and R. S. Lytel, “20 GHz electro-optic polymer Mach-Zehnder modulator,” *Appl. Phys. Lett.*, vol. 58, no. 16, pp.1730-1732, April, 1991.

[65] D. An, Z. Shi, L. Sun, J. M. Taboada, Q. Zhou, X. Lu, R. T. Chen, S. Tabg, H. Zhang, W. H. Steier, A. Ren, and L. R. Dalton, “Polymeric electro-optic modulator based on 1×2 Y-fed directional coupler,” *Appl. Phys. Lett.*, vol. 76, no. 15, pp. 1972-1974, April 2000.

[66] J. J. Veselka, D. A. Herr, T. O. Murphy, L. L. Buhl, and S. K. Korotky, “Crosstalk measurements of integrated high-speed Ti:LiNbO$_3$ $\Delta\beta$-reversal switching circuits,” *J. Lightwave Technol.*, vol. 7, no. 6, pp. 908-910, June 1989.

[67] K. Noguchi, H. Miyazawa, and O. Mitomi, “40-Gbit/s Ti: LiNbO$_3$ optical modulator with a two-stage electrode,” *IEICE Trans. Electron.*, vol. E81-C, pp. 1316-1320, Aug. 1998.

[68] K. Kawano, K. Noguchi, T. Kitoh, and H. Miyazawa, “A finite element method (FEM) analysis of a shielded velocity-matched Ti: LiNbO$_3$ optical modulator,” *IEEE Photon. Technol. Lett.*, vol. 3, pp. 919-921, Oct. 1991.

[69] O. Mitomi, K. Noguchi, and H. Miyazawa, “Design of ultra-broad-band $LiNbO_3$ optical modulator with ridge structure,” *IEEE Trans. Microwave Theory Tech.*, vol. 43, pp. 2203-2207, Sept. 1995.

[70] M. Koshiba, Y. Tsuji, and M. Nishio, “Finite-element modeling of broad-band traveling-wave optical modulators,” *IEEE Trans. Microwave Theory Tech.*, vol. 47, pp. 1627-1633, Sept. 1999.

[71] M. Goano, F. Bertazzi, P. Caravelli, G. Ghione, and T. A. Driscoll, “A general conformal-mapping approach to the optimum electrode design of coplanar waveguides with arbitrary cross-section,” *IEEE Trans. Microwave Theory Tech.*, vol. 49, no. 9, pp. 1573-1580, Sept. 2001.

[72] T. A. Driscoll, “Algorithm 756: A MATLAB toolbox for Schwarz-Christoffel mapping,” *ACM Trans. Math. Softw.*, vol. 22, no. 2, pp. 168-186, June 1996.

[73] T. A. Driscoll, *Schwarz-Christoffel Toolbox User’s Guide: Version 2.3*. Newark, DE: Department of Mathematical Sciences, University of Delaware, 2002.

[74] H. A. Wheeler, “Formulas for the skin effect,” *Proc. IRE*, vol. 30, pp. 412-424, Sept. 1942.

[75] *Ansoft HFSS manual*. Ansoft Corporate, Four Station Square Suite 200, Pittsburgh, PA 15219-1119, USA.

Vita

Qingjun Zhou was born in Wangqing, Jilin Province, P. R. China, on Dec. 19, 1968, the son of Yuxian Zhou and his wife Guizhi Ma. After completing his study at the Wangqing Fourth Middle School, also in Wangqing, he entered Jilin University in Changchun, where he received the degree of Bachelor of Science in Physics, with honors, in July 1991.

He attended the graduate school of the Chinese Academy of Sciences (CAS), Beijing, China, in Sept. 1991. In March 1994 he obtained the degree of Master of Science in Physics, with honors, from the Center for Space Science and Applied Research (CSSAR), a division of CAS. Thereafter, he was employed by the CSSAR as a research scientist.

He entered the Electrical and Computer Engineering (ECE) Department of The University of Texas at Austin, Austin, TX, in June 1999. He received the degree of Master of Science in ECE from The University of Texas at Austin in December 2001.

Permanent Address: Jincang, Fuxing Town
Wangqing County, Jilin Province 133219
P.R. China

This dissertation was typed by the author.